NAVAL POSTGRADUATE SCHOOL
Monterey, California

THESIS

TARGET DETECTION AND CLASSIFICATION AT KERNEL BLITZ 1997 USING SPECTRAL IMAGERY

By

Jeffrey D. Sanders

December 1998

Thesis Advisors: Richard C. Olsen
                     David D. Cleary

Approved for public release; distribution is unlimited

19990726 049

REPORT DOCUMENTATION PAGE

Public reporting burden for this collection of information is estimated to average 1 hour per response, including the time for reviewing instruction, searching existing data sources, gathering and maintaining the data needed, and completing and reviewing the collection of information. Send comments regarding this burden estimate or any other aspect of this collection of information, including suggestions for reducing this burden, to Washington headquarters Services, Directorate for Information Operations and Reports, 1215 Jefferson Davis Highway, Suite 1204, Arlington, VA 22202-4302, and to the Office of Management and Budget, Paperwork Reduction Project (0704-0188) Washington DC 20503.

1. AGENCY USE ONLY *(Leave blank)*	2. REPORT DATE December 1998	3. REPORT TYPE AND DATES COVERED Master's Thesis

4. TITLE AND SUBTITLE
TARGET DETECTION AND CLASSIFICATION AT KERNEL BLITZ 1997 USING SPECTRAL IMAGERY

5. FUNDING NUMBERS

6. AUTHOR(S)
Sanders, Jeffrey D.

7. PERFORMING ORGANIZATION NAME(S) AND ADDRESS(ES)
Naval Postgraduate School
Monterey, CA 93943-5000

8. PERFORMING ORGANIZATION REPORT NUMBER

9. SPONSORING / MONITORING AGENCY NAME(S) AND ADDRESS(ES)

10. SPONSORING/MONITORING AGENCY REPORT NUMBER

11. SUPPLEMENTARY NOTES
The views expressed in this thesis are those of the author and do not reflect the official policy or position of the Department of Defense or the U.S. Government.

12a. DISTRIBUTION / AVAILABILITY STATEMENT
Approved for public release; distribution is unlimited.

12b. DISTRIBUTION CODE

13. ABSTRACT *(maximum 200 words)*

Data collected from the Hyperspectral Digital Imagery Collection Experiment (HYDICE) were analyzed in this thesis to determine the feasibility of wide area detection and classification of target materials in the visible to short wave infrared region. This study used detection algorithms such as spectral angle mapper and matched filter for target detection. Parallelepiped and Maximum Likelihood routines were used to classify the image data for subsequent analyses and comparisons. Effects on data due to altitude variation of the sensor were analyzed using histograms, differencing, and principal component transforms. Data images of the Camp Pendleton airfield used for comparison analyses were obtained from two different altitudes, 5,000 feet and 10,000 feet. Results showed target detection and classification had no strong dependence on altitude.

14. SUBJECT TERMS
Remote sensing, Hyperspectral, Imagery, Target Detection, Classification, HYDICE, Littoral Radiance II, Kernel Blitz '97, Camp Pendleton

15. NUMBER OF PAGES
115

16. PRICE CODE

17. SECURITY CLASSIFICATION OF REPORT Unclassified	18. SECURITY CLASSIFICATION OF THIS PAGE Unclassified	19. SECURITY CLASSIFICATION OF ABSTRACT Unclassified	20. LIMITATION OF ABSTRACT UL

NSN 7540-01-280-5500

Standard Form 298 (Rev. 2-89)
Prescribed by ANSI Std. 239-18

TARGET DETECTION AND CLASSIFICATION AT KERNEL BLITZ 1997 USING SPECTRAL IMAGERY

Jeffrey D. Sanders
Lieutenant, United States Navy
B.S., University of Nevada Reno, 1990

Submitted in partial fulfillment of the
requirements for the degree of

MASTER OF SCIENCE IN APPLIED PHYSICS

from the

NAVAL POSTGRADUATE SCHOOL
December 1998

Author: _____
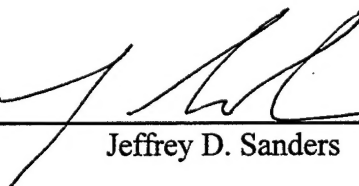
Jeffrey D. Sanders

Approved by: _____
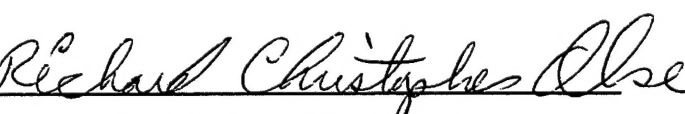
Richard C. Olsen, Thesis Advisor

_____
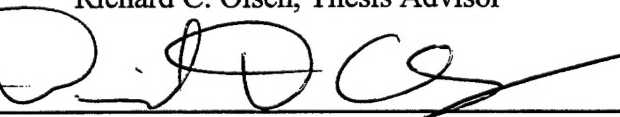
David D. Cleary, Thesis Advisor

_____
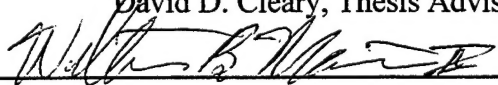
Bill Maier, Chairman
Department of Physics

iii

ABSTRACT

Data collected from the Hyperspectral Digital Imagery Collection Experiment (HYDICE) were analyzed in this thesis to determine the feasibility of wide area detection and classification of target materials in the visible to short wave infrared region. This study used detection algorithms such as spectral angle mapper and matched filter for target detection. Parallelepiped and Maximum Likelihood routines were used to classify the image data for subsequent analyses and comparisons. Effects on data due to altitude variation of the sensor were analyzed using histograms, differencing, and principal component transforms. Data images of the Camp Pendleton airfield used for comparison analyses were obtained from two different altitudes, 5,000 feet and 10,000 feet. Results showed target detection and classification had no strong dependence on altitude.

TABLE OF CONTENTS

ACKNOWLEDGEMENTS

I.   INTRODUCTION

The great importance of remote sensing has been realized in the past couple of decades. An image space is available for remote sensing techniques that include time, space, and wavelength dimensions. From ground systems to satellite systems, the third axis (wavelength dimension) has become a prominent area of research for many scientific, commercial, and military applications. Hyperspectral imaging is a type of remote sensing that refers to imaging a scene in many narrow spectral bands. The goal of hyperspectral imaging is to provide the third axis of the "image space" with powerful information that can be used in classification or characterization of the environment. The advantage gained from this full spectrum signature is the ability to distinguish between similar objects being imaged. In different materials there are distinct differences in spectral signature in one or many wavelength bands of the sensor. These distinctions are seen as absorption features characteristic to a given material or small group of materials.

A.   APPLICATIONS

Reflectance spectrum absorption features have been used extensively by the geological society to identify important rock formations, geologic mapping and studies of volcanoes. Commercial applications involve health analysis of crops to determine specific watering and fertilizing requirements. And finally, spectral analysis techniques have been demonstrated in many military applications, including but not limited to, finding targets, classifying material types, and mapping possible transport routes.

Hyperspectral sensors that are currently being demonstrated or evaluated for operational use include the Airborne Visible/Infrared Imaging Spectrometer (AVIRIS), the Spatially Enhanced Broadband Array Spectrograph System (SEBASS), and the Hyperspectral Digital Imagery Collection Experiment (HYDICE) systems. These systems are carried on airplanes and image scenes anywhere from 2,000 feet to 25,000 feet.

Recent systems include advancements in signal-to-noise ratio, spectral calibration accuracy, resolution, and number of spectral channels.

B.   THESIS OBJECTIVES

This work is conducted in support of the Hyperspectral MASINT Support to Military Operations (HYMSMO) program. In support of the HYMSMO program the Littoral Radiance II Exercise was conducted in June of 1997. This exercise included littoral, beach, and inland image experiments. The images of the airfield at Camp Pendleton proved to be an ideal data set to examine the feasibility of wide area target detection and affects on HYDICE data due to altitude variation. Camp Pendleton is located just north of Oceanside California and has an airfield approximately two miles inland where several HYMSMO targets were deployed in unknown locations.

This study further evaluates the utility of hyperspectral imaging for wide area applications. To meet this objective, data were analyzed to determine the feasibility of finding targets deployed in various locations in and around the Camp Pendleton airfield facilities. Then following these "blind test" results, the data were further processed and analyzed to evaluate the differences between the results obtained from varying altitudes.

Several reasons for researching these affects exist. Among these is the future use of hyperspectral sensors in space. Hyperspectral imaging is fairly young and has not yet been employed from space. The Lewis spacecraft was launched in August of 1997 with a 384-channel sensor, but did not succeed in demonstrating hyperspectral technology from space. Soon after launch the spacecraft developed a slow spin rendering the solar array unusable. The spacecraft could not be recovered, and it re-entered the Earth's atmosphere in September of 1997.

Two current projects exploring the feasibility of hyperspectral sensors in space are the NEMO program and the Warfighter program. The NEMO program is sponsored by the Navy and Industry. The NEMO sensor is a high-resolution sensor for use in several military and commercial applications. The Airforce sponsors the Warfighter-1 program.

The Warfighter-1 satellite will carry a high performance electro-optical digital camera with hyperspectral imaging capabilities. Both of these programs will provide validation of hyperspectral technologies and develop ground-based image processing techniques for further use in military applications.

C.   THESIS OUTLINE

All data presented in this thesis were obtained with the HYDICE sensor. A description of the HYDICE sensor is presented in Chapter 2. Chapter 3 is a discussion of the Littoral Radiance II experiment with specifics for the Camp Pendleton airfield scenes. Chapter 4 outlines the "blind test" study with target results and observations in Chapter 5. Chapter 6 describes the methodology and results on comparing the images flown at different altitudes. And finally, Chapter 7 presents the conclusions drawn from the analysis of the Littoral Radiance II collect.

II.   THE HYDICE SENSOR

A.   GENERAL DESCRIPTION:

The Hyperspectral Digital Imagery Collection Experiment (HYDICE) was designed to obtain 'clean' image data in the range of .4 μm to 2.5 μm. The HYDICE sensor was built by Hughes-Danbury Optical Systems, Inc. and is flown in a CV 580 aircraft. This sensor has been operational since 1995. A cutaway of the HYDICE instrument is shown in Figure 2.1 with the major parameters highlighted in Table 2.1. A photograph of the CV-580 aircraft outfitted with the HYDICE sensor is located in the Appendix.
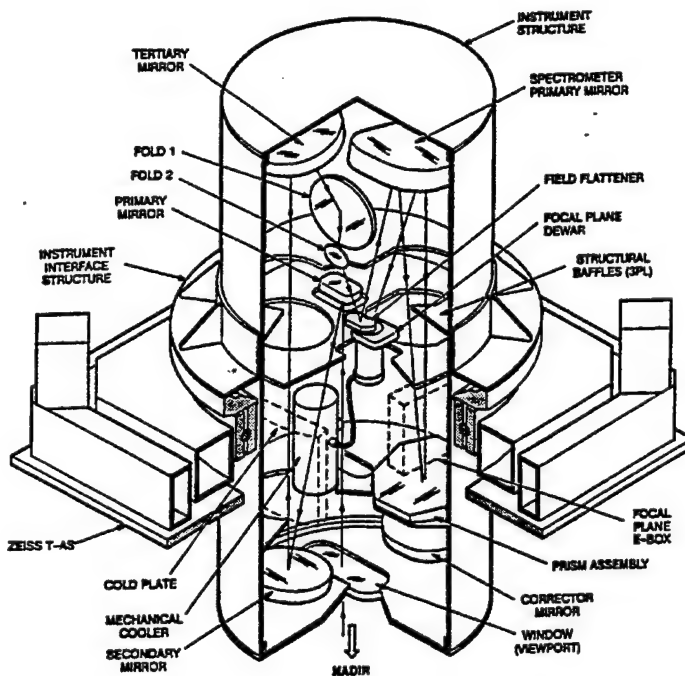
Figure 2.1: Opto-Mechanical Subsystem and stabilization platform for HYDICE. From "The HYDICE INSTRUMENT DESIGN", Basedow 1992.

Table 2.1: HYDICE Operational Parameters extracted from Basedow 1992, Basedow 1994, and Silvergate 1996.

Parameter	Value
Spectral Range	400 to 2,500 nm
Number of Spectral Channels	210
Channel Width (FWHM)	3-15 nm
Optics	Paul Baker telescope Schmidt prism spectrometer
Aperture diameter	27 mm
Swath FOV	9°
Swath width	208 pixels
IFOV	0.51 mrad (average)
Array size	320 X 210 pixels
Integrated modes	Snap Shot & continuous
Integration time	10.5 msec (design point) 1.0 - 42.3 msec (range)
Frame time	17.3 msec (design point) 8.3 - 50 msec (range)
Readout time; Quantization	7.3 msec (fixed); 12 bits
Spectral co-registration (smile)	5% of FWHM (average)
Spatial co-registration	55 μrad at edge of field (average)
Instrument operating temperature	10 °C
MTF (laboratory)	> 0.58 in-track > 0.33 cross-track
InSb focal plane in three regions	A .40 - 1.0 μm B 1.0 - 1.9 μm C 1.9 - 2.5 μm
Average SNR (by gain region)	217/107/40 @ 5% reflectance
Average dynamic range (by gain region)	955/54/17 watts per m²/steradian/micron
Polarization	< 4% above 445 NM < 12% below 445 NM
Aircraft	ERIM CV-580
Aircraft operating altitude	Sea level - 25,000 ft
V/H (aircraft limits)	0.013-0.059 rad/sec(selectable)

This design of this instrument accounted for lessons learned from programs such as Airborne Visible/Infrared Imaging Spectrometer (AVIRIS) and the need for increased spatial resolution and signal to noise ratios. The HYDICE Program Office, Naval

Research Laboratory in Washington, D.C. 20375, controls all experiments and operations of HYDICE.

To obtain detailed information throughout the reflectance spectrum, 210 bands with bandwidths of 3 - 15 nm were integrated using a double pass prism spectrometer and solid state sensing techniques. Superior spatial resolution is obtained using a pushbroom scan, a mechanically cooled focal plane, and a wide field telescope. The .51 mrad instantaneous field of view (IFOV), variable frame rates/integration times, and the operating envelope of the Convair 580 aircraft result in ground sample distances of .75 to 4 meters (Basedow, 1992).

B. OPTICS AND DETECTOR:

The detectors are made of Indium Antimonide (InSb) and are housed in a dewar that is kept cooled to 65 K by a 1-Watt linear cooler to maintain a base or reference energy level on the device. Besides preventing unwanted thermal noise, the temperature control also prevents unwanted variations in the properties of the optical components. When radiation enters the view port it first travels through a series of optics before encountering the detector elements. The viewing window is a slit with the long axis perpendicular to the flight path. The last step in the optical process employs a prism assembly (spectrometer) to separate the 210 wavelength bands and focus them on their respective solid state elements. The Photons interact with the InSb elements and force valence electrons to the conduction band. This provides us with an analog signal proportional to the number of photons for each of the 320 spatial pixels at 210 different wavelengths. Each analog signal is then converted to a 12-bit integer digital signal (DN's) for recording. By methods discussed in a later section these 320 X 210 DN's are processed simultaneously and provide us with a minor frame of digital uncalibrated radiance data. A minor frame is 1 pixel along track and 320 pixels across track. The forward motion of the CV 580 aircraft moves the slit in a pushbroom fashion, which results in line by line generation of a major frame. A major frame of data consists of 320

samples by 320 lines. This major frame combined with the 210 spectral bands makes up the data cube. Each major frame is then numbered and several pieces of data are recorded to mark time of frame, lat./long. of aircraft for that frame, aircraft height, etc. A visual example of a major frame is shown in Figure 2.2.
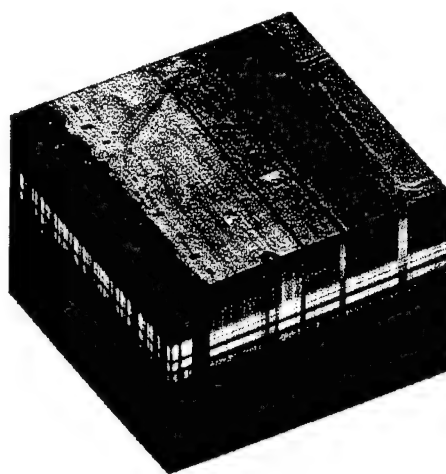
Figure 2.2: HYDICE data cube. This figure represents 320 X 320 spatial pixels by 210 wavelength bands. From "Signal Processing Perspective of Hyperspectral Imagery Analysis Techniques", (Stefanou 1997).

C.   SOLID STATE THEORY:

The InSb detector of the HYDICE instrument consists of a 320 X 210-element matrix. The 320 columns make up 308 elements for the spatial footprint across track and 12 elements for offset calibration. The 210 rows make up the wavelength bands for HYDICE. Each element is 40 µm on a side resulting in a total detector size of about 13 X 8.5 mm. The array is electronically shuttered with a fixed read time of 7.3 msec, a frame time adjusted from 8.3 to 50 msec, and an integration time adjusted from 1.0 to 42.3 msec. With altitudes ranging from 5,000 to 25,000 feet and with proper integration times and frame times selected, the spatial resolutions of 0.75 to 4 meters will result in a maximum swath width of about 1200 meters.

In order to obtain the wavelength coverage (i.e. .4 to 2.5 μm) the solid state device needed to have a band gap of less than .5 eV and must efficiently convert the photons to electrons in this range. A photon of wavelength .4 μm has energy equal to 3.1 eV and a photon of wavelength 2.5 μm has an energy of about .5 eV. The InSb is a III-V compound with a band gap of approximately .23 eV (equivalent wavelength = 5.4 μm). This band gap seems excessively low, but the conversion ratio of photons to electrons for this material is very close to 1:1, which is very attractive. There is a cold filter made of UV-22 glass mounted in the Dewar to filter or absorb all wavelengths longer than about 2.9 μm. Also mounted in the window of the Dewar is a Rugate filter to reject the radiation between 2.5 and 3.0 μm (Basedow 1994).

D.   ANTIREFLECTIVE COATING:

The photoelectric conversion (quantum efficiency) for InSb is shown in Figure 2.3. The bottom curve in this figure shows the measured values of efficiency for uncoated elements. The top curve shows the predicted efficiencies of elements coated with an anti reflective (A-R) material. As with any medium transmitting electromagnetic (E & M) radiation there will be some loss due to reflection at the interface. The amount of reflected light and which polarization's get transmitted depend on the angle of incidence and the index of refraction (n). The angle of incidence is maintained at 90 degrees by adjusting the detector focal plane at 21.9 degrees off of normal to accommodate the optical path. The index of refraction depends on wavelength. Therefore, varying the thickness of the material for each element based on wavelength being detected by that element optimizes the transmission through the A-R coating. This process has shown photoelectric efficiencies of greater than 1.0 for the smaller wavelengths in experiments. The wedge shaped design of the anti reflective coating can be seen in Figure 2.4 below.
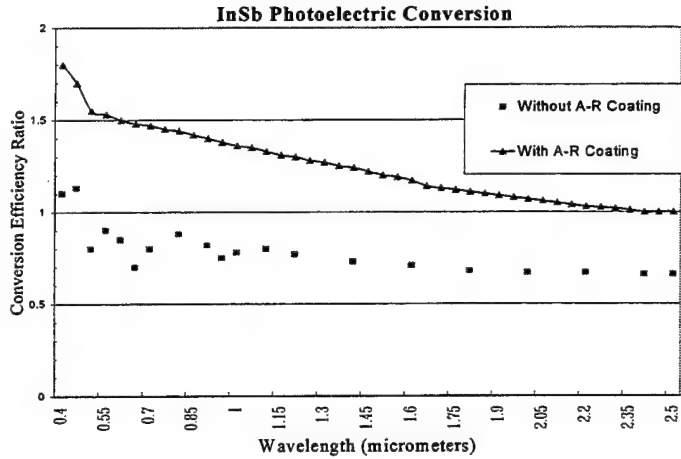
Figure 2.3: Plot of conversion efficiency of InSb verses wavelength (Reproduced figure after Basedow 1992).
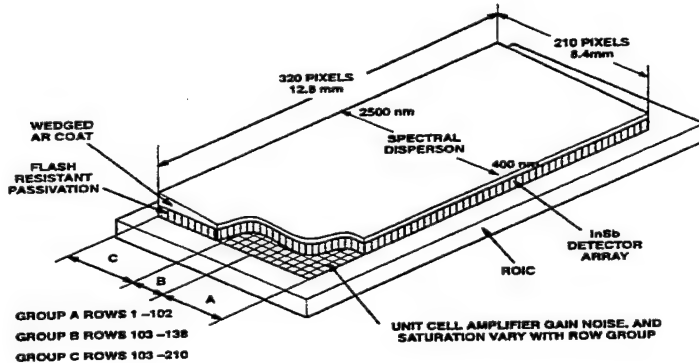
Figure 2.4: Focal plane design. From "HYDICE Focal Plane Design and Performance", (Basedow 1994).

E. ROIC AMPLIFIERS

To ensure simultaneous detection and or readout of all spatial and spectral pixels the element matrix is bump bonded to the Read Out Integration Circuit (ROIC) as seen in the above figure. The ROIC provides amplification and multiplexing necessary for recording to AMPEX tape and for a real time video output. The amplifiers must provide the dynamic range necessary for the lowest radiance input, from the longest wavelengths, and the highest radiance input, at the 1.04 μm range, while still maintaining a high signal

10

to noise ratio. This can't be done using just one amplifier for all wavelengths because of the high noise that would be present in the small wavelength output. The HYDICE design segregates the detector matrix into three different groups based on wavelength allowing for reduced amplifier dynamic ranges and therefore reduced noise in each region.

F.   DATA PROCESSING

After the signal is quantized to 12-bit digital data it is sent to a computer on board the aircraft for a real time display and immediate operator interface. This allows for immediate corrections for an obvious equipment malfunction or incorrect setting. At the same time the data is recorded on an AMPEX DCRSi II 48 Gbyte tape (Basedow 1994).
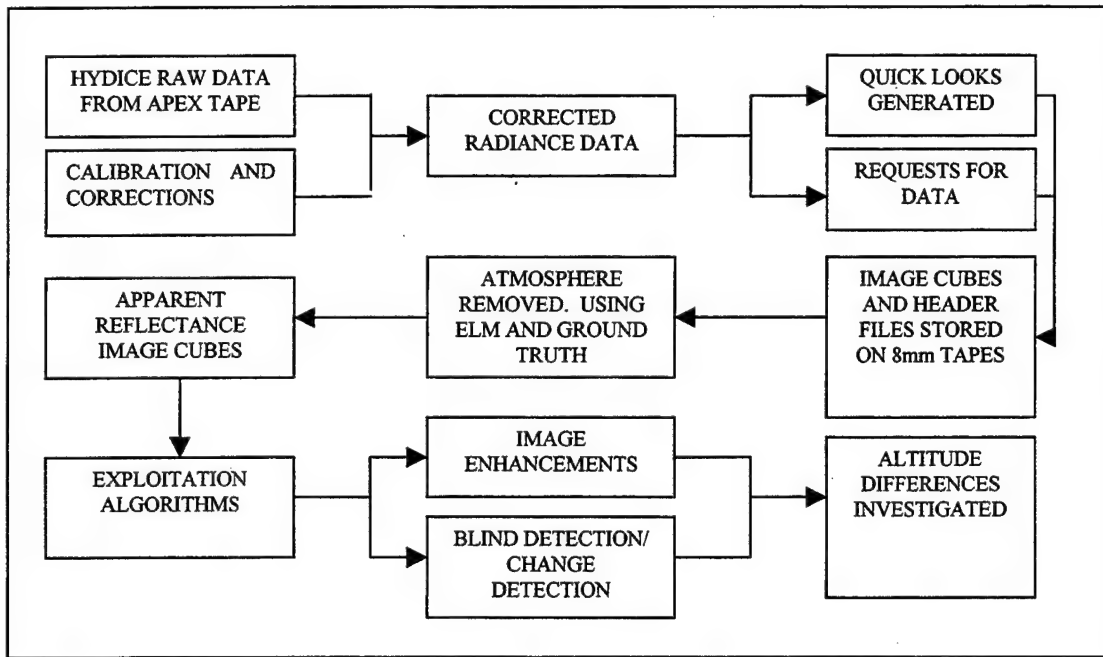
Figure 2.5:   Data path from instrument to exploitation for the Camp Pendleton airfield data.

Each collection experiment consists of several days of flying to collect the required imagery. Each day several hours of data are collected which amounts to tens of Gigabytes of data. Each day these data are sent via the fastest means available to SITAC

11

where the data are then calibrated for corrected radiance and quick looks of the flight lines are produced. These quick looks are then reviewed by any persons or groups planning exploitation to determine which data should be reformatted to an 8 mm 5 Gbyte tape. The calibration techniques are discussed in the next section.

Once the data are disseminated to the appropriate personnel manipulation of this data is still necessary for analysis purposes. Radiance data on the tape are stored as 16 bit integer data. A conversion factor is used to optimize storage. The data are multiplied by a factor of $75W/m^2/sr/\mu m$ to use at least 14 of the 16 bits available. Next, the spectral bands for the particular image are evaluated and full width half maximums are determined. The center wavelengths are then assigned to the cube.

The radiance data can be converted to apparent reflectance, using any of several techniques. The Empirical Line Method was used for the work presented here. Ground truth information is necessary for this method of atmosphere removal and was generated from 6 varying gray calibration panels located at the airfield sight. The data are now ready for exploitation.

G. CALIBRATION

1. Radiometric Calibration

The flight calibration unit (FCU) is a 15-cm polytetraflouroethylene integrating sphere with a 40 X 60-mm aperture, radiance stabilization and monitoring. The (FCU) is mechanically placed in front of a portion of the slit window and employs two redundant halogen lamps referenced to a ground standard that is tied to the U. S. National Institute of Standards and Technology and the U. K. National Physical Laboratory standards. Calibration is performed before or after flight runs by selecting the calibration mode instead of the imaging mode. Due to the size of the FCU compared to the slit window the sensor is tilted to three different positions to illuminate all 320 columns of the FPA. The three frames using the FCU and which columns (samples) are illuminated are shown as Position 1, 2, and 3 in Figure 2.6.
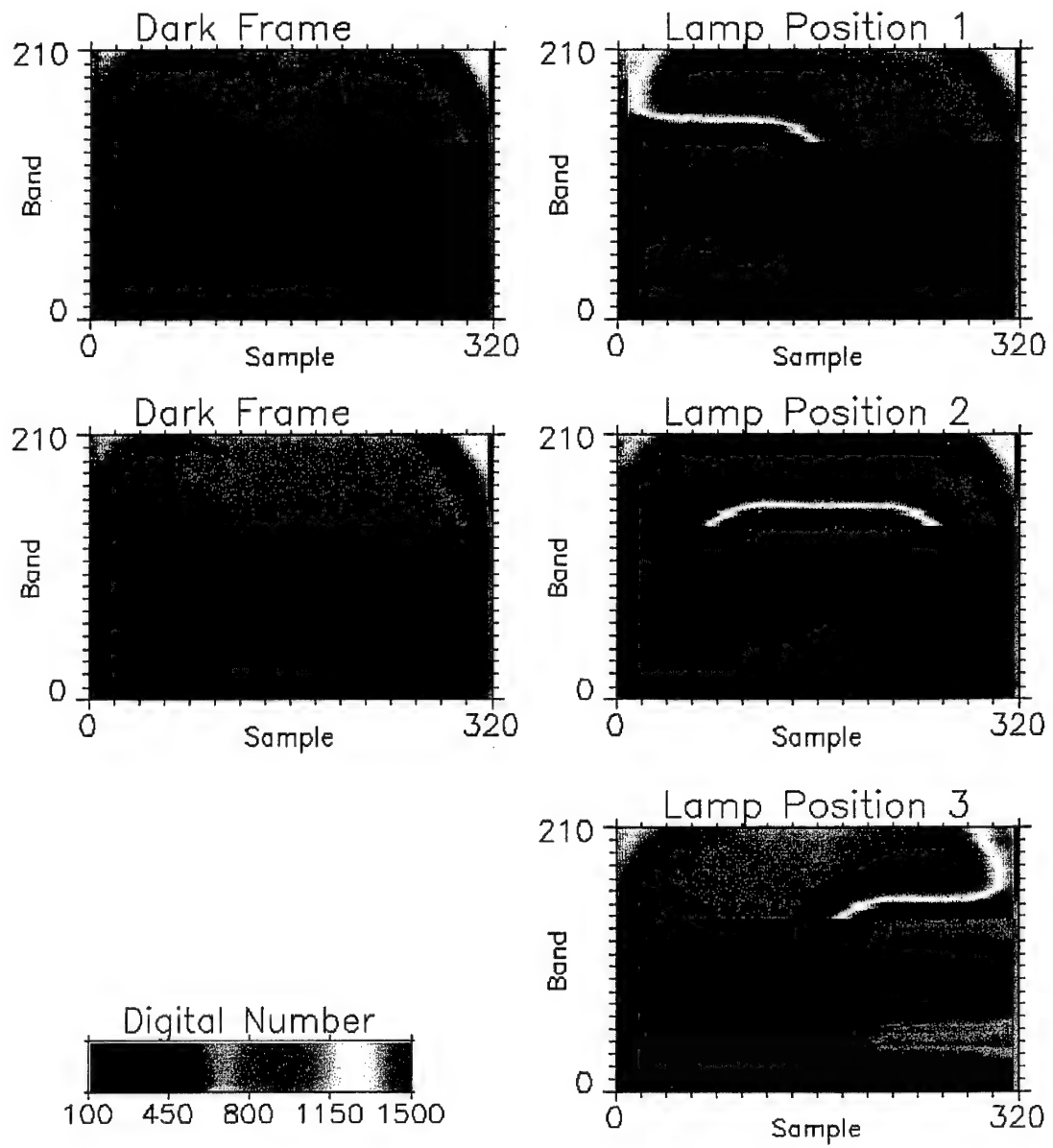
Figure 2.6: HYDICE FCU sequence. Five major frames are acquired, two dark frames with the shutter closed and three frames with the FCU placed in different positions to illuminate all pixels. "Bad" pixels can be seen as red spots against the blue and green background.

2.   Spectral Calibration

A He/Ne laser with a wavelength of 0.6328 μm corresponding to wavelength band 48 is used with the FCU to adjust the spectral channel correlation. The wavelength position of the He/Ne laser is shown in Figure 2.7 and as a small tick mark on the right axis in the Position 1 and 2 illuminations of Figure 2.6. A residual error of 0.2 channels can still exist after calibration using this technique. This calibration deals with quasi-static variations due to varying atmospheric pressure and temperature affecting the dispersion of the prism and associated optics. The temperature is maintained close to constant using the mechanical cooler previously mentioned, but the pressure changes with altitude and environmental operating conditions is not accounted for.

In addition there are higher frequency fluctuations producing fluctuations in the spectral character of the sensor. These are illustrated in the next two figures.
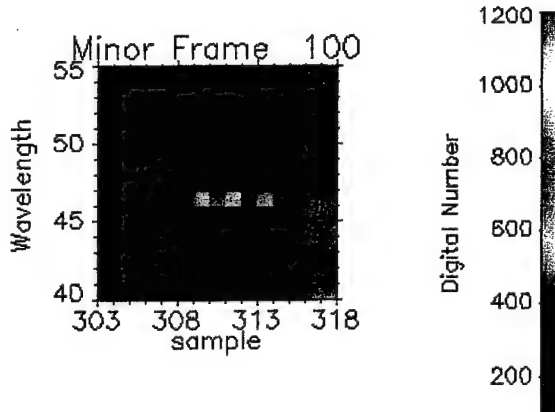
Figure 2.7: Minor Frame 100 from Ivanpah (subset of Figure 2.6 Lamp Position 2). This minor frame shows the wavelength band location   (band 46 and 47) of the He/Ne laser.

3.   Spectral Jitter

The DN for one pixel in Figure 2.7 is plotted as a function of time (top panel, Figure 2.8), and it can be seen that these are low and high frequency fluctuations. The bottom panel is a Fast Fourier Transform (FFT) of that time series and it can be seen that there is a major peak at 17 Hz.
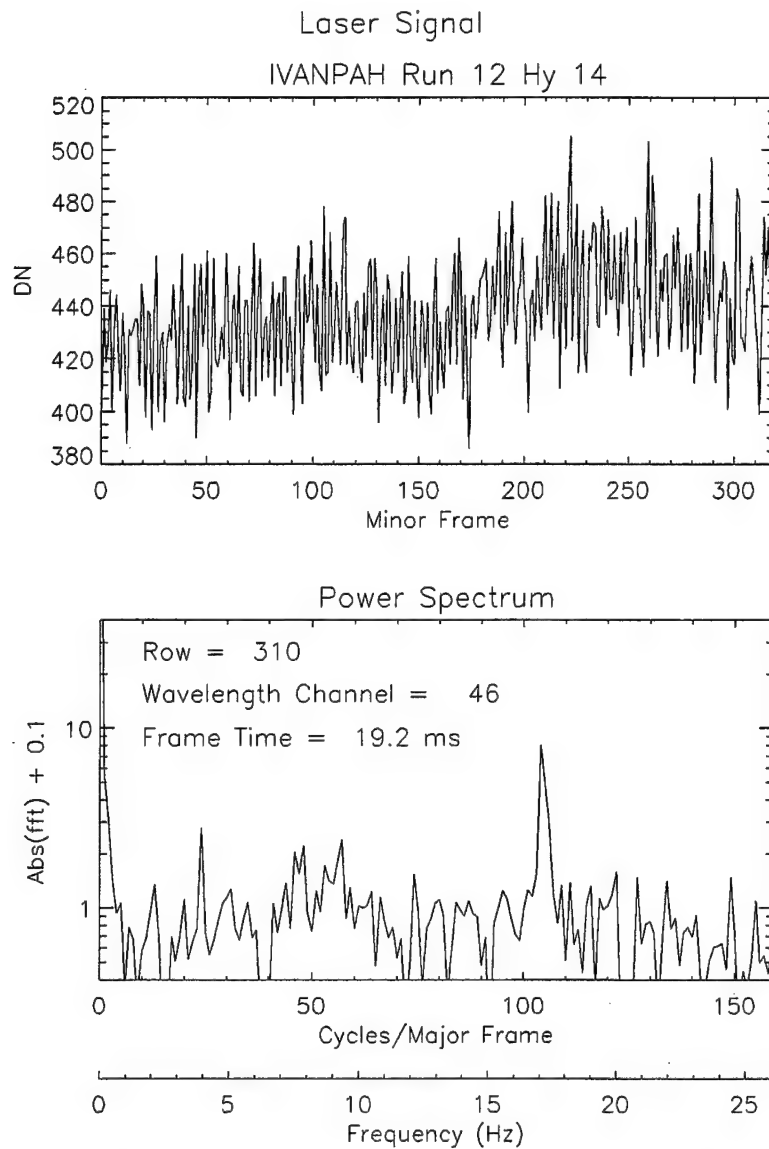
Figure 2.8: **He/Ne laser power detected for one wavelength band over 320 minor frames. Top: Resulting DN values from Ivanpah. Bottom: Fast Fourier Transform Power Spectrum.**

A more global view is found in Figure 2.9. In each panel, the horizontal axis is frequency. In the vertical direction, samples 305 to 316 are plotted for wavelength channels 45-49. (Imagine the bottom panel of Figure 2.8 turned "upwards" for one horizontal stripe.) The peak at 17 Hz is persistent throughout the different runs (generally a small red spot). The power of the laser is initially shared equally between bands 47 and 48 in Run 05. By Run 17 the power has clearly shifted down in the

wavelength bands and is shared by three bands 46, 47, and 48 (nominally 0.612 μm, 0.620 μm and 0.628 μm respectively).

Ivanpah — Laser Spot Power Spectrum
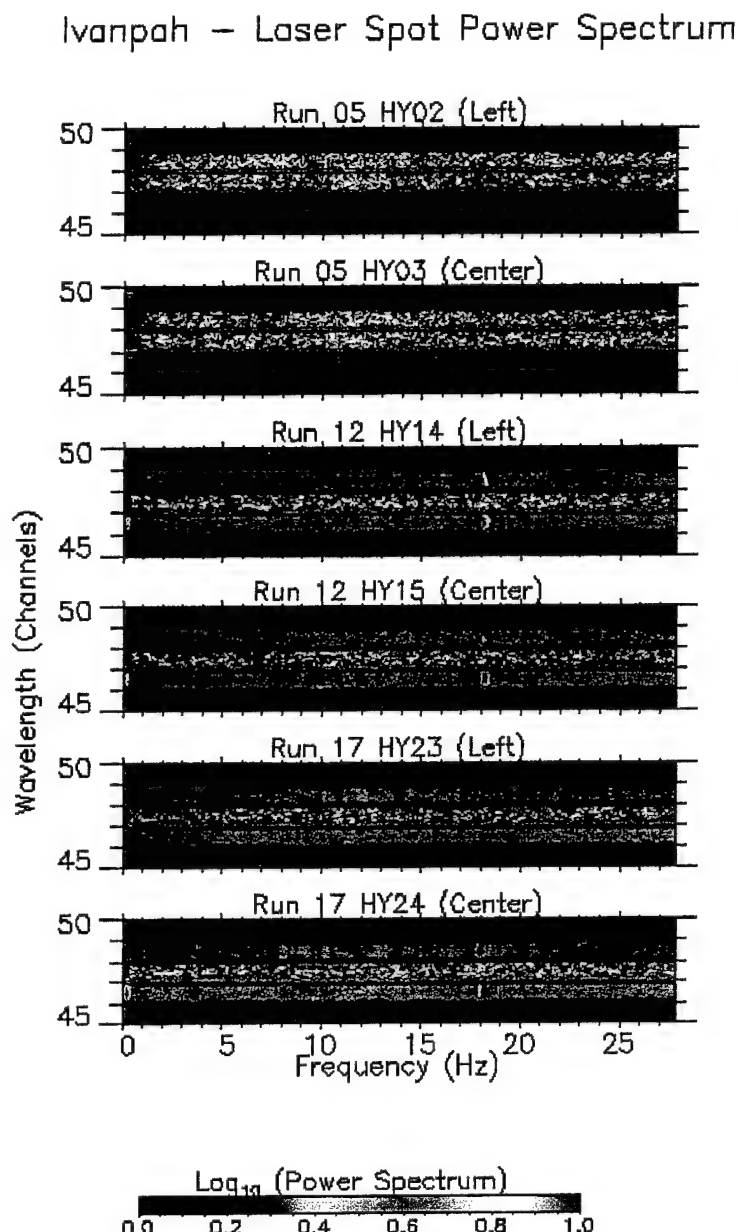
Figure 2.9: Laser Spot Power Spectrum from Ivanpah. This figure shows the Spectral Shift of laser power from bands 47 and 48 in Run 05 to bands 46, 47, and 48 in Run 17.

4. Geometric Distortion

This distortion is a result of the sensor mounting to the platform. There is a small amount of wandering that the sensor does combined with an 8 to 9 Hz resonance that results in a wavy image. The edge of a flight line varies up to 4 pixels in the cross track direction. No corrections have been identified, but the problem continues to be investigated.

5. Flight Path Alignment

A small error has been seen due to a misalignment of the sensor slit with the perpendicular to the flight path of the aircraft. This misalignment is approximately one degree. The results can be seen in imagery where the corners of some buildings are not exactly 90 degrees.

6. Smile

Two factors contribute to the center wavelength shifting slightly from column to column within a given row of detector elements. The first is the slight rotational misalignment of the slit causing the projection of a given wavelength to be misaligned with the rows of elements. The second factor, which will occur even for a perfectly aligned slit, is the spectrometer smile. This is a result of the geometric path followed by a given wavelength photon that results in a smile when projected on the FPA.

7. Band to Band Co-registration Error

For the some of the same reasons discussed previously, there is some error in registration of spatial information to the appropriate column of detector elements. The shift in spatial registration along a column is plus or minus 0.2 pixels relative to the position of the pixel at 1000 nm.

8. FPA Scratch

The FPA was scratched during production when integrating the Dewar assembly. This scratch extends from row 23 to row 70 and causes up to 40% degradation of signal on the affected elements. The scratch can be seen in the right hand side panels of Figure

2.6. Some data sets may show some slight residual due to the scratch, but for the most part the problems caused by the scratch are corrected on the radiometrically calibrated data.

9. Bad Detector Elements

Approximately 0.23% of the elements on the FPA are inoperative. These elements are effectively masked and are corrected for using a bilinear interpolation of neighboring elements.

10. Calibration Sequence

The flight calibration sequence consists of five major frames of data as seen in Figure 2.6. The sensor is operated in the calibrate mode with the integration times and frame times set for the next (or last) image run. The first major frame is taken while a shutter closes in front of the viewing window to collect focal plane offset levels. The FCU is then cycled through the three required positions to illuminate all pixels. The last major frame is another offset check by closing the shutter in front of the slit.

III. LITTORAL RADIANCE II EXPERIMENT

A. GENERAL

The Littoral Radiance II (LR-II) experiment was designed to extend hyperspectral imaging (HSI) techniques for support to military operations (SMO), while addressing a number of HYMSMO Program Level of Information (LOI) objectives. The experiment included participation in the amphibious operations and littoral warfare training exercises of the U.S. Marine Corps (KERNEL BLITZ Exercise-97). This exercise was conducted from the 12th through the 16th of June 1997. Data were collected over San Diego, San Clemente Island, and Camp Pendleton. The Camp Pendleton collect had components in the "Red Beach" area, the LCAC facility, and the Camp Pendleton airfield.

Only the Camp Pendleton airfield portion of LR-II will be discussed in detail here. A complete description of the LR-II collect is detailed in Ground Truth Reports that can be obtained from the HYMSMO Program Office.

Figure 3.1 is derived from a LANDSAT image of southern California on May 8, 1996. The base image is a gray scale image of LANDSAT band 7. The middle image is a map to give local reference to the LANDSAT image. The final image is a RGB view taken from the LANDSAT image from bands 7-4-2 expanded to show the location of the Camp Pendleton airfield. The runway lies northeasterly with the support buildings below and to the right.
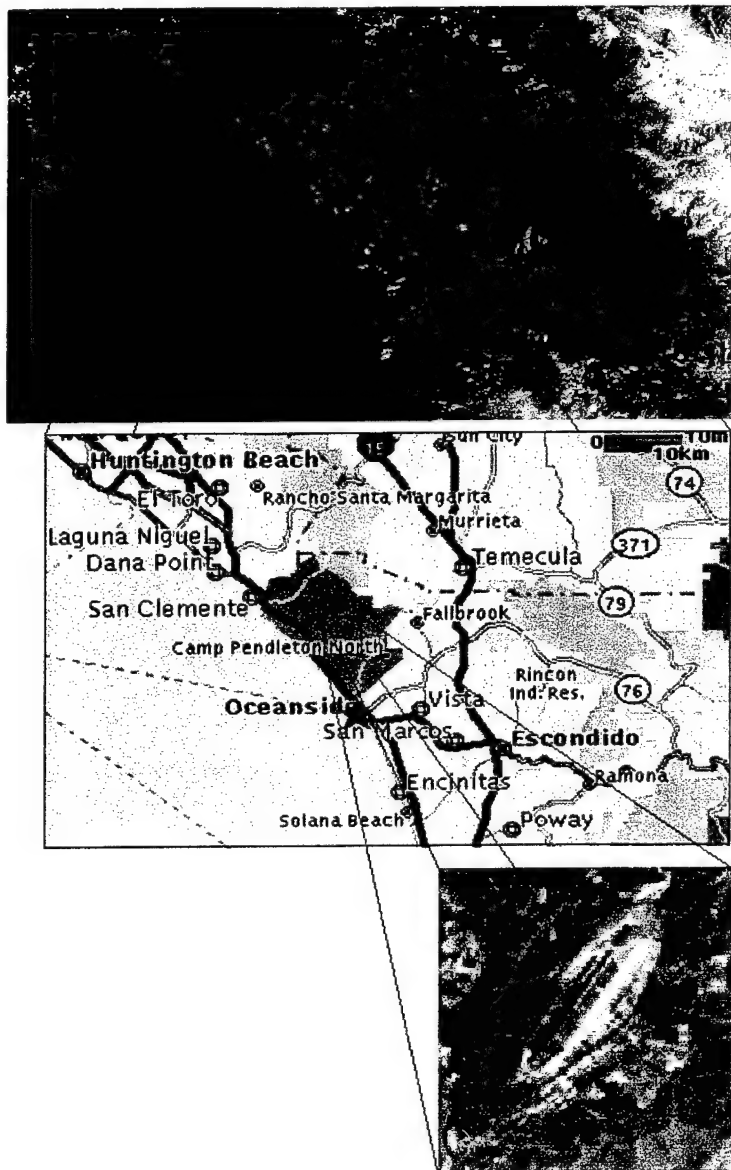
Figure 3.1: LANDSAT image of the southern California coast. Base image is LANDSAT band 7. Lower image is a color RGB image using bands 7, 4, and 2.

B. AIRFIELD

Figure 3.2 below shows an aerial view of the airfield on Camp Pendleton. The runway is at the bottom of the picture, a large helicopter parking area is seen in the middle of the image, and the top of the picture shows the airport support facilities. A

number of standard HYMSMO fabric and CARC panel targets were placed in the airfield (in and around the support facilities) scene to generate a cluttered target array for exploitation.

In the extreme upper right corner of Figure 3.2 (too small to see), there are six varying gray calibration panels. The airfield calibration panel site was located on a newly paved parking lot located between Building 2380 and Vandegrift Boulevard. The six pads were placed along with a spectral panel, a magic target, and two black rubber mats.

Figure 3.2: Aerial photograph showing the airfield at Camp Pendleton.

C.   CALIBRATION PANELS

The calibration panels were placed in the airfield area during HYDICE flights to support Empirical Line Method atmospheric scattering and attenuation removal to obtain target ground reflectance. These ground reflectance data was then used to test target detection algorithms and the atmosphere removal techniques that are commonly used. The calibration panel setup uses a six step gray scale with a known uniform reflectance, within the near ultraviolet to short-wave infrared region. These panels are 9.1 x 9.1 m with nominal reflectance levels of 2, 4, 8, 16, 32, and 64 percent. The panels are Dacron

substrate with an acrylic top coating. Figure 3.3 shows the relatively flat spectral signatures of the six calibration panels from the ultra violet to the short wave infrared regions of the electromagnetic spectrum.

Cal Panel Spectra (averaged)
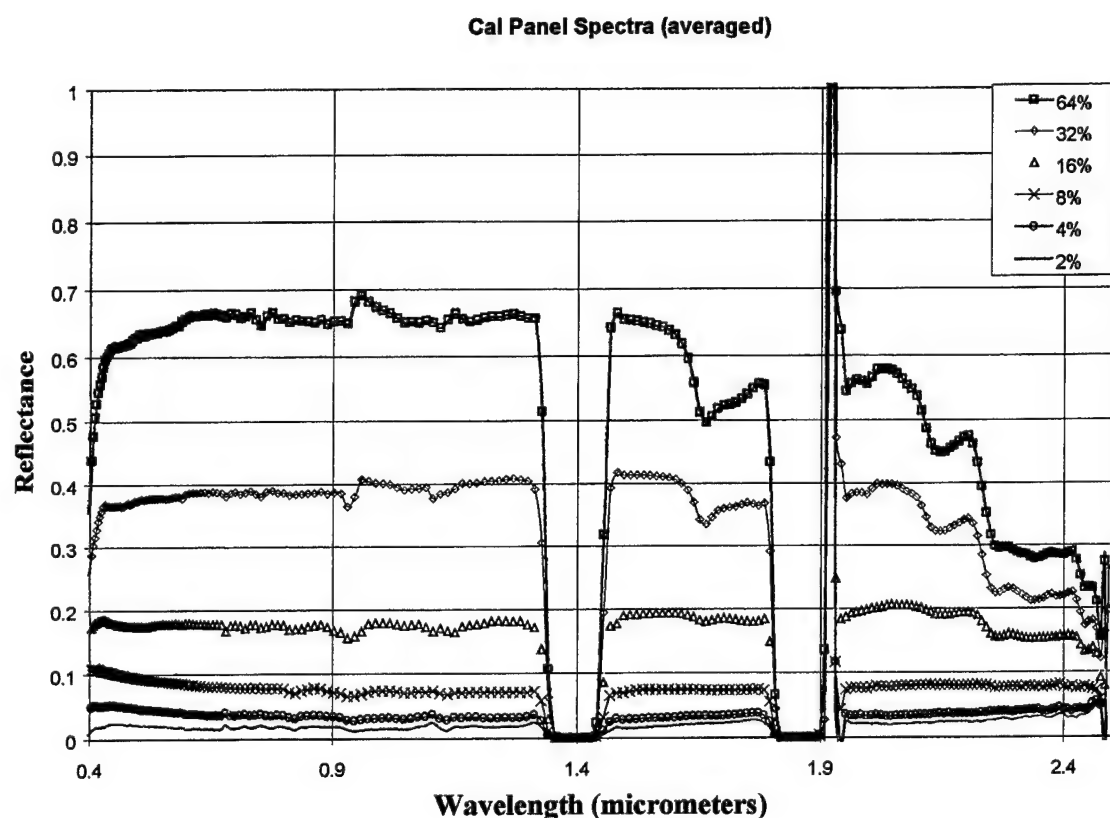
Figure 3.3: Reflectance verses Wavelength for the six step gray scale at Camp Pendleton airfield.

A sketch of the calibration panels and how they were setup is shown in Figure 3.4.
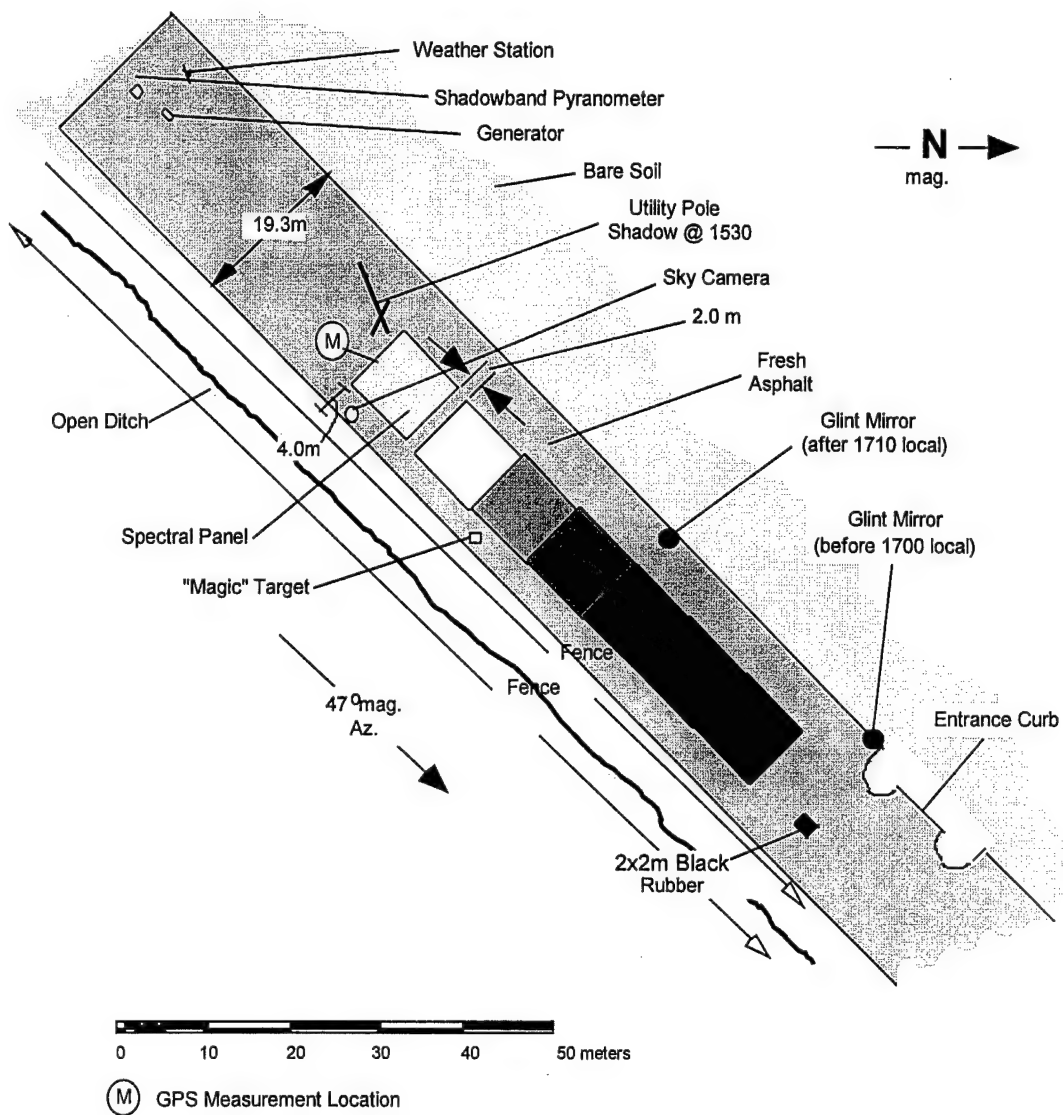
Figure 3.4: Six-step gray scale calibration panel setup at Camp Pendleton airfield. From MTL Systems, Inc. Ground Truth Report Vol. 2, page 14.

A ground level photograph of the calibration panels is shown in Figure 3.5.
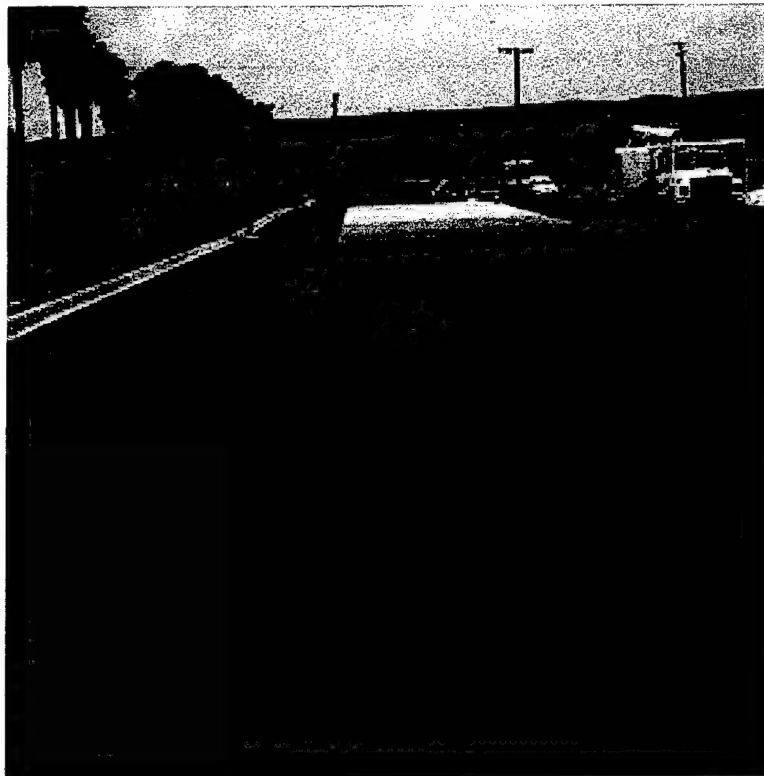
Figure 3.5: Photograph of the Calibration Panel setup at Camp Pendleton airfield.

This parking lot site also contained a "glint" mirror positioned along the north edge of the paved area (not shown in Figure 3.5). The mirror was adjusted periodically to maintain a visible reflection directly overhead. An automated surface weather station was set-up just southwest of the spectral panel.

D. SPECTRAL PANEL

A spectral calibration panel was located above the gray scale as shown in Figure 3.4. The spectral signature of this panel has several sharp absorption bands at known wavelengths. This panel is a polyester substrate with a nominal reflectance near 64 percent. The flight measurements over this panel clearly show all absorption bands and are plotted for comparison in Figure 3.6.
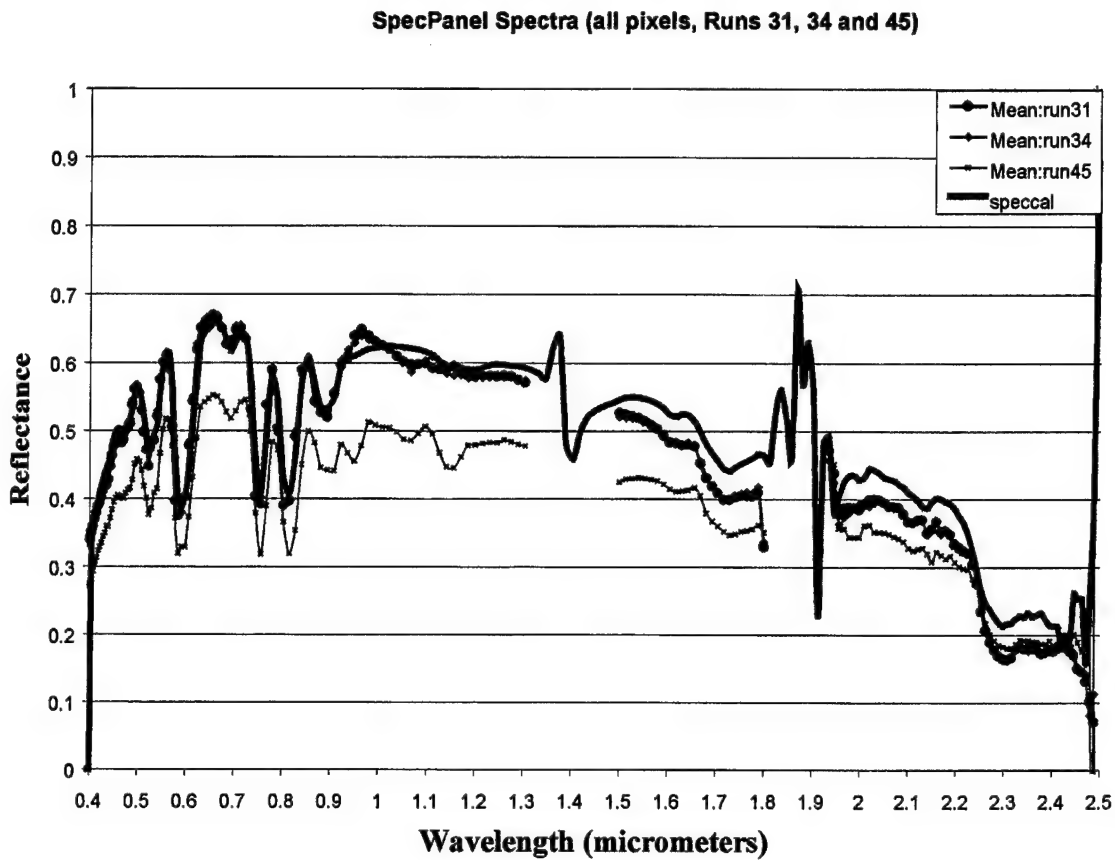
Figure 3.6: Reflectance vs. Wavelength for the Spectral Calibration Panel at Camp Pendleton airfield.

E. GROUND TRUTH

Ground truth services provided by MTL Systems, Inc. at Camp Pendleton included the calibration array and spectral panel deployment, atmospheric data acquisition, contact temperature sensor deployment and data acquisition, and spectroradiometric measurements of selected surfaces. Specifically, the ground truth important for this thesis included:

1. Spectral reflectance of the six-step gray scale calibration and spectral panels.

2. Spectral reflectance of background materials in the vicinity of the calibration panels.

3. Spectral reflectance of selected scene elements (building and roof surfaces). Building 2387 (roofs and walls), Building 2396m (roof and wall), Building 2368 (roof and wall), and Building 2386 (roof and wall).

4. Cloud cover and scene photographic documentation.

5. Atmospheric conditions: air temperature, relative humidity, and barometric pressure.

6. Geo-positioning data for panel deployment, and site sketches.

F.   SPECTRORADIOMETER

The spectroradiometric information in the VNIR and SWIR was obtained using the Geophysical Environmental Research Mark IV (GER) spectroradiometer. The spectroradiometer was positioned over the surface being measured using a boom truck. Several measurements of each surface were completed for averaging the spectra. The GER spectroradiometer was radiometrically calibrated with a standard traceable to the National Institute of Standards and Technology (NIST).

G.   DEPLOYED TARGETS

The targets that were deployed at the airfield on 15 June 1997 were standard HYMSMO targets with varying spectral profiles. The list below are the targets that had enough ground truth information available to perform studies pertinent to this thesis. All dimensions are given in meters.

- F1c Desert BDU 1X1
- F3a Solid Green Cotton Oxford fabric 3X3
- F3c Solid Green Cotton Oxford fabric 1X1
- F4a Nylon Poncho material, woodland camo pattern 3X3
- F4c Nylon poncho material woodland camo pattern 1X1
- F5c Cotton/Nylon woodland pattern BDU material 1X1
- F8 Brown fiberglass panel .6X.6

- F12a Nomex/kevlar BDU material, Woodland Camo pattern 3X3
- F12c Nomex/kevlar BDU material, Woodland Camo pattern 1X1
- F13b Nylon, light olive colored parachute material 2X2
- P3 Tan CARC paint on aluminum panel .6X.6
- P5 Green CARC paint on aluminum panel .6X.6

A few representative targets are shown here for context. Specific comments are made about some of the targets in regard to the Blind Test of Chapter Three. Note, for example, in Figure 3.7, the relatively high complexity of the area around the target.

Figure 3.7:   Target F1c, Desert BDU Material 1m X 1m.

The green cotton oxford fabric (F3a) is similar to the fabric covering the adjacent trucks in Figure 3.8. By contrast, the deployment in the grassy area (Figure 3.9) is more typical of previous HYMSMO collects (e.g. Forest Radiance). Target F3a was detected by all detection algorithms used during the blind test study detailed in Chapter 3.
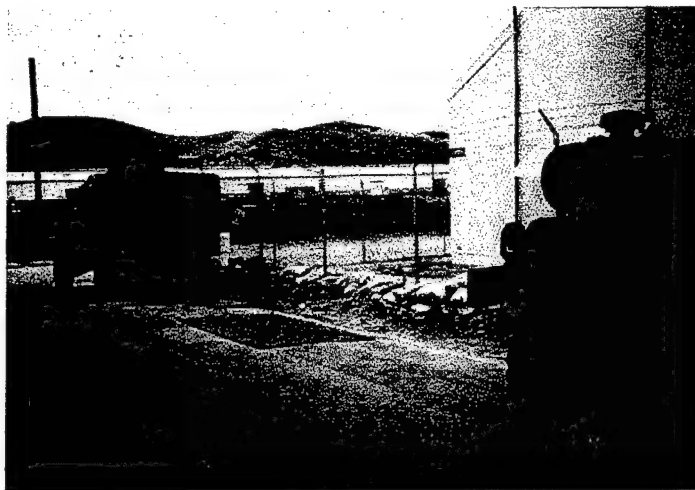
Figure 3.8: **Target F3a, Green Cotton Oxford Fabric 2m X 3m.**

Figure 3.9: **Target F3c, Green Cotton Oxford Fabric 1m X 1m.**

The smaller green cotton oxford target's (F3c) spectral signature is similar to the vegetation surrounding it. These surroundings combined with its relatively small size make this a difficult target to detect from the altitudes that were flown in Littoral Radiance II.

The nylon poncho (F4a) is one of the large targets, but was detected by only one of the standard algorithms. It was much more difficult than Target F3a, apparently due to the close placement of this target to the adjacent building, as illustrated in Figure 3.10.

Figure 3.10: Target F4a, Nylon Poncho Material, Woodland Camouflage Pattern, 3m X 3m.

Figure 3.11: Target F5c, Cotton Nylon Woodland Pattern BDU Material, 1mX1m.

Target F5c, shown in Figure 3.11, was not imaged from the lower altitude flights of five thousand feet. It was included in the ten thousand foot run with no detection success. The size and placement of this target made this a difficult detect.

Figure 3.12 shows the smaller of two targets made from the Nomex/Kevlar material that were deployed at the Camp Pendleton airfield. Like Target F5c, F12c was not imaged from five thousand feet. This target was not detected by any algorithms used in the "blind test".
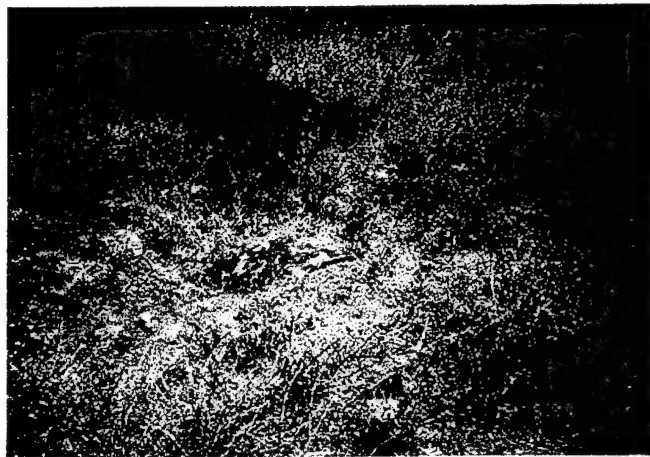
Figure 3.12: Target F12c, Nomex/Kevlar Woodland Camouflage Material.

Figure 3.13 shows one of the larger targets deployed placed in an area leading to difficult detection. The spectral signature of this material is similar to the grass that it rests on and was in partial shadow for both flight runs that imaged this target. F13b was detected only after the location of the target was revealed to the analyst.
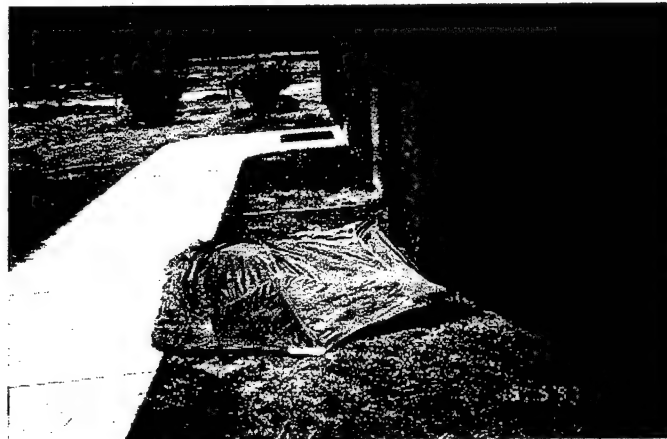
Figure 3.13: Target F13b, Nylon, Olive Parachute Material, Woodland Camouflage, 2m X 2m.

The targets shown in Figures 3.14 and 3.15 are small panels painted with different colors of CARC paint. This paint has distinct spectral signatures normally allowing for easy detection. However, neither P3 nor P5 were detected in this study. This was an unexpected result leading to a detailed analysis of the target placement. The missed detection was possibly due to the nearby walls, which can dramatically change the local illumination of the area. It was also discovered that both targets were in the shade during the flights that imaged these targets.

Figure 3.14: Target P3, Tan CARC paint on aluminum panel, 0.6m X 0.6m.
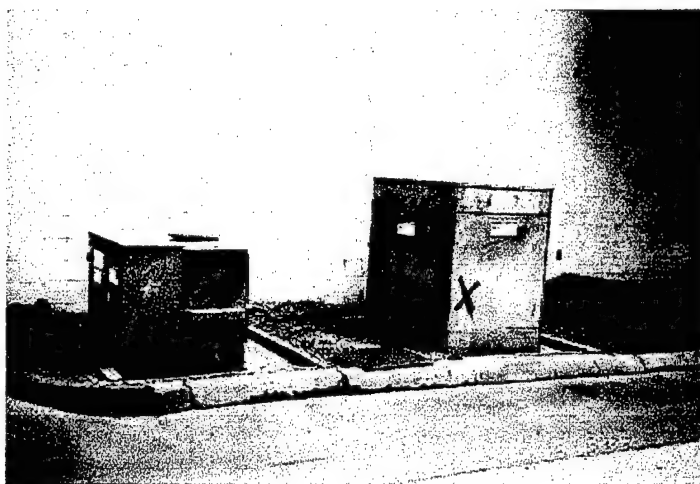
Figure 3.15: Target P5, Green CARC paint on aluminum panel, 0.6m X 0.6m.

H. FLIGHT COVERAGE

The flight lines covering the Camp Pendleton airfield were lines 9 through 12. These flight lines are shown in Figure 3.16 with details presented in Table 3.1. The flights studied and presented in this thesis are line 9 (runs 27 and 42), line 10 (runs 31 and 45), and line 11 (run 34). These lines were exploited because they covered the deployed target area, included flights at both 5,000 feet and 10,000 feet, and included the calibration panels in their respective scenes.
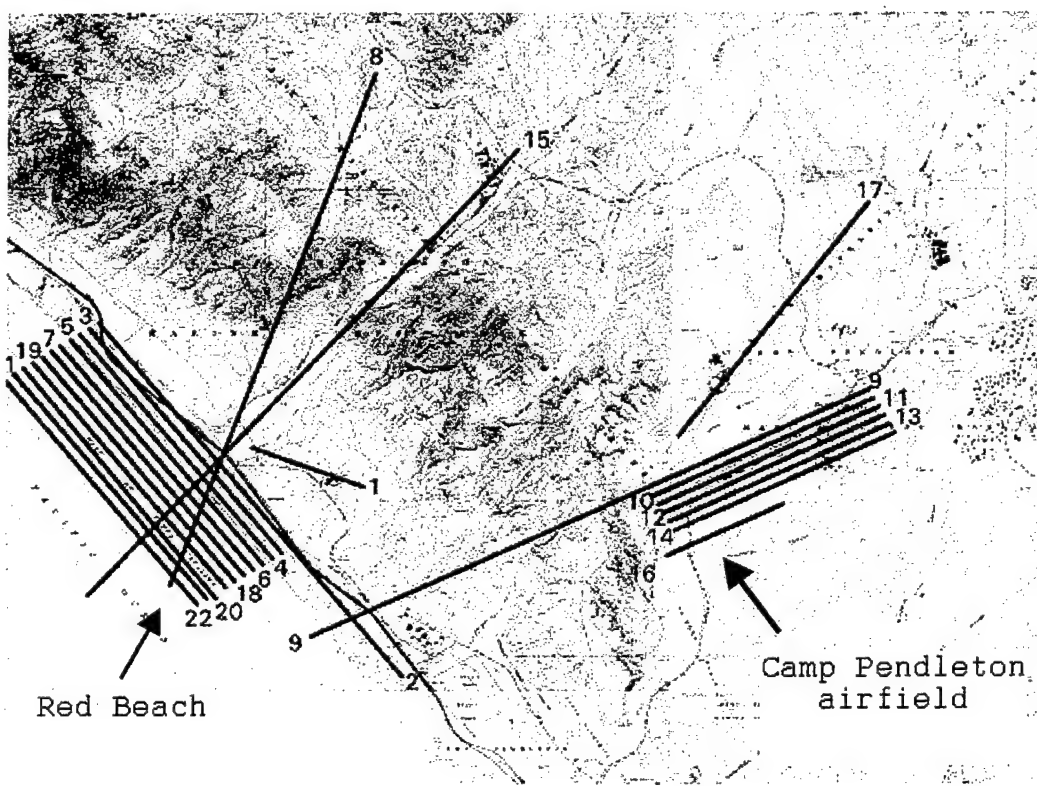
Figure 3.16: Chart showing the flight lines over the airfield and Red Beach areas at Camp Pendleton.

The airfield flight lines are on the right half of the figure. The length of the flight lines is on the order of a kilometer. The time needed to fly over the entire airfield area at varying altitudes accounting for instrument calibrations, etc. is on the order of two hours.

Table 3.1 contains the time and date information for only the flight lines that I studied. The complete details for all others can be obtained from the ground truth report put out by the HYMSMO Program Office. The major frame numbers are included to show what portion of the given flight line was exploited. A discussion of major frames is located in Chapter 2 of this thesis. The time and altitude data included in this table are important for addressing the affects due to bi-directional reflectance and altitude differences.

Table 3.1: Camp Pendleton HYDICE flight information June 6, 1997.

Flight Line	Time	Major Frames	Altitude (feet)
9	1656	11-49	5,413
9	2123	6-29	10,593
9	2239	6-45	5,370
10	2146	10-19	10,601
10	2254	73-90	5,397
11	2159	45-55	10,594
11	2315	29-43	5,396
12	2220	12-23	10,573
12	2340	25-45	5,386

I. SUMMARY

The Littoral Radiance II (LR-II) Collection occurred over ten days and covered six different sites. These sites included collection operations for HYMSMO LOI's and the Kernel Blitz-97 Exercise. LR-II covered urban targets, rural targets, and water targets both submerged and on the surface of the water.

The concentration of this thesis is on the Camp Pendleton airfield where standard HYMSMO targets and calibration panels were deployed. The studies completed on these targets included a blind test, the effects of bi-directional reflectance on hyperspectral images, and effects of changing altitudes on image resolution.

IV. BLIND TARGET TEST DESCRIPTION AND SETUP

A. HYMSMO METHODOLOGY

The HYMSMO program office has been conducting hyperspectral collection experiments since FY-94. These series of experiments have been designed to demonstrate the capabilities of hyperspectral remote sensing instruments and exploitation techniques. Collection experiments have been conducted in many types of environments ranging from desert to forest to sea. The data collected from these experiments is expansive and requires extensive man-hours or even man-years to exploit all the science available in all of the collects conducted to date.

This thesis is an attempt to exploit only a fraction of the data set collected in Littoral Radiance II. A discussion of the LR II collection operation is presented in Chapter 2 with details covering the airfield area of Camp Pendleton for which this blind test was completed.

1. Information Objectives for Littoral Radiance II

Each HYMSMO collection experiment is designed to incorporate information objectives. These objectives were originally compiled from an extensive survey known as the Assured Support to Operational Commanders (ASOC) (Bergman page 49) and are called "Levels of Information" (LOI's). LOI's include Detect/Geolocate (DE/GE), Classify (CL), Discriminate (DI), Characterize (CH), Material Identification (MI), Functional Identification (FI), Unit Identification (UI), Quantify Material (QM), Quantify Time (QT), Point (PO), Track (TR), Predict (PR), Target (TA), Warn (WA), Map and Chart (MC), and Taggants (TG). These LOI's can fall into many different categories. This thesis deals with the category of Exposed Fixed Objects.

The Littoral Radiance II collect was conducted from June 10 to June 16 1997. Several objective goals were set for this collect including a blind target test. There were then several LOI's associated with this blind test including Detect/Geolocate (DE/GE),

Material Identification (MI), and Characterize (CH). By addressing priority LOI's several capabilities inherent to the process can be improved upon or demonstrated. Every data set, when analyzed should provide means for improving exploitation algorithms, exploitation techniques, and potential for hyperspectral data dissemination to the user.

2. Detect and Geolocate (DE/GE)

Several different materials were placed in varying locations in and around the airfield site at Camp Pendleton. The materials used are standard HYMSMO fabric panels and are listed in Table 4.1. Using detection algorithms and spectral analysis, attempts were made to detect and geolocate each target. Results are listed in the following chapter.

Table 4.1: Target Material Panels at Camp Pendleton Airfield.

Target Designator	Material	Panel Size
F1c	Desert BDU	1m X 1m
F3a	Solid Green Cotton Oxford fabric	3m X 3m
F3c	Solid Green Cotton Oxford fabric	1m X 1m
F4a	Nylon Poncho material, woodland camouflage pattern	3m X 3m
F4c	Nylon poncho material woodland camouflage pattern	1m X 1m
F5c	Cotton/Nylon woodland pattern BDU	1m X 1m
F8	Brown fiberglass panel	.6m X .6m
F10	Tan Tenting	3m X 3m
F12a	Nomex/kevlar BDU material, Woodland Camouflage pattern	3m X 3m
F12c	Nomex/kevlar BDU material, Woodland Camouflage pattern	1m X 1m
F13c	Nylon, light olive colored parachute	2m X 2m
P2	Tan CARC paint on aluminum panel	.6m X .6m
P5	Green CARC paint on aluminum panel	.6m X .6m

3. Material Identification (MI)

The objective of material identification goes beyond simply looking at an image and visually picking out a target by color or shape. Sometimes it is necessary to discriminate between an actual target and a decoy target that may be the same shape and color. It is necessary to be able to identify materials even when the spatial resolution is not sufficient to visually identify the material. By using existing detection techniques

applied to hyperspectral data, it is often easy to identify a material without ever looking at the image.

4. Characterization (CH)

The HYDICE sensor has 210 bands that can be analyzed ranging from the visible to the short wave infrared .4µm to 2.5µm. As an example of the utility of several spectral bands consider Figure 4.1a and 4.1b. These two materials are similar in the visible spectrum, so when viewed from a long distance they could be easily mistaken. They are both fabric and are green in color, but one may be used for parachutes and the other for tents or covering truck beds. These fabrics have completely different uses and require discrimination between them.

(a)   (b)
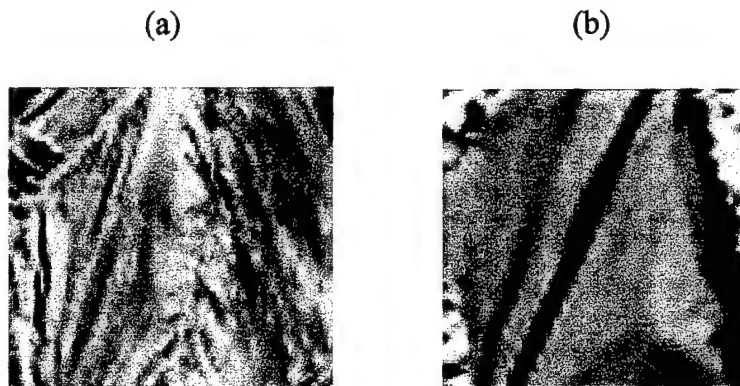
Figure 4.1: Green Fabrics (a) Olive Green Nylon Parachute Material. This material is a standard HYMSMO target designated Target F13. (b) Green Cotton Oxford Fabric. This material is a standard HYMSMO target designated F3.

Although an algorithm is normally used to evaluate the similarities between spectra for given materials, evaluation may also be conducted by visually analyzing a plot of the data spectra. Figure 4.2 on the next page contain plots of the spectra corresponding to Figures 4.1a and 4.1b. In the visible region both plots show relatively high values near the green region of the spectrum, but without knowing what the materials are the features are not extraordinary. The distinguishing features are clearly seen in the infrared regions. For the parachute material there is a strong dip in energy near the 1.6 µm to 1.7 µm

bands. The corresponding wavelengths in the green cotton show a pronounced peak in energy. There are also some distinguishing features in the 2.0 μm to 2.3 μm ranges. The parachute material has two familiar energy dips in this region, where the green cotton only has one. The inherent value of (CH) using hyperspectral data is a clear strength of hyperspectral imaging technology.

F3 Spectra compared to F12 Spectra
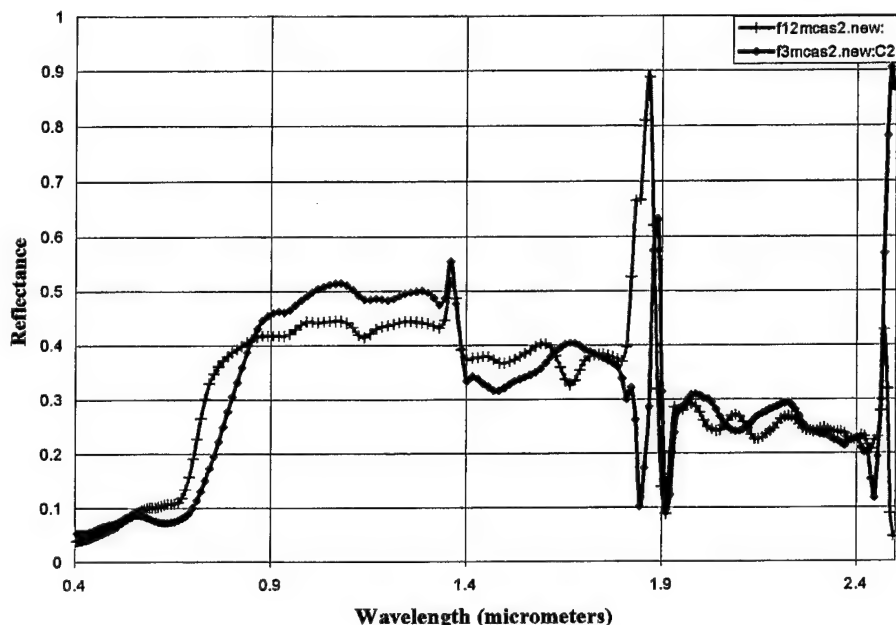
Figure 4.2: MTL Systems, Inc. sampled all target spectra for supplying Ground Truth support for LR II. Spectral plots shown to examine differences between similar green target materials.

B.   EXPERIMENT OBJECTIVE

The experiment objective as defined by the LOI for this study is to detect the presence and determine the location of materials and/or material changes. This includes exposed fixed targets whose representation in conventional imagery (e.g., panchromatic, infrared, radar) lacks sufficient levels of spatial information to be detected, geo-located, and mapped through literal interpretation techniques. The objective assumes that candidate target materials' spectral, textural, or temporal signatures have already been

characterized. Several groups or organizations, as discussed in the ground truth portion of Chapter 2, completed this characterization.

C.   STATEMENT OF THE PROBLEM

Determine the utility of using hyperspectral imaging techniques for detecting and geo-locating blind targets. The emphasis on this particular experiment is to not only evaluate the ability of existing software and algorithms to assist an analyst in finding targets, but to explore second order LOI's that have not been addressed in detail to date. Second order objectives that will be evaluated subsequent chapters include bi-directional reflectance (BRDF) and altitude variation (AV) effects on hyperspectral data.

D.   PROCEDURE

Remove atmospheric effects from several data cubes obtained from HYDICE using ground truth data. Ground truth data from six gray calibration panels were used to convert the radiance data to apparent reflectance using Empirical Line Method (ELM). Various algorithms such as Spectral Angle Mapper (SAM) and Matched Filter (MF) were then employed to detect and locate target panels. After locating and characterizing all available targets, the effects of BRDF and AV on the data were investigated.

E.   BACKGROUND

1.   Solar Energy

Using the temperature of the sun at approximately 5900 °K, the Planck function is used to calculate the energy distribution per unit wavelength at the earth's atmosphere. This energy distribution is called Planck's radiation law for a black body emitter and is given by,

$$I(\lambda, T) = \frac{2\pi c^2 h}{\lambda^5} \frac{1}{e^{hc/\lambda kT} - 1} , \tag{4.1}$$

where λ is wavelength normally expressed in μm, T is temperature in K, c is the speed of light in m/s^2, h is Planck's constant in J-s, and k is Boltzman's constant in J/K.

39

Most of the solar energy transmits the atmosphere and can reflect off a given target for collection by a sensor. The wavelength range of the HYDICE sensor (.4µm to 2.5µm) includes three of the main atmosphere absorption bands at .94µm, 1.13µm, and 1.4µm. Energy at these wavelengths cannot penetrate the atmosphere due to absorption by H_2O and CO_2. The sensor data at these wavelengths result in little or no useful information for analysis.

2.   Radiance at Sensor

The second known parameter is the digital number value assigned by the sensor to represent the energy detected by a given pixel. Chapter 1 describes in detail the method used by the sensor to detect energy for a definitive spatial and spectral resolution. After all sensor calibrations are completed the data that is considered "raw" to the analyst is actually a value of radiance at the sensor. An example of this data is shown in Figure 4.3.
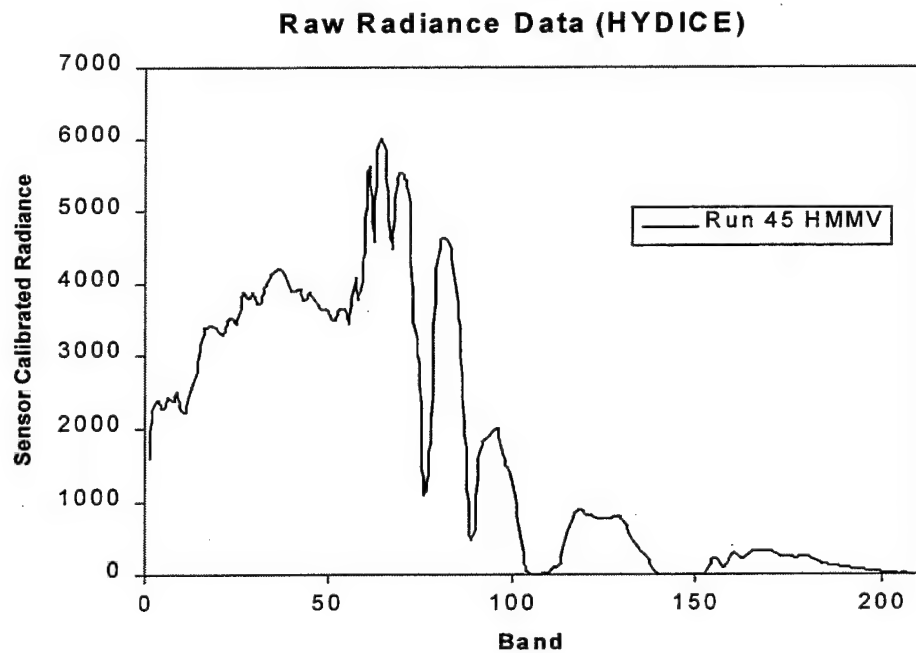
Figure 4.3: HMMV radiance spectra prior to atmosphere removal.   This plot represents the pixel spectra of the front hood of a HMMV parked in the scene of Run 45, Camp Pendleton airfield, LR II Experiment.

This data is not particularly useful until wavelength values replace the band values and reflectance values replace radiance values. To assign center wavelengths to the band values, a simple program is employed that makes use of the wave file that is supplied with the image data. Then the radiance is converted to apparent reflectance using one of several algorithms. The method used to convert to reflectance in this thesis was the Empirical Line Method (ELM).

3. Empirical Line Method (ELM)

ELM accounts for the atmosphere by fitting the sensor obtained data to known values of reflectance for a given material. This is done using existing reflectance (spectra) values obtained in a laboratory or in the field for a given material. Obtaining the spectra in the field using a portable spectroradiometer is the preferred method, but not always practical. Field data is preferred because the solar energy reaching the target would be the same for the data collected using the spectroradiometer and for the sensor in the aircraft.

ELM compares the ground truth data and the sensor data to obtain a linear regression that equates the Digital Number values for radiance to the reflectance of the target material. ELM calculations are performed using each wavelength band for each spatial pixel and results in correction coefficients for maximum solar irradiance, atmospheric path radiance, and a rms error value. After applying these corrections to the radiance data a much more useful data set is generated as seen in Figure 4.4. Figure 4.3 and Figure 4.4 both represent the same spatial pixel in the same scene. The latter figure shows the two humps characteristic of green CARC paint.

Converted Reflectance Data (HYDICE)
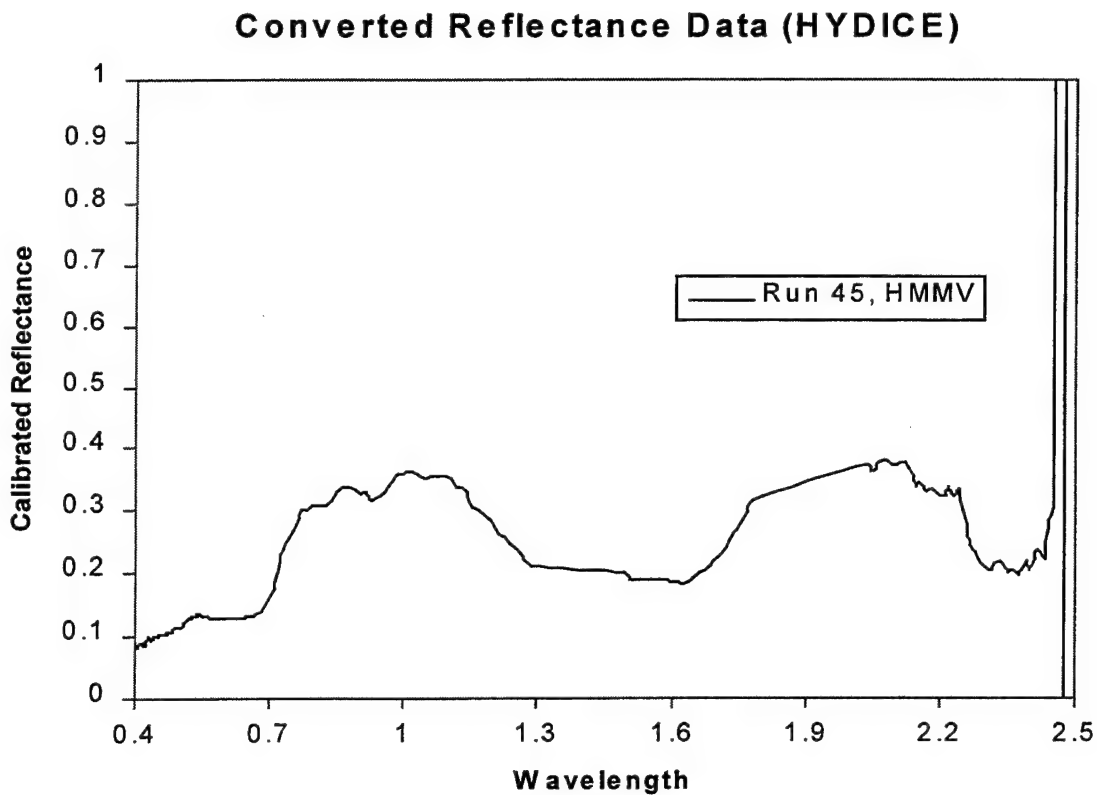
Figure 4.4: HMMV reflectance spectra after ELM calibration. This spectra represents the same pixel as in Figure 4.3 following application of atmosphere correction and normalization.

4.   Atmosphere Modeling

Other methods of atmosphere removal are used in cases where obtaining the ground truth data at the field site is not practical. ATREM and MODTRAN are two common algorithms currently used to remove atmosphere effects and require input values for air particulate, water vapor, etc. This information comes from an estimate of a "standard atmosphere" for the area or from actual atmosphere profiling using in situ measurements. It is important to note that hyperspectral imagery is greatly affected by any incorrect modeling of the atmosphere due to the high spectral resolution. Specific reasons for this are (Schowengerdt, pg. 321):

- "Hyperspectral sensor bands coinciding with narrow atmospheric absorption features, or the edges of broader spectral features, will be affected by the atmosphere differently than the neighboring bands.

- The band locations in imaging spectroradiometer systems are prone to small wavelength shifts under different operating conditions, particularly in airborne sensors.

- Many analysis algorithms for hyperspectral data require precise absorption band-depth measurements exactly at the wavelength of maximum absorption.

- From the computational standpoint alone, the calibration problem is much greater for hyperspectral systems."

5. Airfield Blind Test Scenario

In order to argue for or against the results of this experiment for target detection and geo-location it is necessary to point out what was known prior to the analysis. A list of targets was provided to set bounds on the blind test problem. However, not all targets were required to be in the scene and the number of occurrences of each target was unknown. The targets were listed as material type only, without revealing size, function, or location.

The HYDICE sensor imaged the airfield area using four different flight lines, of which each were flown at varying altitudes. The original design for this experiment included the HYDICE sensor and the SEBASS sensor with flight altitudes of 2,500, 5,000 and 10,000 feet. However, the SEBASS sensor did not end up participating in the experiment so only the 5,000 feet and at 10,000 feet altitudes were flown.

F. METHODOLOGY

1. Radiance to Apparent Reflectance

To generate the necessary baseline data for this study, the radiance data cubes provided by the HYDICE scenes were converted to apparent reflectance. As previously

mentioned, there are several options for converting the data to reflectance. To narrow the scope of this experiment Empirical Line Method, rather than atmospheric modeling and removal algorithms, was used to obtain the base data set. Empirical Line Method assumes a homogeneous atmosphere throughout the scene. The airfield area is small enough for this assumption to be valid. Also, the adjacency effects due to the background, fresh black top pavement near the calibration panels, did not introduce significant error in the correction calculations for the rest of the scene. Ground truth information from six varying gray calibration panels located at the airfield allowed direct removal of the atmospheric column using the Empirical Line Method. Obtaining ground truth data necessary for ELM in a hostile situation or a "real world" target detection situation is not normally feasible. However, the goal of this study was not to evaluate atmospheric modeling, only to obtain the most accurate reflectance data possible.

2. Target Detection Analysis

Flight lines 10 and 11 were analyzed more closely then 9 and 12 due to the coverage area and the availability of calibration panels within the scene. The detection algorithms used required signature spectra of all targets as end-members. The target spectra used were averages of several data collects for each target material obtained at the airfield using a portable spectroradiometer.

The truth spectra were applied to the Matched Filter (MF) and Spectral Angle Mapper (SAM) algorithms in the ENVI software program for analysis and target detection. The technique used to analyze the data involved enhancing the algorithm result images using a linear stretch feature on the histogram. The results then included pixels with only the very best (smallest angular separation or highest correlation) target signature matches. Each pixel was then visually evaluated, comparing the detected pixel spectra to the target spectra.

G.   SUMMARY

The results for the initial blind test were obtained by using only the above listed SAM and MF algorithms.   Once the target locations were revealed, the Constrained Energy Minimization (CEM) and Low Probability of Detection (LPD) algorithms were run on all of the data.   This was done for comparison to the other algorithms previously run and to see if CEM or LPD easily detected any missed targets.

V. BLIND TEST OBSERVATIONS

This chapter summarizes initial observations from the LR II Blind Test including whether the targets were detected and or geo-located during algorithm application. The purpose of this compilation of data and results was to setup a second order test to study the effects of Altitude Variation (AV) and Bi-directional Reflectance Distribution Function (BRDF) on data obtained from the HYDICE sensor.

The initial observations for all targets are summarized in Table 5.1. The first two columns of the table list the target materials deployed in the airfield area. The third column lists the flight runs that imaged the target. The fourth column lists those targets detected using the different algorithms. When a target was identified by a given algorithm, but was hidden amongst many false targets, the algorithm was labeled with an asterisk. Column five lists whether a target was recognized as an actual target, among false targets, and recorded prior to the target locations being revealed.

Flight lines 10 and 11 included runs 31, 34, 45, and 47. Each run did not cover all of the targets. Run 31 covered all targets from 10,000 feet. Run 45 covered most of the targets from 5,000 feet. The targets that were not covered in Run 45 at 5,000 feet were F1c, F4c, F5c and F12c. Run 34 covered six of the fourteen targets at 10,000 feet, but did not result in strong conclusions like Runs 31, and 45. Run 47 was analyzed, but did not contribute to any findings since it did not cover any targets that were placed away from the calibration panels. Most of the following discussion results from runs 31 and 45.

A.   RESULTS REFERENCE TABLE

Table 5.1: Summary of Results for the Blind Test of standard HYMSMO fabrics at Littoral Radiance II, Camp Pendleton airfield.

Target Material	Size of Panel	Target Imaged by	Target Detected in Run (Algorithm used for detect)	Recorded as Target	Associated Figures
F1c Desert BDU Nylon/Cotton	1 X 1 m	Run 31 10K.	Not detected by any algorithms.	No	None
F3a Green Cotton	3 X 3 m	Run 31 10K, Run 45 5K, Run 34 10K.	Run 31 (SAM, *MF, LPD) Run 45 (SAM, MF, CEM, LPD) Run 34 (SAM, MF, CEM, LPD)	Yes	Figures 4.1, 2, 7
F3c Green Cotton	1 X 1 m	Run 31 10K, Run 45 5K.	Run 45 (*MF, *CEM)	No	
F4a Green Nylon	3 X 3 m	Run 31 10K, Run 45 5K.	Run 45 (*MF, *CEM) Run 31 (*SAM, MF,*CEM,LPD)	Yes	Figures 4.3, 4, 8
F4c Green Nylon	1 X 1 m	Run 31 10K.	Run 31 (*MF)	No	Figure 4.10
F5c Green Cotton/Nylon Blend	1 X 1 m	Run 31 10K.	Not detected by any algorithms.	No	
F8 Dark Brown Fiberglass	.6 X .6 m	Run 31 10K, Run 45 5K, Run 34 10K.	Not detected by any algorithms.	No	
F10 Tan Tenting	1 X 1 m	Run 31 10K, Run 45 5K.	Not detected by any algorithms.	No	
F12a Nomex/Kevlar Woodland Pattern	3 X 3 m	Run 45 5K, Run 31 10K.	Run 45 (*SAM, MF, CEM, LPD) Run 31 (*SAM, MF, LPD)	Yes	Figures 4.5, 6, 9
F12c Nomex/Kevlar Woodland Pattern	1 X 1 m	Run 31 10K.	Not detected by any algorithms.	No	
F13b Light Green Parachute	2 X 2 m	Run 31 10K, Run 45 5K.	Run 31 (*MF) Run 45 (*MF, *CEM)	No	Figure 4.11
P3 Tan CARC Painted Alum.	.6 X .6 m	Run 31 10K, Run 45 5K, Run 34 10K.	Not detected by any algorithms.	No	
P5 Green CARC Painted Alum.	.6 X .6 m	Run 31 10K, Run 45 5K, Run 34 10K.	Not detected by any algorithms.	No	
RSb Black Rubber Sheet	2 X 2 m	Run 45 5K, Run 31 10K, Run 34 10K.	Not detected by any algorithms.	No	

* Signifies that the target was found by this algorithm only after the location of the target was already known.

B.   DETECTION SUCCESSES (F3A, F4A, AND F12A)

Only three of the fourteen targets, F3a, F4a, and F12a were detected and decisively geo-located prior to the locations being revealed. These are listed in the "Recorded as Target" column of Table 5.1. The method used to detect the target and record the geolocation was to enhance the algorithm result by using a linear stretch of the histogram to minimize the false targets. Then each highlighted pixel following the enhancement was evaluated by inspecting the signature spectra. Several targets were detected by algorithm, but were not recorded as targets because of visual inspection of the spectra not matching expected ground truth spectra or because of a large number of false targets cluttering the scene.

1.   Run 31 Successes

Figures 5.1 and 5.2 show the SAM and MF results from run 31 for F3a. These are followed by Figures 5.3-5.6 to show results for F4a and F12a. For each target the full MF, RGB, and SAM image is shown. The RGB image is presented with minimal reduction in brightness and contrast in order to georeference between the images. These images shown in the first figure for each target contain a boxed area to show the general location of the target. The second figure for each target contains the expanded views of the boxed areas to discern individual pixels of interest. The top three expanded images represent the boxed areas using the same gray scaling as the full scene. The second row of three images represent these boxed areas after enhancement. Below the expanded views are the histograms showing the distribution of detection values for the two algorithms. The locations of the detected target pixels are indicated on the histograms.

Figure 5.1: The airfield at Camp Pendleton. These are HYDICE images from the Littoral Radiance II experiment, Run 31 at 10,000 feet. Left: Matched Filter result image for target F3a. Right: Spectral Angle Mapper result image for target F3a. A 3 X 3 meter square of green cotton, designated F3a, is in the center of the outlined (red box) area.
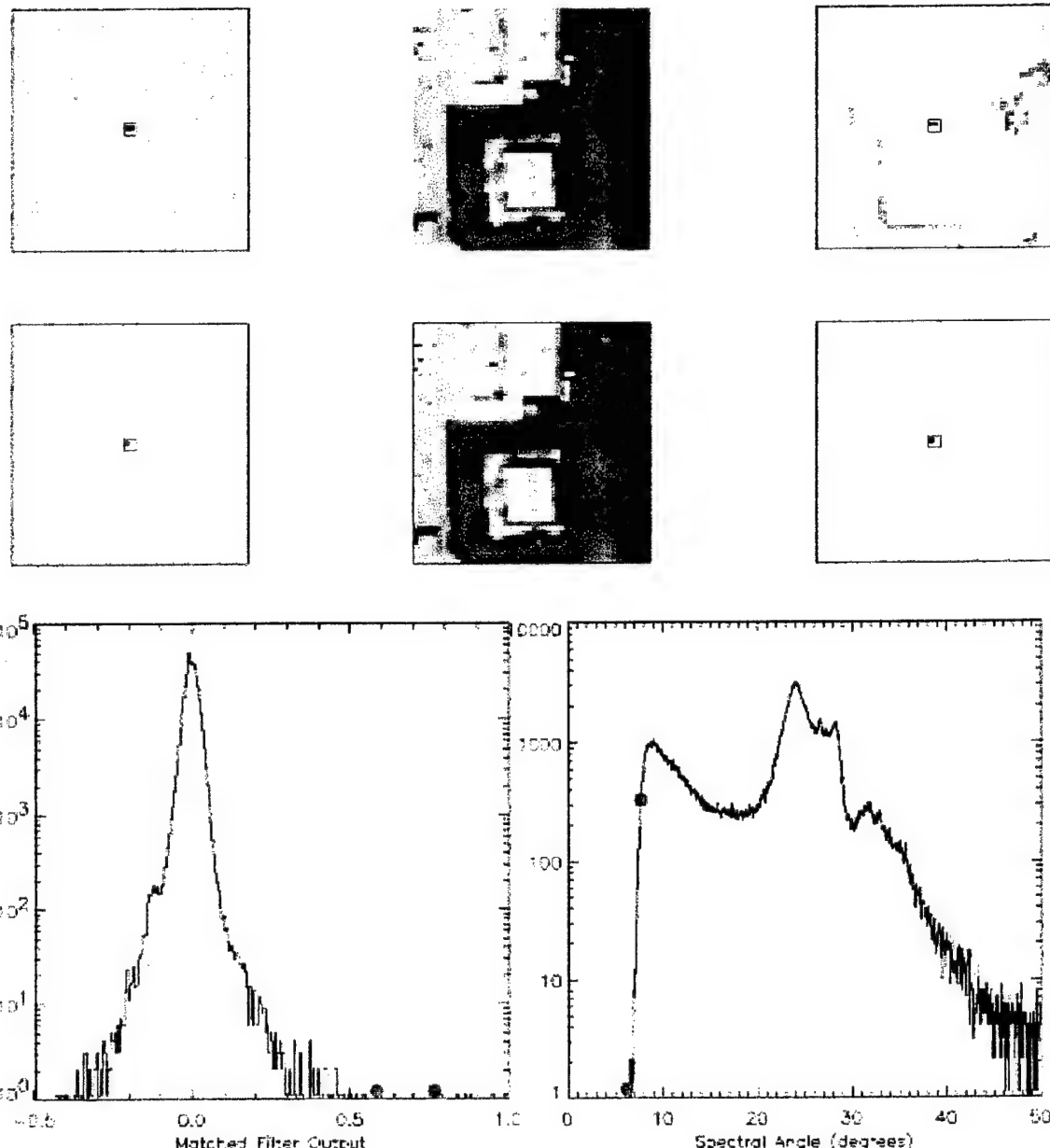
Figure 5.2: The top row contains enlargements of the boxed areas of Figure 5.1. The second row contains the same images enhanced to highlight the target of interest. Left: Matched Filter (MF) result image for target F3a. Center: RGB image of target area. Right: Spectral Angle Mapper (SAM) result image for target F3a. The histograms represent the MF and SAM results respectively, with the target pixels highlighted with red dots. The target pixel values detected by the MF algorithm are greater than ten standard deviations from the mean.

Figure 5.3: The airfield at Camp Pendleton. These are HYDICE images from the Littoral Radiance II experiment, Run 31 at 10,000 feet. Left: Matched Filter result image for target F4a. Right: Spectral Angle Mapper result image for target F4a. A 3 X 3-meter square of Green Nylon, designated F4a, is in the center of the outlined (red box) area.
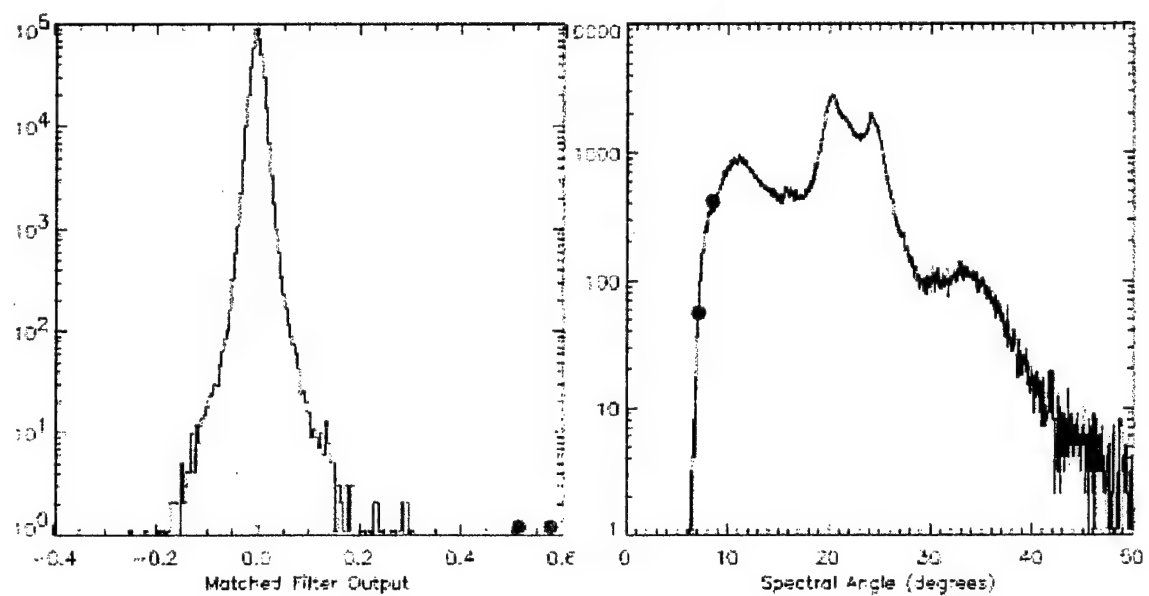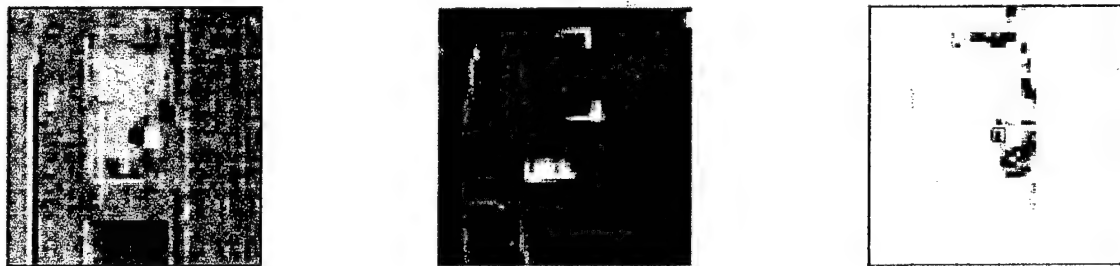
Figure 5.4: The top row contains enlargements of the boxed areas of Figure 5.3. The second row contains the same images enhanced to highlight the target of interest. Left: Matched Filter (MF) result image for target F4a. Center: RGB image of target area. Right: Spectral Angle Mapper (SAM) result image for target F4a. The histograms represent the MF and SAM results respectively, with the target pixels highlighted with red dots. The target pixel values detected by the MF algorithm are greater than ten standard deviations from the mean.
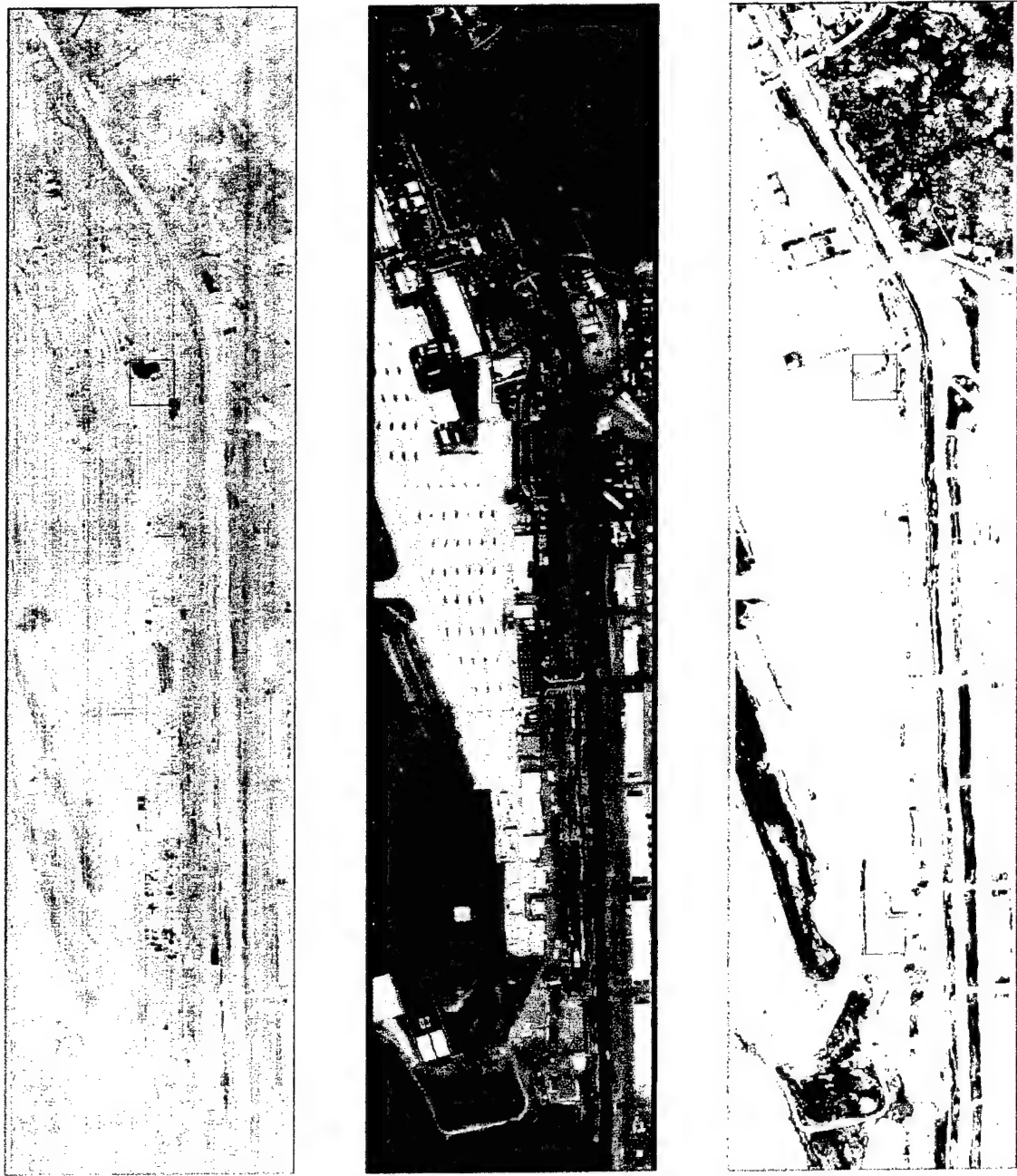
Figure 5.5: The airfield at Camp Pendleton. These are HYDICE images from the Littoral Radiance II experiment, Run 31 at 10,000 feet. Left: Matched Filter result image for target F12a. Right: Spectral Angle Mapper result image for target F12a. A 3 X 3 meter square of Nomex/Kevlar (woodland pattern), designated F12a, is in the center of the outlined (red box) area.
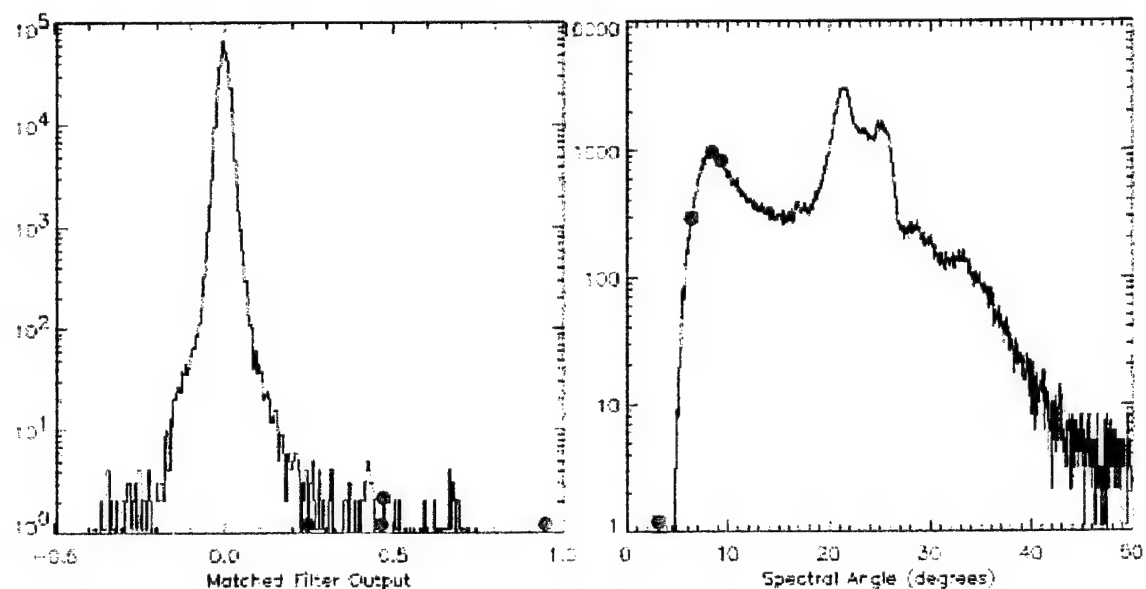
Figure 5.6: The top row contains enlargements of the boxed areas of Figure 5.5. The second row contains the same images enhanced to highlight the target of interest. Left: Matched Filter (MF) result image for target F12a. Center: RGB image of target area. Right: Spectral Angle Mapper (SAM) result image for target F12a. The histograms represent the MF and SAM results respectively, with the target pixels highlighted with red dots. The target pixel values detected by the MF algorithm are greater than four standard deviations from the mean.

2. Run 45 Successes

Figure 5.7 shows the SAM and MF results from run 45. The full-length RGB image is included for spatial reference with the target area highlighted (red box) for F3a. To the right of the full-length image are the MF and SAM results. The top row shows the target area enlarged by a factor of four with MF and SAM results respectively. The bottom row shows the same areas with the results enhanced to show only the target pixels. Figures 5.8 and 5.9 follow and show results for F4a and F12a.
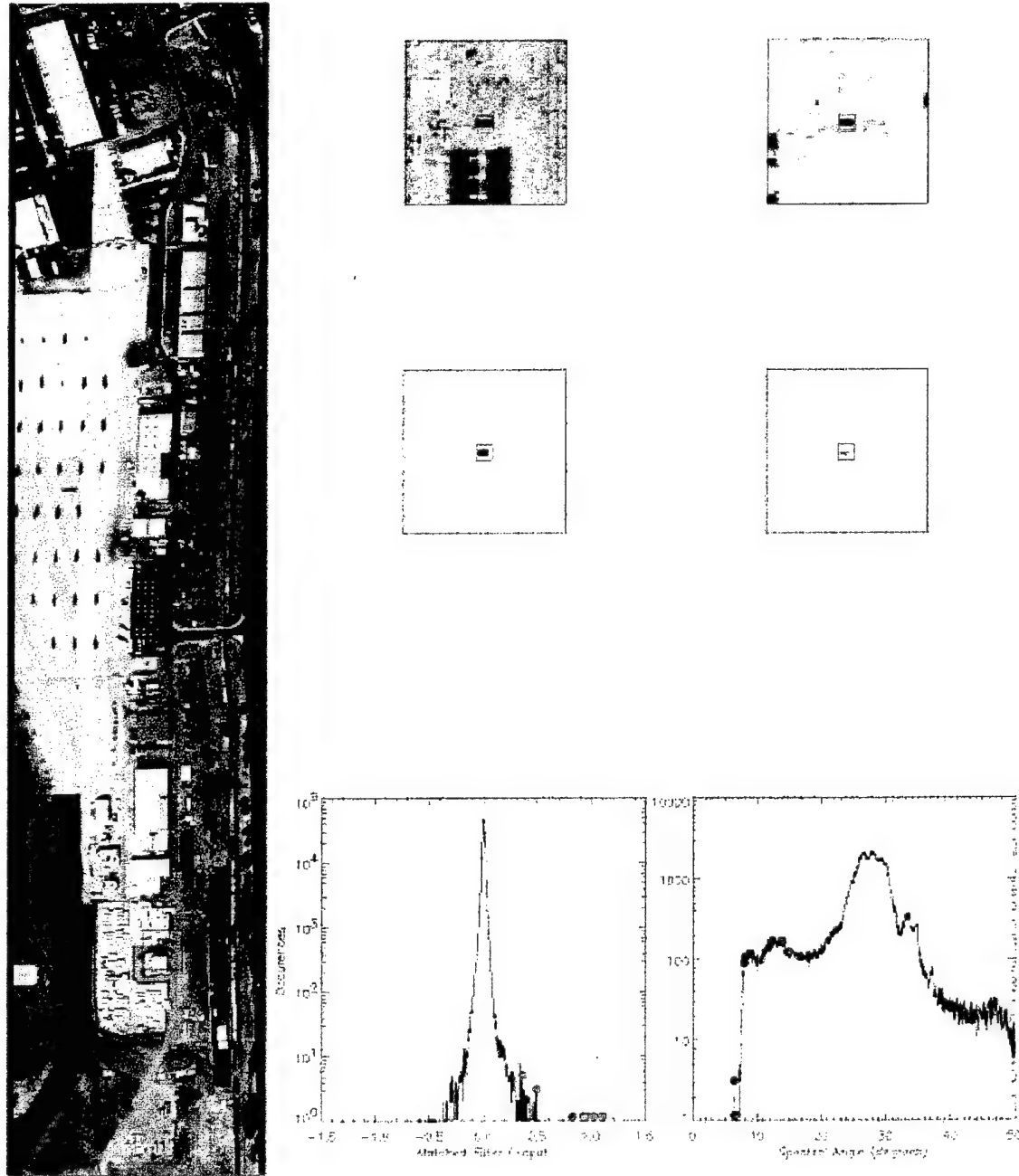
Figure 5.7: Left: HYDICE image of the airfield at Camp Pendleton, Run 45 at 5,000 feet. Top Row: Matched Filter and Spectral Angle Mapper results respectively, for target F3a in the outlined area. Second Row: Result images enhanced to highlight target pixels. Bottom Right: MF and SAM histograms with values for the F3a target pixels marked with red dots. The target pixel values detected by the MF algorithm are greater than five standard deviations from the mean.

57
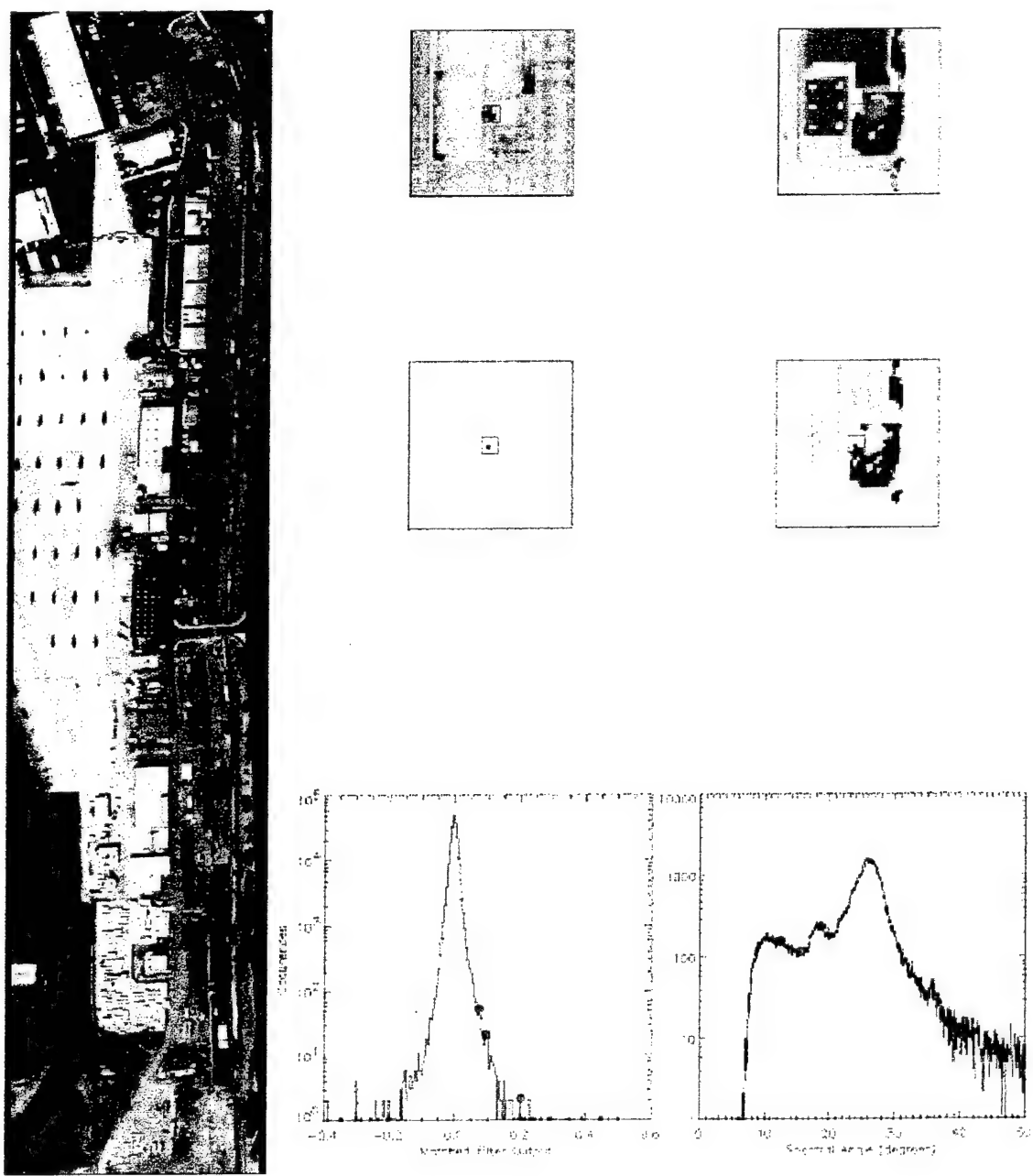
Figure 5.8: Left: HYDICE image of the airfield at Camp Pendleton, Run 45 at 5,000 feet. Top Row: Matched Filter and Spectral Angle Mapper results respectively, for target F4a in the outlined area. Second Row: Result images enhanced to highlight target pixels. Bottom Right: MF and SAM histograms with values for the F4a target pixels marked with red dots. The target pixel values detected by the MF algorithm are greater than three standard deviations from the mean.
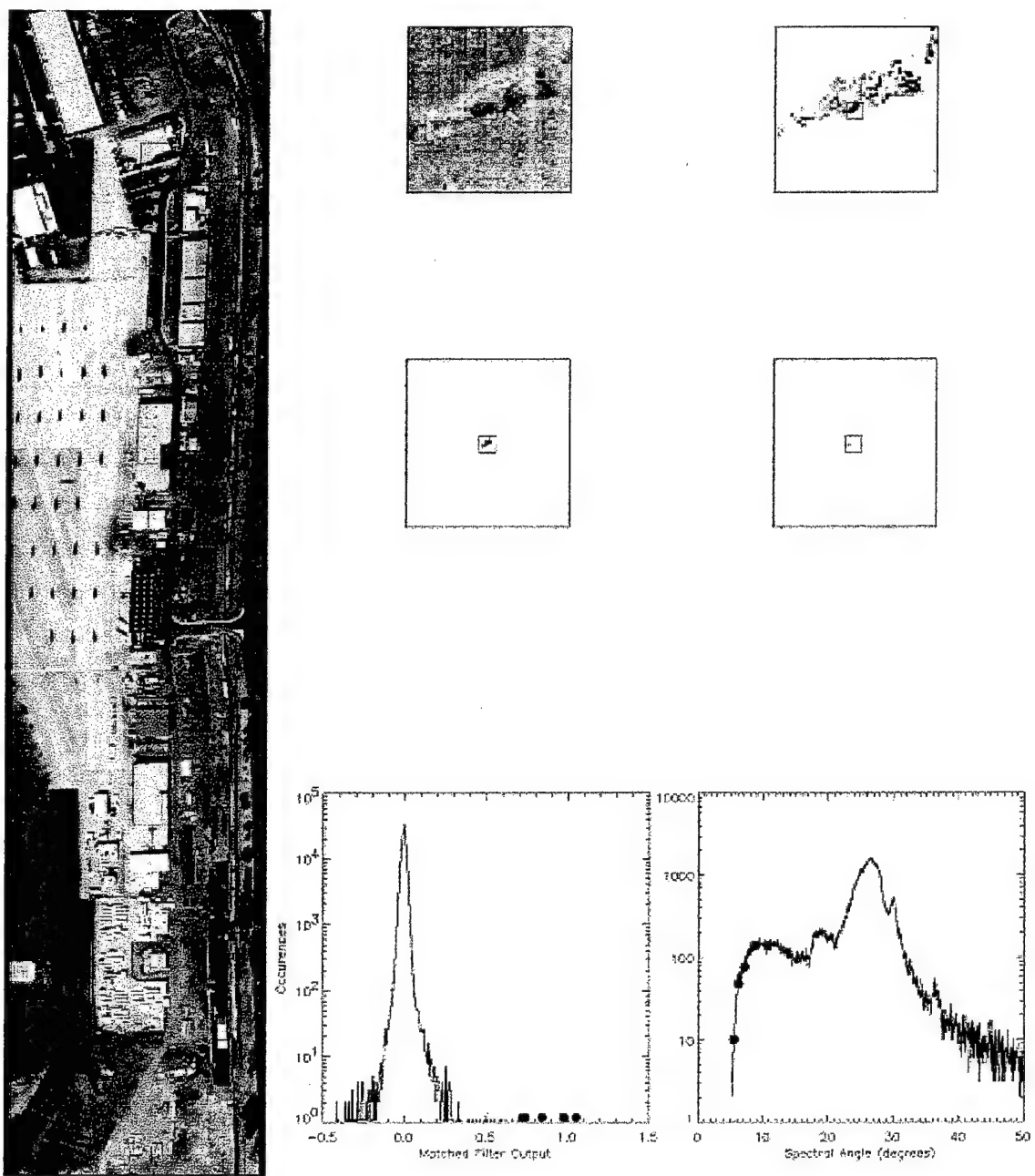
Figure 5.9: Left: HYDICE image of the airfield at Camp Pendleton, Run 45 at 5,000 feet. Top Row: Matched Filter and Spectral Angle Mapper results respectively, for target F12a in the outlined area. Second Row: Result images enhanced to highlight target pixels. Bottom Right: MF and SAM histograms with values for the F12a target pixels marked with red dots. The target pixel values detected by the MF algorithm are greater than ten standard deviations from the mean.

C. DISCLOSURE OF TARGET LOCATIONS (DETECTION OF F4C, AND F13B)

Once the exact locations of the targets were known, the images were enhanced using a linear stretch to highlight the targets. Pixel spectra were then visually analyzed in the given target areas to see if the targets could be positively located. If the target was located using these methods then the algorithm was listed with an asterisk (*) in Table 5.1. F4c and F13b were located using this technique with an example of the results obtained for F4c shown in Figure 5.10.

1. Post Disclosure looks using MF and SAM

The MF results showing F4c with false targets are shown in Figure 5.10. F4c was a 1-meter by 1-meter square and placed very close to the edge of a building. This target was not imaged at 5,000 feet, but was imaged by Run 31 at 10,000 feet. The expected ground pixel size from 10,000 feet is greater than $1m^2$, which makes this a subpixel target. Also, because of the building edge and many other close reflective objects the adjacency effects lead to a difficult detection.

After enhancing the MF results to detect this target the results show many false targets which can be seen in Figure 5.10. These false targets would not necessarily inhibit detection if the visual comparison of the spectra for the target pixel was easily matched to the ground truth target spectra. The chart at the bottom right hand side of the figure shows the comparison of the target pixel spectra (blue) to the MTL Ground Truth data (black) for the F4c material. At first glance it is not easily seen that the two spectra are the same. The third data series (red) is simply the ground truth data values multiplied by a factor of .3 to show that a gain value was the main difference between the two spectra. This error could have been incorrectly introduced during calibration or possibly because of a loss of radiance from target to sensor due to scattering and absorption.

Left: Matched Filter results for F4c from Run 31 at 10,000 feet. This result shows the F4c target pixel within the boxed area and several false targets in the rest of the scene. This MF image was linearly stretched to show only the results between 0.03 and 0.3 to ensure this target was highlighted.

Bottom Right: This chart shows the spectra plots of the target pixel (blue), F4c MTL truth (black), and F4c MTL truth multiplied by a factor of .3 (red). This shows the similarity between the target spectra and the truth spectra.

F4c Target
(1mX1m)

F4c Target Spectra (Run 31)

Legend
X:285/Y:1031
f4 MTL Truth
f4 MTL Truth *0.3

Reflectance (percent): 0, 0.2, 0.4, 0.6
Wavelength (micrometers): 0.4, 0.7, 1, 1.3, 1.6, 1.9, 2.2, 2.5, 2.8

**Figure 5.10: Target F4c Matched Filter Detect.**

61

The MF results for F13b following the enhancement to reveal the target resulted in a large number of false targets (approximately 100). For this reason the MF result is not shown. But, since the location of the target was known, it was easy to identify the pixel location by visually comparing the pixel spectra to the ground truth spectra. This comparison is shown in the graph in Figure 5.11.
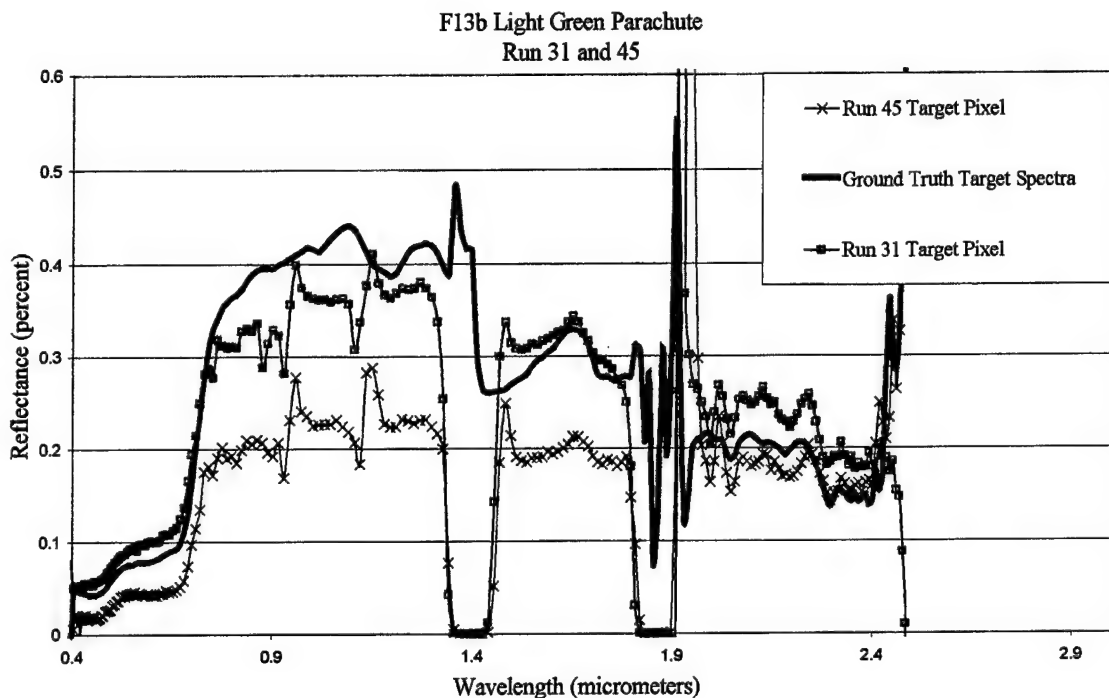
Figure 5.11: Reflectance vs. wavelength for target F13b from Littoral Radiance II, Camp Pendleton airfield Runs 31 (10,000 feet) and 45 (5,000 feet). Note the characteristic reflectance peak for this target in the 1.7 μm wavelength.

When looking at the comparison plots from target pixels to ground truth spectra in Figures 5.10 and 5.11 one important point should be noted. The scene spectra normally contained two or three pixels with very close matches to target spectra, but only the closest match was plotted. This is due to the reflectance from a given ground pixel containing only a portion of the target. So even though a target may be 1 meter by 1

meter it can contribute to four pixels at the sensor. A representation of this is shown in Figure 5.12.
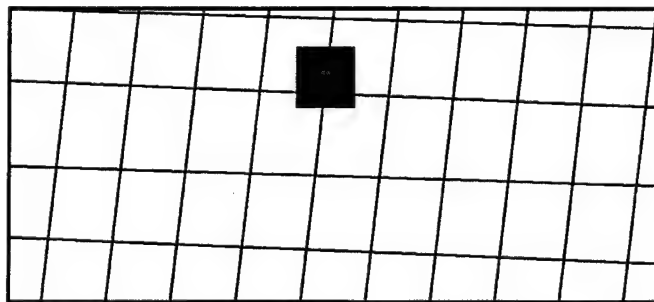
Figure 5.12: Pixel pattern at sensor due to altitude and direction of flight over the target. Although the target area is smaller than the resolved pixel area it still contributes to the reflectance of four separate pixels.

2. Post Disclosure looks using Constrained Energy Minimization (CEM) and Low Probability of Detection (LPD)

Following the second detailed look at the MF and SAM results other algorithms were used to improve the detection percentage. CEM and LPD were employed and the results were evaluated and compared to the results already obtained using the MF and SAM algorithms. The goal was to locate any of the previously undetected targets or to see if the results obtained using these algorithms were better than those of MF and SAM. Even with the target positions known the CEM and LPD algorithms did not contribute to any new target detects or significantly improve on the results already compiled.

3. Employing SAM and MF on spatial subsets

Run 45 was made up of five major frames of data which required the algorithms to compute spectral angles and matches for 1600 X 320 pixels with 210 bands each. Run 31 was only slightly smaller, four major frames, with 1280 X 320 pixels. Another attempt to locate undetected targets was completed by applying the SAM and MF algorithms to small areas within the image where the targets were known to be located.

To do this, the size of the data sets were reduced by selecting only subsets of the original image around the target of interest (50 X 240 pixels). This reduced the number of end members or eigenvectors requiring comparisons and was theorized to better segregate the final results allowing for easy detection of the target pixels. The targets selected for this analysis were P3 and P5. These targets were chosen because they were small (.6 X .6 meter) and they have easily distinguished spectra.

When analyzing the results using the spatial subsets, it was easy to see that both targets were located in the shaded area next to buildings in run 45. By visual inspection it could not be determined whether the targets were in the sun or in the shade in run 31. After completing these runs P3 was still not detected nor could the correct pixel be positively located during analysis. P5 was detected and positively located, but the results contained several false alarms and did not show an easily matched spectrum.

D.   SUMMARY

All three of the blind detects listed in Table 5.1 were from 3 X 3 meter targets. After the target locations were revealed a 2 X 2 meter and a 1 X 1 meter target were detected. The targets originally detected and geo-located were the larger panels for the given materials. The targets detected were located away from buildings and in areas where the signature spectra of the target was easily distinguishable from the surrounding environment. Results indicate that flights at 5,000 feet, as compared to 10,000 feet, had no significant benefits for algorithm detections. Also, these data show both algorithms, SAM and MF, contributing approximately equally to the detection process (similar success rates).

E.   DISCUSSION

The detection success rate was less than expected for the blind test conducted at the Camp Pendleton airfield. The larger targets were found in both images (run 31 and run 45). The smaller targets were not detected in either image. There were few observed differences between the results of run 31 and run 45, which were flown at 10,000 feet and

5,000 feet respectively. Because of the similar results between the two different altitudes, it was noted that the target size was not the governing factor determining detection. The most likely factor that allowed the smaller targets to go undetected was the target placement. The exact locations and relative environments are not known for all targets. However, the overhead photograph labeled with the approximate locations of the targets, combined with the field photographs of individual targets presented in chapter two, show that the placement of these smaller targets would be a significant factor for non-detection. Targets P3 and P5 were shaded by buildings in run 45 and targets F3c and F12c were placed in areas where the surrounding environment's spectral signature closely matched the target signatures. The question still remains whether the smaller targets would have been detected by run 45 (2X the resolution of run 31), if the surroundings played less of a role in the probability of detection. This idea leads to the consideration of differences in the data caused by altitude variation. These differences are explored in the following chapter.

F.   BLIND TEST RECOMMENDATIONS

To extend the statistics for this blind test study the flight line 9 data could be analyzed. This line contained most of the targets in the 10,000 foot run, though not at the 5,000 foot run. Neither the run at 5,000 feet or 10,000 feet contained the calibration panels within the scene. Therefore, conversion to reflectance is more complex. Also, if it is known that the targets of interest include small targets (i.e. 1 X 1 meter or smaller) then the analyst should concentrate on sub-pixel detection methods. The analyst should also employ shade removal techniques for the targets located close to buildings.

VI.   ALTITUDE VARIATION EFFECTS

A.   INTRODUCTION

This chapter evaluates the results of the previously presented blind test study. Specifically, what are the differences between the data obtained from different altitudes? Although differences due to altitude do exist, is it possible to counter these effects in the data processing stage so that resolution is not the limiting factor in hyperspectral image technology? The data from both altitudes are compared using several techniques to determine the feasibility of using HYDICE for wide area target detection and classification.

The approaches used here to diagnose the variations due to altitude are:

- direct comparison of the spectra (dot product),
- comparison of manipulated spectra (principal component transforms),
- and, comparison of classified scenes (SAM, MF).

Note that the techniques used here are a subset of the techniques commonly used for change detection, as recently reviewed by Behrens (1998).

B.   REGISTRATION

Registration is defined as the alignment of one image to another image of the same area. Any two pixels at the same location in both images are then "in register" and represent two samples at the same point on the earth (Schowengerdt, pg.329). Employing comparison algorithms requires pixels from one image be linked to the same spatial pixel of the other image. Image to image registration was completed on run 31 (base image) and run 45 (warped image) for the Camp Pendleton airfield. Run 31 data were resampled for two times the resolution to approximate the ground pixel size of run 45. Ground control points (GCP's) were then selected using several different wavelength bands and principle component bands of both run 31 (640 X 2560 pixels) and run 45 (320 X 1600). Subpixel (fractional) coordinates were used from both images and a total of 156 GCP's

of 156 GCP's were chosen resulting in a rms registration error of less than 7.5. First degree polynomial warping and nearest neighbor resampling techniques were used for the resulting image of run 45. Figure 6.1 shows a portion of run 45 with its resulting warped image. The remainder of this chapter compares Run 31 (X2) to Run 45 (Warped).
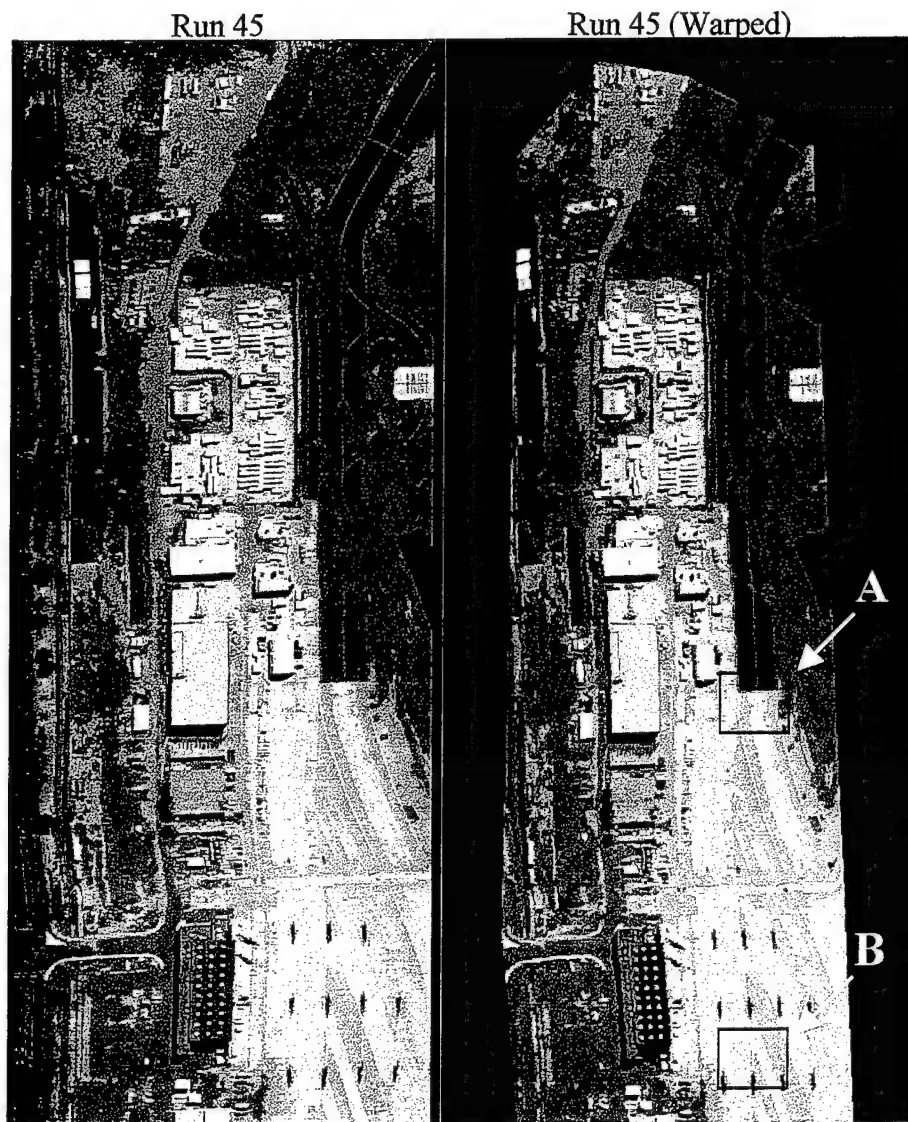

Figure 6.1: Eight-bit palette RGB images (bands 50-40-20) Left: Run 45 (lines 1 to 960) and Right: the resulting Run 45 (Warped) image (lines 1 to 960). The red boxed areas A and B are presented in Figure 6.11.

C.   REFLECTANCE CUBES COMPARED (RUN 45 (WARPED) TO RUN 31 (X2))

1.   Reflectance data scatter plot comparison

This section illustrates the comparison of the 165 band reflectance data from runs 31 (10,000 feet) and 45 (5,000). The simplest comparison between the two 165 band reflectance cubes can be seen in Figure 6.2. This figure is a scatter plot of reflectance values Run 45 (Warped) vs. Run 31 (X2) for each pixel and each wavelength band.
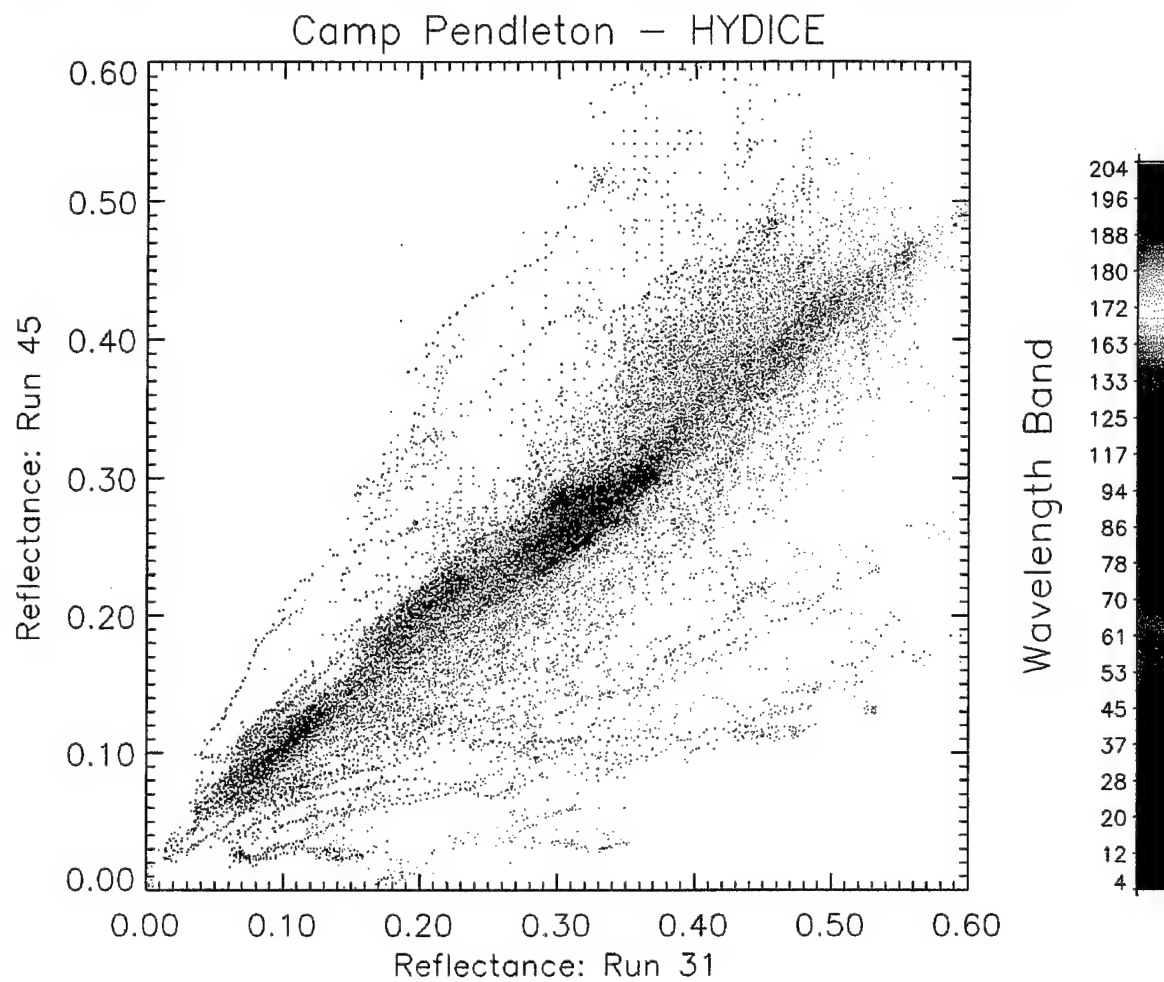
Figure 6.2: Scatter Plot for reflectance data from Run 45 (Warped) and Run 31 (X2). This data was obtained from the Camp Pendleton airfield as part of the Littoral Radiance II Collection in June 1997. The scale on the right shows the representative color for each wavelength band.

The reason for this plot was first, to determine if there were any trends in the differences between the two images and second, to find out if these differences existed for only certain wavelength bands. A perfect match between the data of Run 45 and Run 31 would be seen as a straight line with equal reflectance values for both runs. No major trends are seen, reflecting reasonable success in registration. This scatter plot did not show any wavelength band straying from the diagonal more than other bands. Also, the data generally follow the diagonal. These two results give the immediate impression that both runs, although flown at different altitudes, contain essentially the same data.

2.   Dot product comparison

Dot product calculations were performed to further investigate possible differences between the reflectance data. Figure 6.3 shows a partial scene of Run 45 overlaid on Run 31. The image was obtained by taking the dot product of the spectral vectors of Run 45 (Warped) pixels and Run 31 (X2) pixels. The figure displays the arccosine of the scalar product and follows the color scale to the right of the image. A Hue-Lightness-Saturation (HLS) coding is used, with the spectral angle encoded as hue, principal component one as intensity, and saturation set to 100%. The larger the spectral difference between Run 45 (Warped) and Run 31 (X2) the more red the display. Pixels with little or no difference are represented by colors close to blue.

Figure 6.3 shows some very distinct differences between the reflectance image cubes. Specifically, the difference areas (red) are seen -- "A" – on a large shed roof covered with a dark composition or tar material in the upper left portion of the image, -- "B" -- at the building edges, and -- "C" -- on the helicopter pad. A gray scale copy of Figure 6.3 is included as Figure 6.4 to highlight and discuss the areas of change (A, B, and C) between run 31 and run 45.
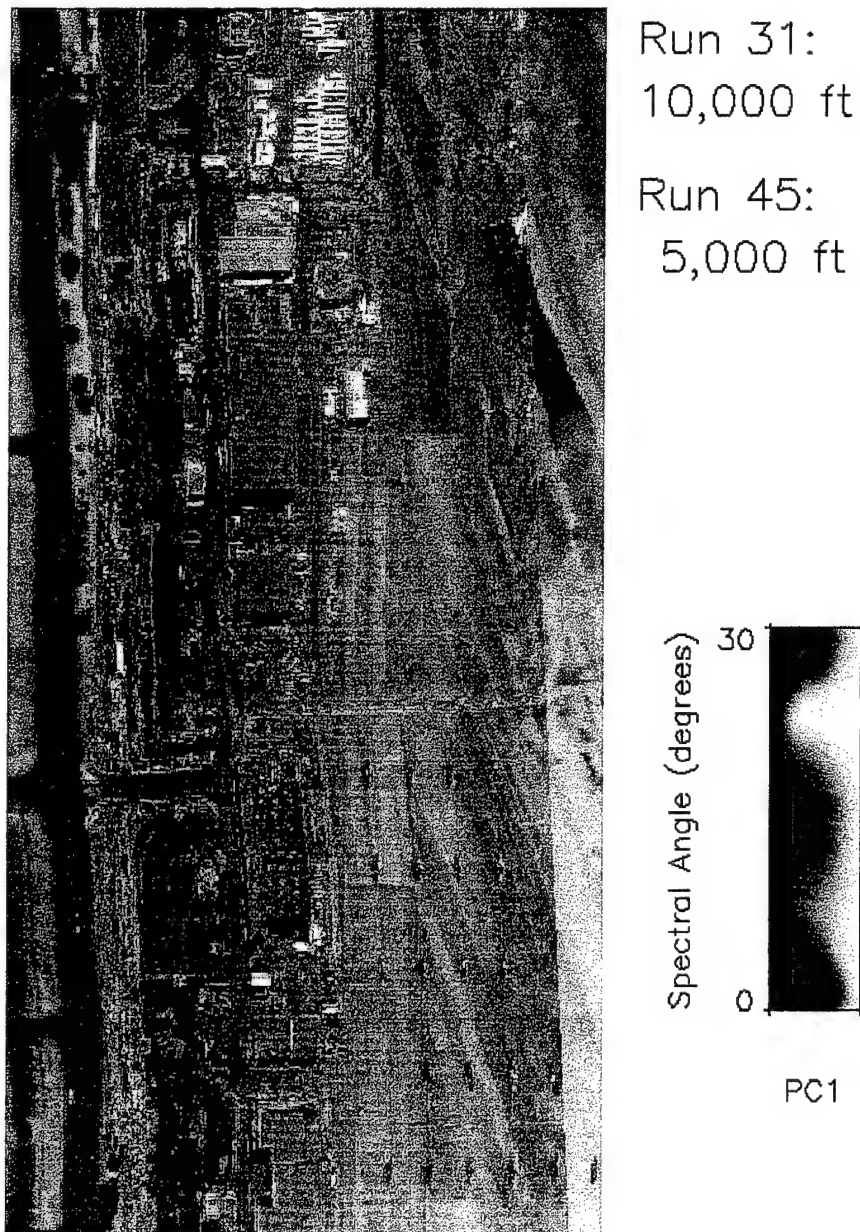
Figure 6.3: Camp Pendleton airfield from the Littoral Radiance II Collection in June 1997. Spectral Angle Comparison – HLS encoded. Resultant figure representing the spectral angle difference between Run 45 (Warped) and Run 31 (X2). Largest differences represented in red with the smaller differences represented by blue.
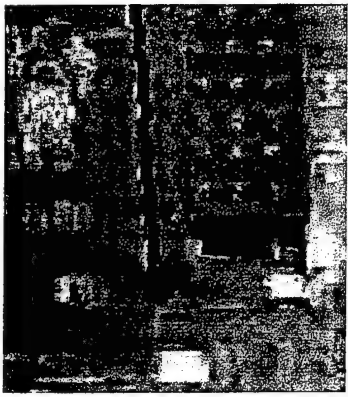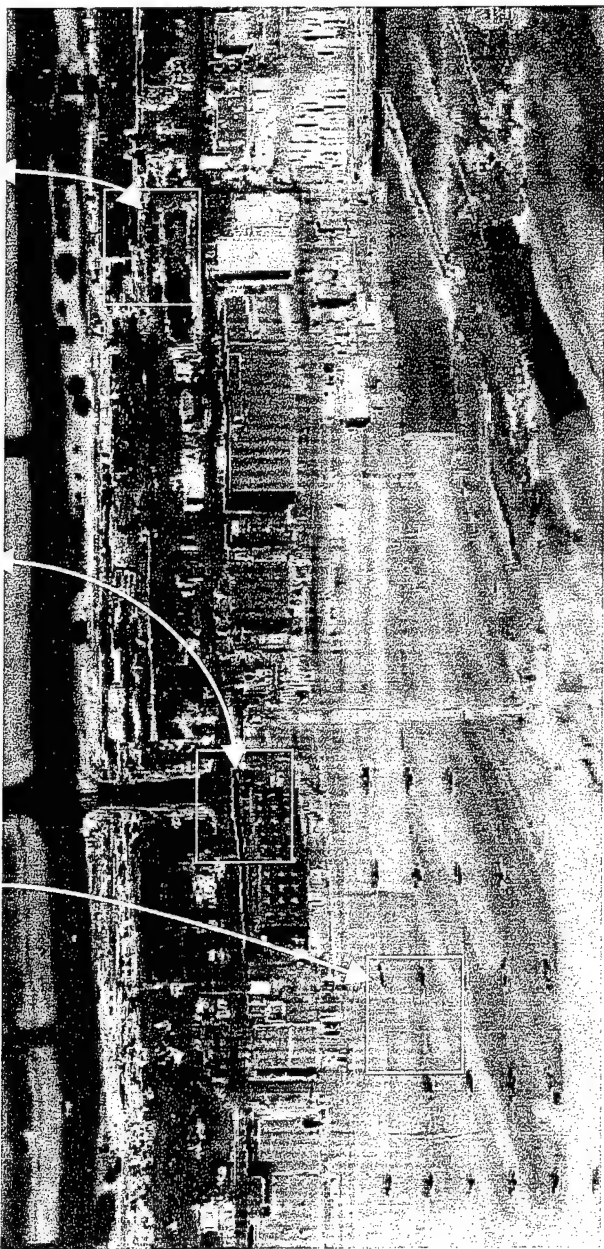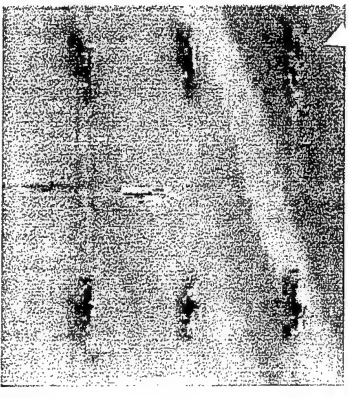
Figure 6.4: Reproduction of Figure 6.3 in eight bit gray scale with color pull-outs. This figure is included to highlight areas of change A, B, and C between Run 45 (Warped) and Run 31 (X2). Largest differences represented in red with the smaller differences represented by blue.

The first significant difference is highlighted in box A from the upper left portion of the figure. Throughout the scene relatively large differences represented by red, green and yellow represent paved or tarred areas. The most probable cause of these differences is noise, however, there might be some illumination effect - angular dependence. The relatively flat signatures and low reflectance of the pavement or tar lends itself to increased noise showing up in the data. This holds true on paved roads and for buildings in the scene that appear to have black tar or dark composition roofs. The area in the upper left portion of the image has two factors contributing to large difference between images. The difference area is a shed structure with a dark roof and located in the scene where both flights had turbulence causing the structure to look curved or bent rather than straight. The noise due to low reflectance and the misregistration due to "squiggly" data are the causes for the large spectral differences in this area.

The reflectance differences highlighted in B near the buildings were determined to be due to changes in shadows from one run to the next and due to some registration errors between the two images. With the number of registration points and the good image data used for registration most difference can be attributed to the shade.

Several helicopters are shown on the concrete parking pad in box C highlighting distinct differences between the images. Because the largest differences show up more toward the center of these helicopters, rather than the edge, it seems reasonable to attribute these differences to sun reflection angle and not registration errors. The helicopter parked horizontally in the image beneath the fourth row of helicopters was in Run 45, but not in Run 31. This was the most prominent difference between the two images and is recorded as red because the change exceeded the thirty-degree threshold for the figure.

D.   PRINCIPLE COMPONENT TRANSFORMS COMPARED

To more efficiently analyze the two data sets a Principal Component Transformation of axes was completed on the images to reduce the data to a manageable

size without losing important information. A principal component transformation is done by building a correlation or covariance matrix from two data sets with the same number of bands. For two images with P wavelength bands the cross covariance for p to q is,

$$C_{pq} = \left\langle \left(m_p - \left\langle m_p \right\rangle\right)\left(m_q - \left\langle m_q \right\rangle\right)\right\rangle,$$

(6.1)

with the complete matrix being,

$$C = \begin{bmatrix} C_{aa} & C_{ab} & \cdots & C_{ap} \\ C_{ab} & \cdots & \cdots & C_{bp} \\ \vdots & \vdots & \ddots & \vdots \\ C_{ap} & C_{bp} & \cdots & C_{pp} \end{bmatrix}.$$

(6.2)

The covariance matrix is then diagonalized resulting in the principle components (variances) only,

$$C' = \begin{bmatrix} C'_{aa} & 0 & \cdots & 0 \\ 0 & C'_{bb} & \cdots & 0 \\ \vdots & \vdots & \ddots & \vdots \\ 0 & 0 & \cdots & C_{pp} \end{bmatrix}.$$

(6.3)

The eigenvectors of this new matrix form the new coordinate system where all features are uncorrelated (Jahne, pg. 516). The transform has not yet reduced the dimensionality of the data. This is done after evaluating what kind of data points belong to individual Principle Component (PC) bands. Normally the first several bands can be analyzed to evaluate whether they contain the most relevant information. The first three PC bands of the Camp Pendleton data were used for several analyses in this thesis, including, GCP selection and general classification of the area. Later, following the registration of run 45 to Run 45 (Warped) and the doubling of resolution of run 31 to Run 31 (X2), the first ten PC bands were selected for further data analysis.

The method used here compares the images by displaying the first Principle Component (PC1) band from each image. These images are overlaid in Figure 6.5 with values of PC1-Run 45 represented by varying shades of yellow and values from PC1-Run 31 represented by varying shades of blue. Areas of difference show up in blue or yellow while perfect pixel matches between the images show up in varying shades of gray.
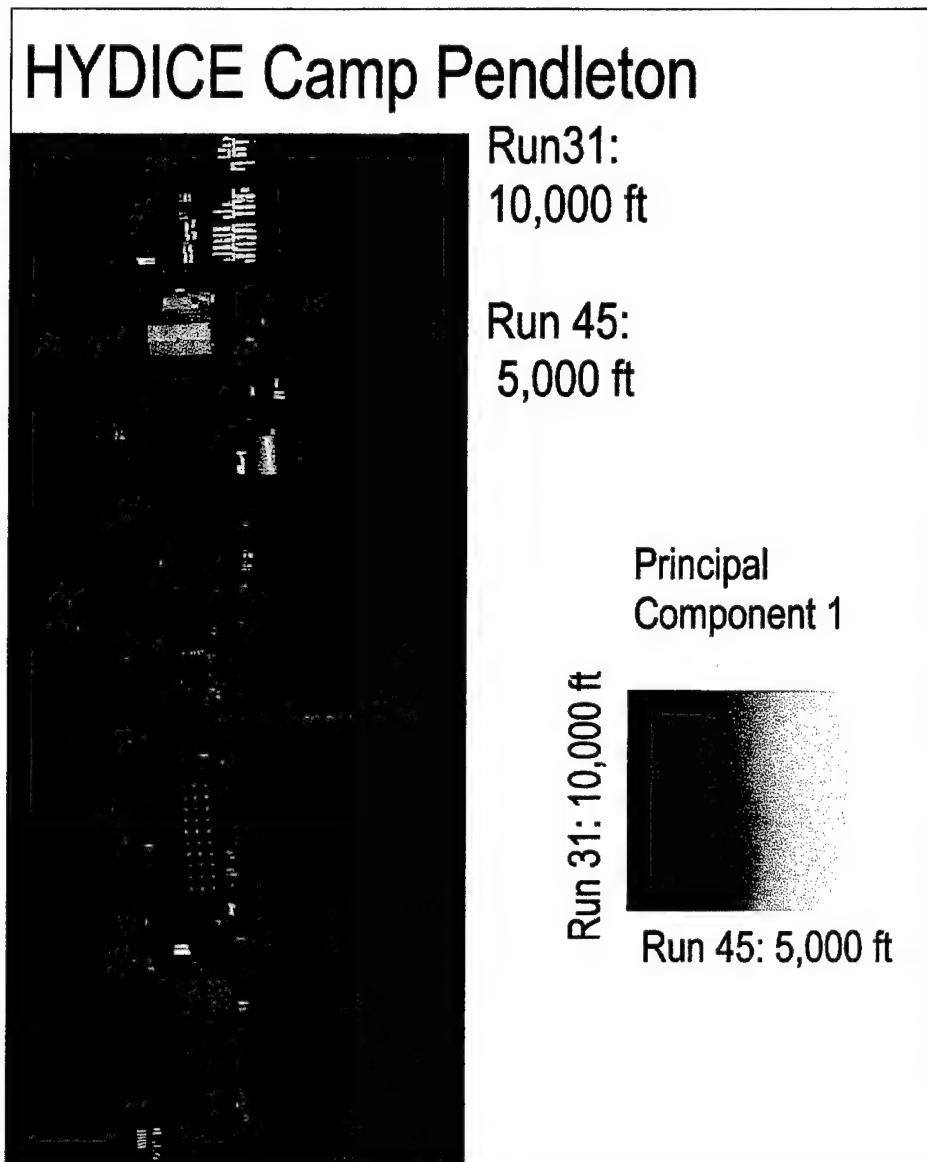

Figure 6.5: Principal Component band 1 (PC1), from Run 45 (Warped) overlaid on PC1-Run 31 (X2). Data obtained from HYDICE flights over Camp Pendleton as part of the Littoral Radiance II collect in June of 1997.

The finer differences between the two runs did not show up in Figure 6.5. The only significant result obtained from this technique was the change caused by the helicopter (beneath the fourth row of helicopters, horizontally parked) being present in Run 45, but not in Run 31. It appears as a relatively bright blue.

E.   CLASSIFICATION MAPS COMPARED

The three techniques employed were the Parallelepiped (PP) Classifier, Maximum Likelihood (ML) Classifier, and the Spectral Angle Mapper (SAM) Classifier. The PP and SAM classifiers were run on both the full images Run 45 (Warped) and Run 31 (X2) using 165/210 wavelength bands and on the ten bands of the PC images. The ML was run only on the ten PC bands. Classifiers were performed to produce classification maps to determine the best images for data comparison in altitude variation affects.

Classification began with an analysis of structure in the feature space of the PC images. The feature space is produced by the scatter plot of the two PC images. This scatter plot results in a data cloud (ten dimensions) that includes all pixels selected by the analyst from a given image. Pixel selection is completed to obtain a representative sample of the different types of objects and geography in the scene. Figure 6.6 shows the data cloud from the Run 45 (Warped) PC bands. Eight end members were selected for supervised classifications of the data.
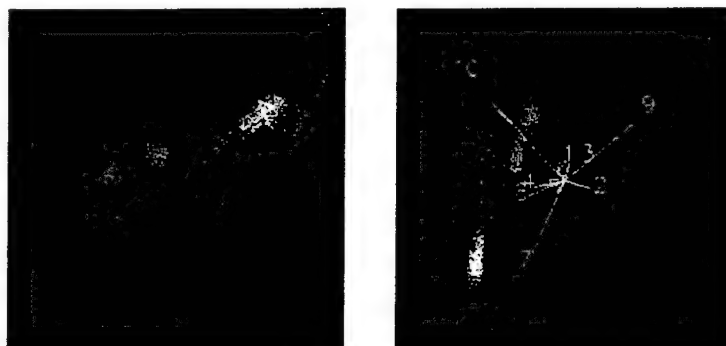
Figure 6.6: Data cloud resulting from the selected regions of interest in Run 45 (Warped) PC bands 1-10. The two pictures show different rotational views of the data cloud with the end members color coded for supervised classifications. The right picture includes the PC axes that resulted from the PC transformations.

The colors selected for the end members of Run 45 were the same as those selected for Run 31. Table 6.1 defines the set of colors consistently used for all images discussed in the following sections. The classification techniques differ only by the method used to associate classes to clusters in the data cloud. Complete classification maps for each technique are included in the Appendix. Small subsections are presented below for discussion.

Table 6.1: End member color selection for all images discussed in this chapter.

Color		Region Selected
Red	■	Roof Top
Green	■	Vegetation
Blue	■	Dirt Parking Lot
Coral	■	Concrete 1
Maroon	■	Concrete 2
Cyan	■	Concrete 3
Magenta	■	Paving 1
Yellow		Paving 2

1.   Parallelepiped Classification

Parallelepiped classification uses decision boundaries to form an eight dimensional parallelepiped in the feature space (ENVI, pg. 373). These boundaries are defined by a number of standard deviations from the mean value for that dimension. A pixel is evaluated and determined to fall within one parallelepiped, several parallelepipeds, or outside of all parallelepipeds. If the value from a pixel is inside several parallelepipeds then the value is associated with the last class matched. This classification was completed using criteria of both three and five standard deviations from the mean. This classification method was applied both in "reflectance" space, and in "principal component" space. A sample of the Parallelepiped results for PC bands one through ten for Run 45 (Warped) and Run 31 (X2) is shown in Figure 6.7.
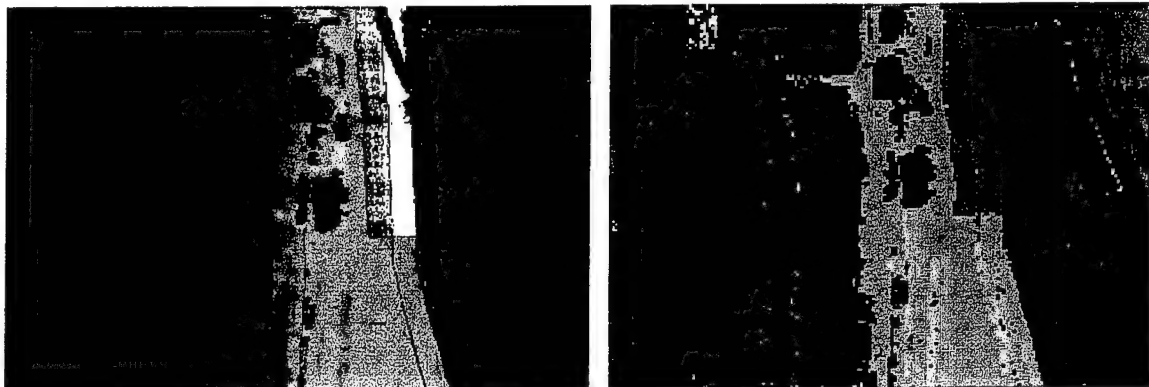
Figure 6.7: **Parallelepiped Classification, 5 standard deviations from the mean, results from PC bands 1-10. Left: Run 45 (Warped), samples 0 through 420, lines 450 to 700. Right: Run 31 (X2), samples 0 through 400, lines 300 to 550.**

2. Maximum Likelihood Classification

The second technique used was a maximum likelihood classifier. Each cluster is modeled as a statistical probability density function (Jahne, pg. 519). This results in eight normal distribution functions for the end members selected. The probability of a feature vector belonging to any one of these clusters is calculated and the pixel is associated using the highest probability. A sample of the Maximum Likelihood results for PC bands one through ten for Run 45 (Warped) and Run 31 (X2) is shown in figure 6.8. This technique did not run successfully over the complete 165 band data cube.

Figure 6.8: **Maximum Likelihood results from PC bands 1-10. Left: Run 45 (Warped), samples 0 through 420, lines 450 to 700. Right: Run 31 (X2), samples 0 through 640, lines 300 to 550.**

3. Spectral Angle Mapper Classification

The SAM classification defines end member spectral vectors in a space equal to the number of bands in the image. The algorithm then determines the spectral similarity between two spectra by calculating the angle between the spectra (ENVI pg. 377). The spectral angle in radians is expressed,

$$\cos^{-1}\left(\frac{\mathbf{x} \bullet \mathbf{u}}{\|\mathbf{x}\|\|\mathbf{u}\|}\right) = \cos^{-1}\left(\frac{\sum_{i=1}^{l} x_i u_i}{\sqrt{\sum_{i=1}^{l} x_i^2}\sqrt{\sum_{i=1}^{l} u_i^2}}\right). \tag{6.4}$$

Where $\mathbf{x}$ is the observed pixel vector and $\mathbf{u}$ is the reference end member vector. The dot product of $\mathbf{x}$ and $\mathbf{u}$ are divided by the product of their Euclidean norms to cancel out the amplitude difference of the two vectors (Behrens pg. 15).

Figure 6.9 is the graphical illustration of the spectral angle between the end member vector (Reference) and the pixel's spectral vector (Observed) for two dimensions.
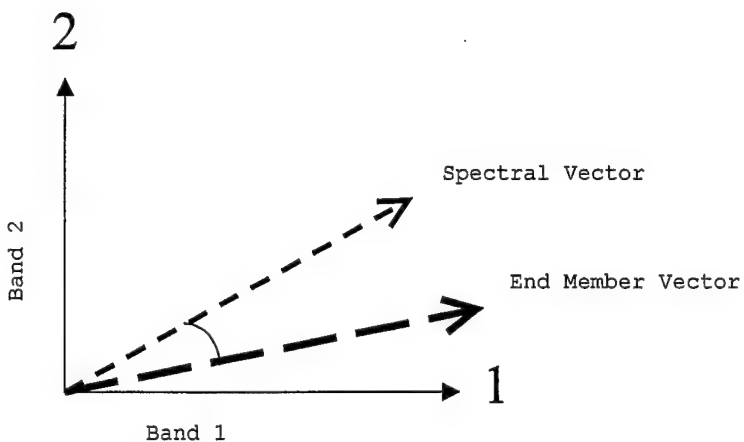
Figure 6.9: A graphical illustration of the spectral angle for a two-band example (after Collins, 1996).

This classification was performed on the 165 bands from Run 45 (Warped) and Run 31 (X2) untransformed images and their respective PC images. A sample of the Spectral Angle Mapper classification results for the image cube is shown in Figure 6.10.
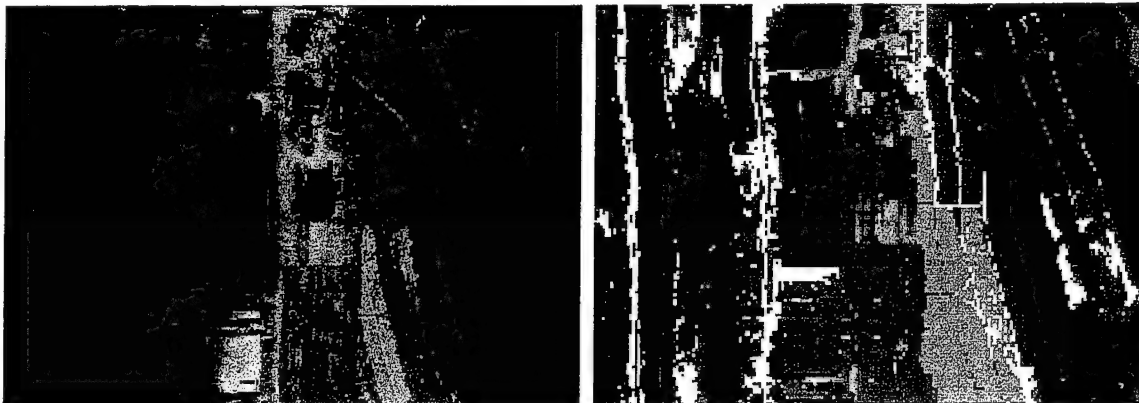

Figure 6.10: Spectral Angle Mapper classification results from the 165 band image cubes. Left: Run 45 (Warped), samples 0 through 420, lines 450 to 700. Right: Run 31 (X2), samples 0 through 400, lines 300 to 550.

4. Classification map selection for further analysis

A modest subset of the classified maps from Run 45 (Warped) has been selected to illustrate the character of the differences observed. Individual pixel spectra and data clouds were evaluated from these subsets.

a) Parallelepiped Selection

The areas of comparison for the PP classification maps of Run 45 (Warped) are shown in Figure 6.11. The upper row of images show the PP results from box A of Figure 6.1. The lower row shows PP results from box B of Figure 6.1. These subsets show the PP classes from the warped cube and from the PC transforms of the warped cube at three standard deviations and five standard deviations respectively.
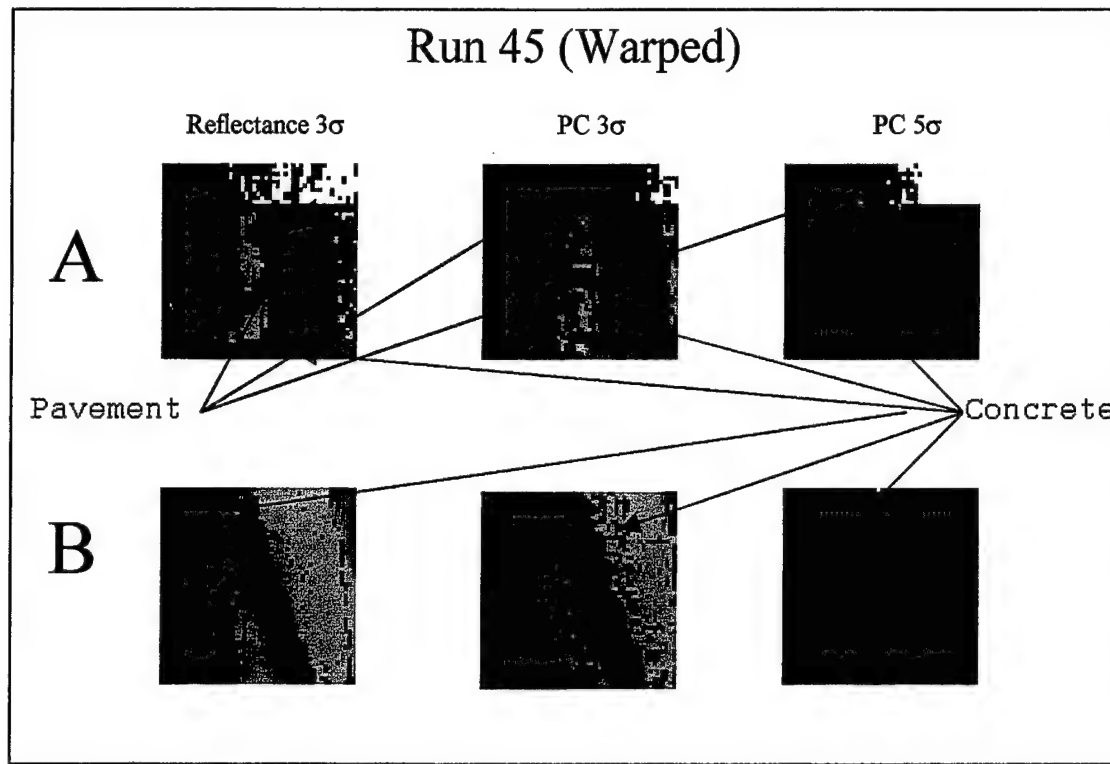
Figure 6.11: Left: Run 45 (Warped), PP class map, three standard deviations from the mean. Center: Run 45 (Warped PC transform bands 1-10), three standard deviations from the mean. Right: Run 45 (Warped PC transform bands 1-10), five standard deviations from the mean. The top row correlates to the upper-boxed area "A" shown in Figure 6.1 and the bottom row correlates to the lower boxed area "B".

Figure 6.11 shows small subsets from the Run 45 scene as indicated in Figure 6.1. There are differences in the classification results, but it should be noted that these represent small differences in concrete or pavement - apparently differing by age or other factors. These small images were evaluated to determine which classification technique would be best used for change detection.

The right most images top and bottom, were disregarded for further comparison because of the relatively low sensitivity to change detection between the types of concrete or paved features. The PP class maps of the 165-band image cube (first column) and the ten-band PC image cube (second column) contains sensitive and correct classifications. The best representation of the actual data is in the left most images.

These images appear to correctly classify the pixels and retain needed detail for later analysis.

b) *Maximum Likelihood Selection*

Maximum Likelihood classification was run only on the ten band PC transformed images. These images contribute high levels of detail to the vegetation and dirt covered areas and will be looked at in detail in the next section.

c) *Spectral Angle Mapper Selection*

As in the case of the parallelepiped classification selection, the 165-band image cube contains far more correctly classified pixels than the PC image classification.

The maps selected were the Parallelepiped classifications of the 165-band image cubes, the Maximum Likelihood classifications of the ten PC band cubes, and the Spectral Angle Mapper classifications of the 165-band image cubes. These maps were chosen for further analysis because of unique advantages offered from each classification technique. The Parallelepiped maps show fine differences in concrete and pavement that could be due to age, compactness, or type. The Maximum Likelihood results show excellent classification of the vegetation and parking areas that did not show up so well in other class maps. And finally, the Spectral Angle Mapper results show some subtle differences between run 31 and run 45 images. Full view images of these classification maps for runs 45 and 31 are included in the Appendix.

5. Classification Map Differencing

The classification maps from Run 45 (Warped) and Run 31 (X2) were compared by creating an image that represents the algebraic difference between the two runs. Each map contained eight bands of data representing the classes chosen to represent the scene. Run 31 (X2) was subtracted from Run 45 (Warped) for each classification technique.

ML, SAM, and PP differencing all showed expected results that had already been seen in the above 165 band comparisons, with no significant differences between images due to altitude changes for the sensor. All differences appeared to be due to registration

error, noise, and actual scene changes from one run to the next. However, to find all changes from one scene to the next all results needed to be evaluated. No single result held all of the differences between the images.

The ML result contained valuable information on the registration error between the images. In Figure 6.12 below, the white outline of the vegetation area in the upper right hand corner is a direct result of registration error in that region. This image shows the vegetation classification differences between Run 45 (Warped) and Run 31 (X2). The white represents the area classed as vegetation in Run 45 (Warped), but not in Run 31 (X2). The light gray areas are those that were classified as the same material in both images and resulted in zero change between the two images. The dark gray areas were classified as vegetation in Run 31 (X2), but not in Run 45 (Warped). The black is the border region between images that was not differenced.
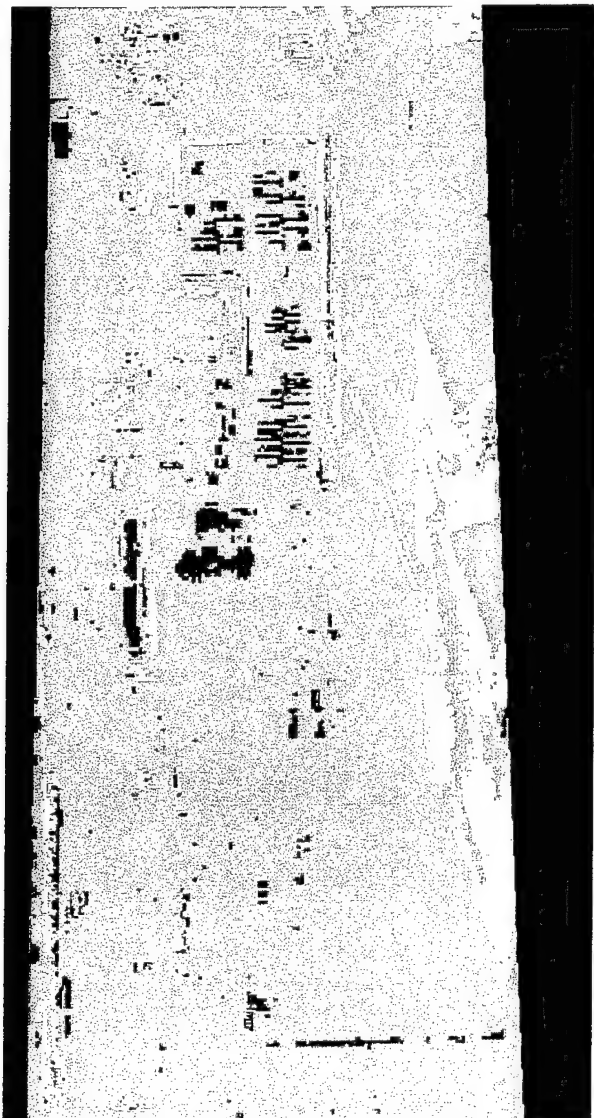
Figure 6.12: Maximum Likelihood classification differences between Run 45 (Warped) and Run 31 (X2) from the Camp Pendleton airfield, Littoral Radiance II. White areas represent those classified as vegetation in Run 45, but not in Run 31. Dark gray represents areas classified as vegetation in Run 31, but not in Run 45. The lighter gray represents areas of no difference in classification between the images.

Figure 6.13 was created using the same process as Figure 6.12 except that it represents the differences for the SAM vegetation classifications. This figure again

shows the differences for the vegetation band, but the registration errors are not great in this result as in the ML result.
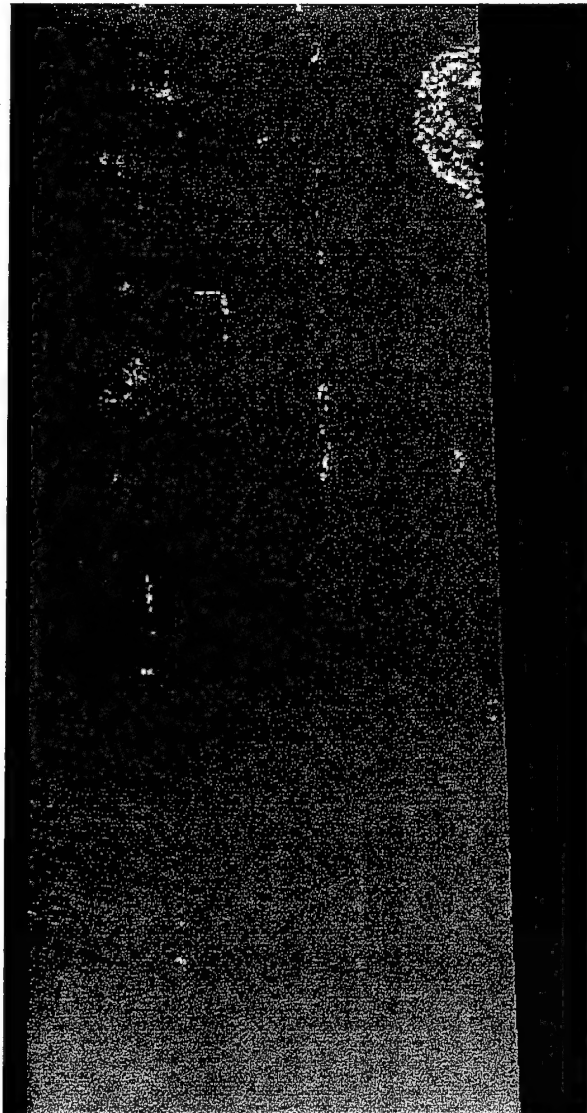
Figure 6.13: Spectral Angle Mapper classification differences between Run 45 (Warped) and Run 31 (X2) from the Camp Pendleton airfield, Littoral Radiance II. White areas represent those classified as vegetation in Run 45, but not in Run 31. Dark gray represents areas classified as vegetation in Run 31, but not in Run 45. The lighter gray represents areas of no difference in classification between the images.
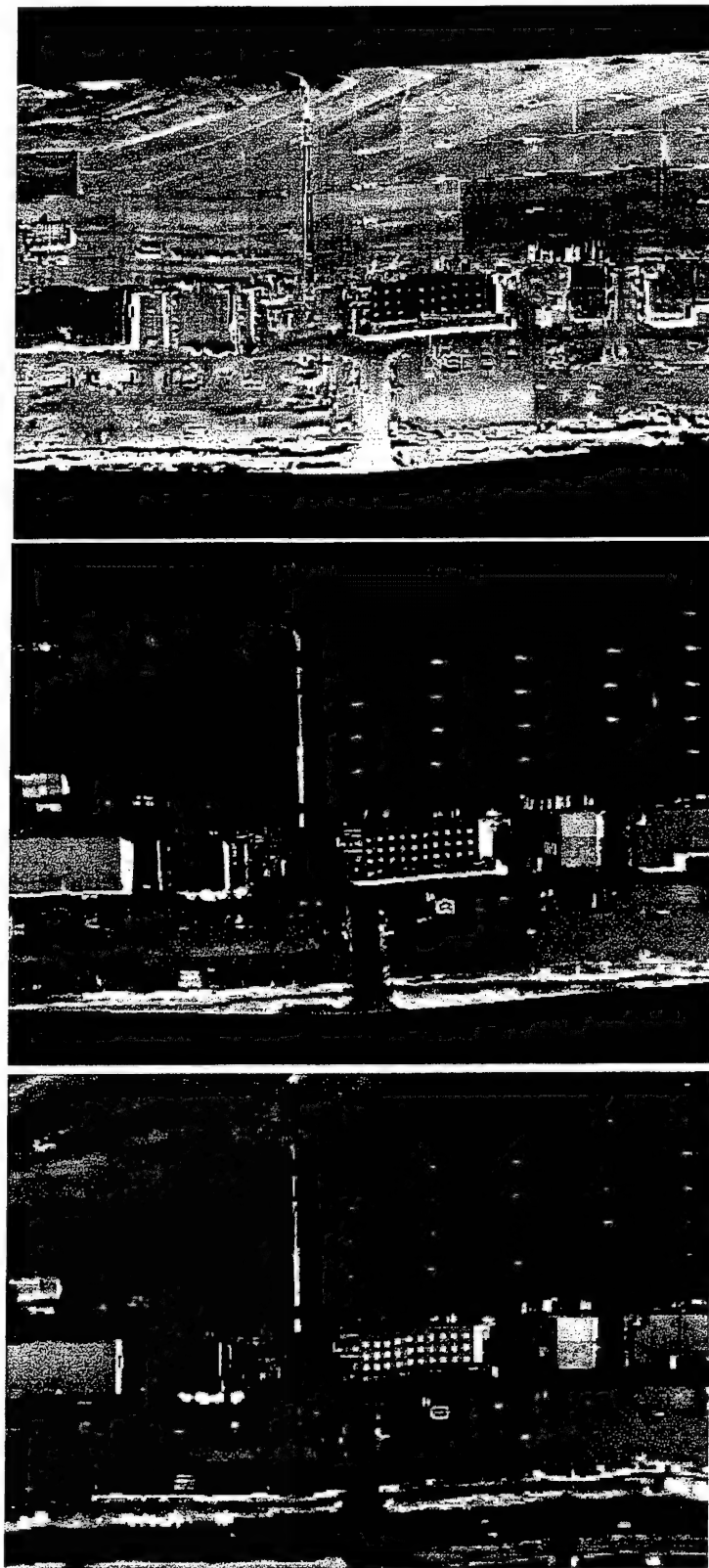
Figure 6.14: Left: Spectral angle classification in radians for band 6 (Concrete 1), Run 31. Center: Spectral angle classification in radians for band 6 (Concrete 1), Run 45. Right: Spectral angle difference, in radians, for band 6, between run 31 and run 45. White corresponds to significant changes from one image to the next. Black corresponds to zero change.

A different comparison approach was attempted for a more global view of change as revealed by the SAM classifier, in spectral angle, rather than binary class. These results are shown in Figures 6.14 and 6.15. Figure 6.14 shows the SAM output for the two runs, and the spectral angle difference for a single band (band 6, concrete) in radians. One of the more obvious changes from one image to the next is the helicopter in the lower right hand corner. Note however that the spectral differences for the stationary helicopters are as great (greater than 60 degrees).
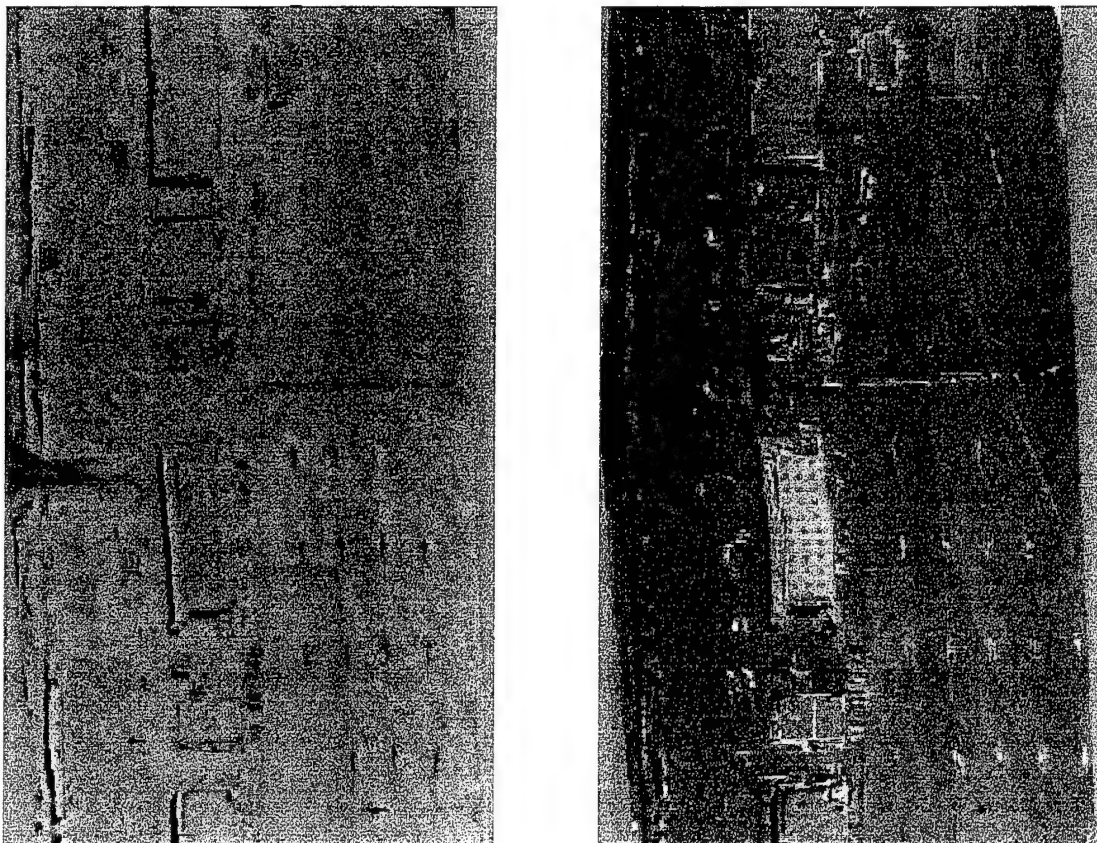
Figure 6.15: Spectral Angle Mapper (SAM) classification differences between Run 45 (Warped) and Run 31 (X2) from the Camp Pendleton airfield, Littoral Radiance II. Left: Bands 6, 7, and 8 from SAM differencing the bands are represented in red, green, and blue respectively. Right: Bands 1, 2, and 3 from SAM differencing the bands are represented in red, green, and blue respectively.

Results from six bands are combined in two panels in Figure 6.15. The left hand image of Figure 6.15 shows the differences between classification bands (6, 7, and 8), which are the three concrete classes. That is, red is encoded with the changes in class 6, in radians, green is encoded with changes in class 7, and blue is encoded with the changes in class 8. In a similar way, the difference in spectral angle for bands 1, 2, and 3 are encoded in RGB on the right hand side of Figure 6.14. Band 1 is the roof material class, band 2 is the vegetation class and band 3 is the dirt parking class.

Parallelepiped (PP) differencing was performed, but the images were not included in this chapter. The PP results did not reveal any further change information between images.

F.   SUMMARY

Variation between the data from Run 31 and Run 45 were analyzed. Registration was done from scene to scene, with errors of about one pixel. Following registration, the reflectance bands from each flight were compared using various methods including a histogram and a color encoded dot product image. Next, the first principal components were compared to search for major changes. Finally, class maps were created using three different methods to check how the classification techniques would perform from each altitude and how the results would differ. All comparisons were evaluated and lead to the conclusion that there were not any major differences in the results from data taken at the two altitudes. A detailed summary and conclusions are included in the next chapter.

VII. SUMMARY AND CONCLUSIONS

All data analyzed in the preceding chapters were collected during the Littoral Radiance II experiment conducted in June of 1997. A subset of the Littoral Radiance II experiment included deploying ground targets in unknown locations for the sole purpose of performing a "blind test". The thirteen targets consisted of standard HYMSMO fabrics and painted panels that were placed in various locations throughout the Camp Pendleton airfield and support facilities.

A CV-580 aircraft (picture included in the Appendix) carrying the HYDICE sensor flew several flight lines over the airfield collecting images in the visible and infrared (.4 μm to 2.5 μm). All flight lines over the airfield area were analyzed in an attempt to detect and geo-locate all of the deployed targets. This "blind test" was the first experiment of its kind sponsored by HYMSMO.

Following sensor calibrations completed while on the aircraft and radiance calibrations completed at SITAC in Fairfax, Virginia, all data was converted to reflectance by the Empirical Line Method. The conversion from radiance to apparent reflectance proved very successful due to the placement of calibration panels within the scenes and extensive ground truth information supplied by MTL Systems, Inc. The two primary algorithms employed to detect the targets within the airfield images were the Matched Filter and Spectral Angle Mapper routines in ENVI. Both algorithms performed equally well on all targets.

The above analysis showed that there were little or no differences in the results obtained from either of the two altitudes (Run 45 at 5,000 feet and Run 31 at 10,000 feet). The governing factor affecting the detection success rate for the targets was the level of difficulty in placement of the targets in relation to their immediate surroundings.

After completing the blind test the images from the most pertinent flight lines were again analyzed. Techniques were used to determine the differences between images

obtained from different altitudes. The goal was to identify those effects due solely to different flight altitudes of the sensor. Run 45 (Figure 5.7), an image obtained from 5,000 feet, was registered to a base image from run 31 (Figure 5.1), an image obtained from 10,000 feet. The resulting two images, Run 45 (Warped) and Run 31 (X2), were then used for altitude comparisons.

Spectral angle comparisons were performed on the reflectance data of each image. This consisted of taking the dot product between each wavelength band for each pixel of Run 45 (Warped) and the associated pixel from Run 31 (X2). The spectral differences were easily seen in the resulting image in Chapter 6 by using the color scale provided with the image.

A comparison between the first principal component bands of Run 45 (Warped) and Run 31 (X2) was performed by overlaying one on the other. The principle component band from Run 45 (Warped) was represented by blue and the band from Run 31 (X2) was represented by yellow. This technique was successful in detecting major changes. This result was the first indication that a helicopter was present in Run 45 (Warped), but not in Run 31 (X2).

Classification maps were created with Spectral Angle Mapper, Parallelepiped, and Maximum Likelihood for further comparison between altitudes. Each classification was supervised and consisted of eight end members that best represented the image environments. Out of the twelve image maps created, six were selected for post processing. The post processing performed consisted of differencing the image maps. The respective map from Run 31 (X2) was subtracted from Run 45 (Warped). The results showed differences in the images due to shade, vehicle movement (helicopter), and registration errors. The only differences in classification were between types of concrete or types of pavement. Other areas that were difficult to segregate into distinct classes were areas of sparse grass and vegetation with a lot of soil showing through. These were classed as dirt parking areas or vegetation areas and were sometimes classed differently between the altitudes.

The results from Littoral Radiance II demonstrated an important capability of the HYDICE sensor and the standard algorithms for target detection and geo-location. However, further study is needed to develop techniques that will improve the detection success rate when targets are located in environments that mask, distort, or match the signature spectra of the target. The altitude effects on imagery obtained with HYDICE have proven to be small between the 5,000 and 10,000-foot levels. Different flight altitudes of the sensor did not adversely affect the results for target detection or scene classification. The equality of results between the two altitudes seen in these analyses is a positive conclusion that wide area applications using this sensor are feasible.

APPENDIX. EXTRA FIGURES

These figures were useful to the research completed, but were not specifically discussed in the body of this thesis.

**Figure 1: The HYDICE Sensor Platform, Convair 580, from http://rsd.www.nrl.navy.mil**

Run 45   **Run 31 (X2).**

Figure 2: Maximum Likelihood results from PC bands 1-10.
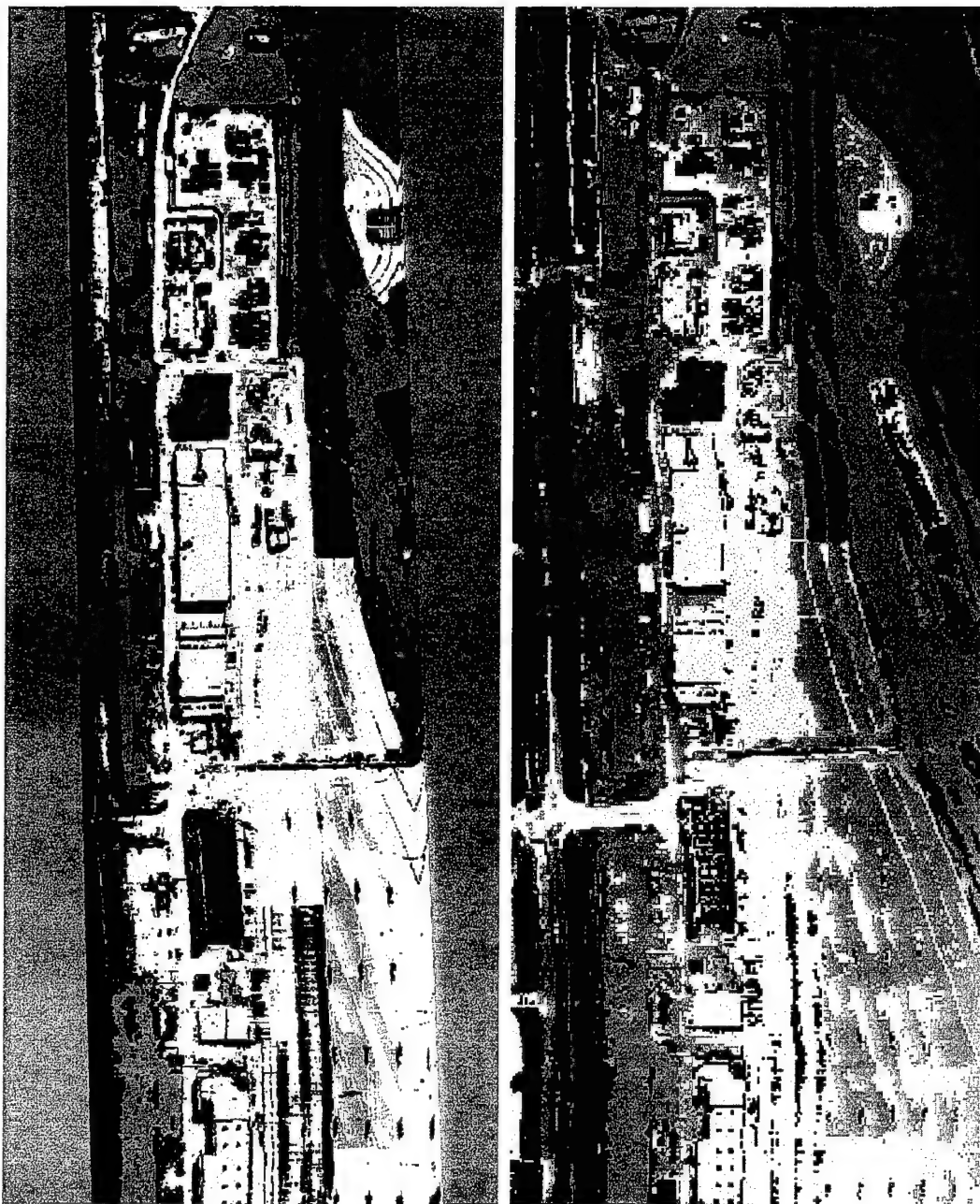
# Run 45   Run 31 (X2).

Figure 3: Spectral Angle Mapper results from 165 band cube.
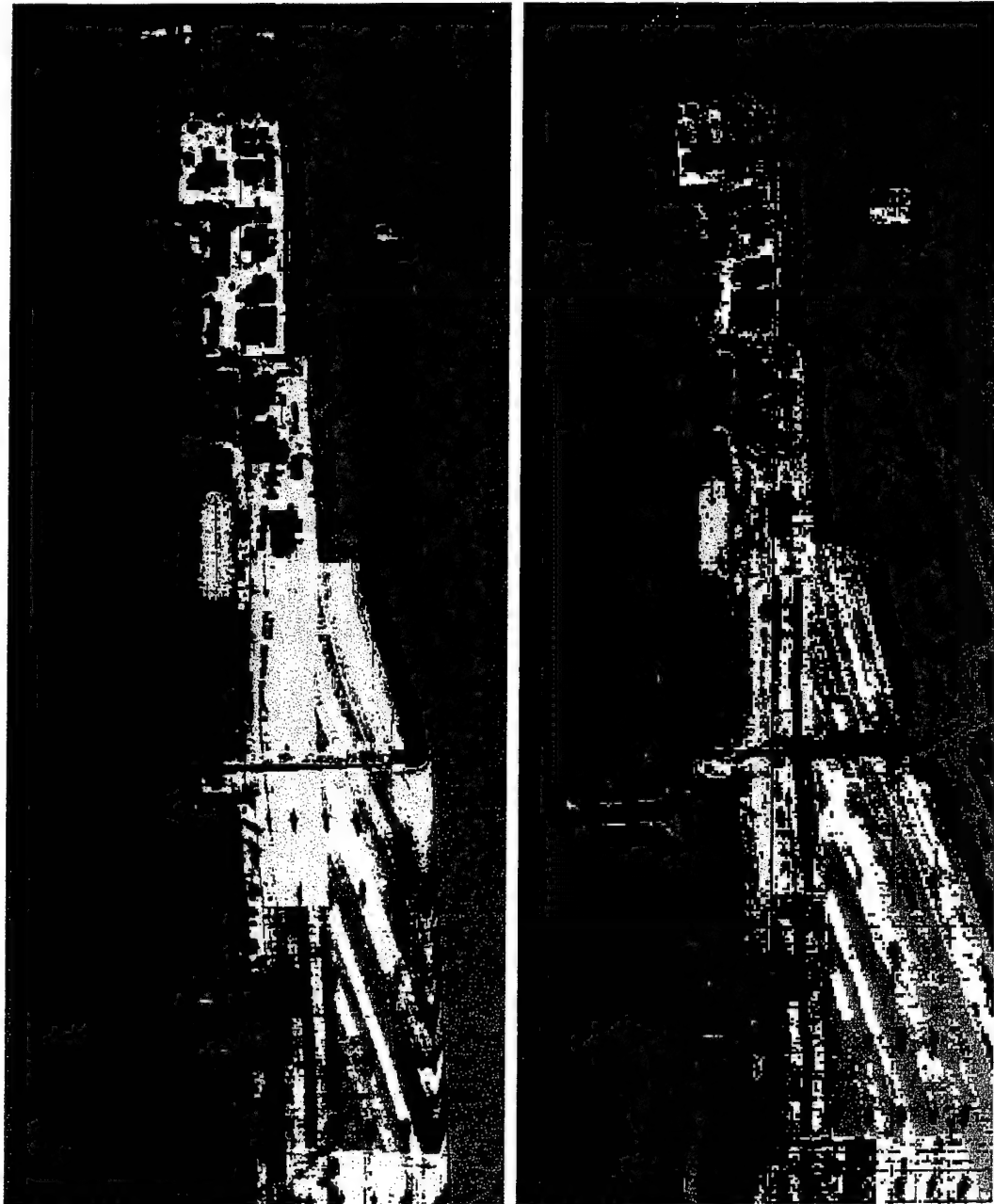
# Run 45

Run 31 (X2).

Figure 4: Parallelepiped results from 165 band cube.
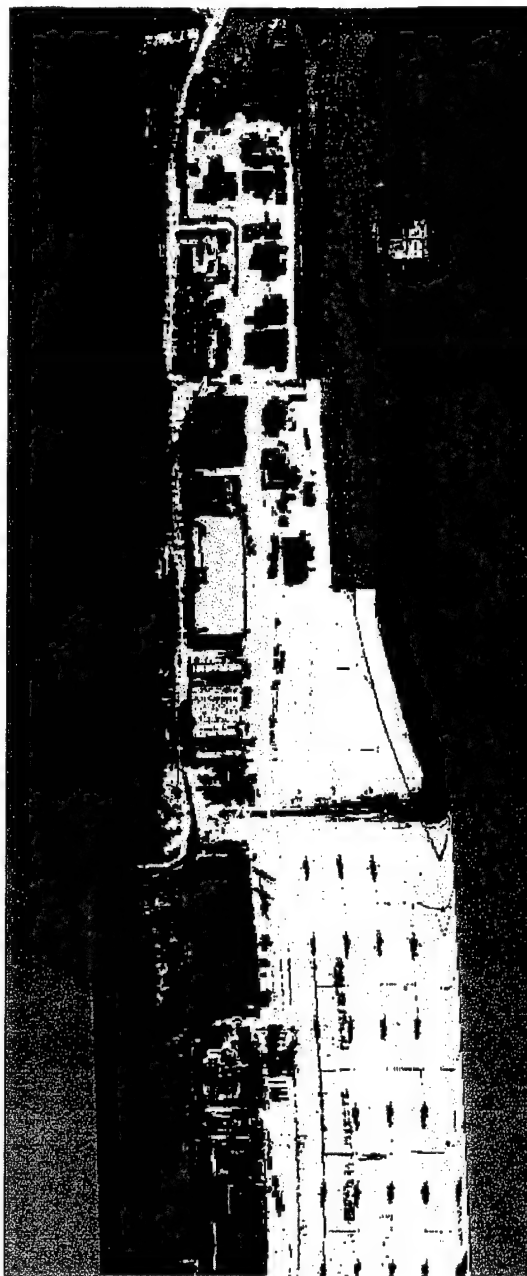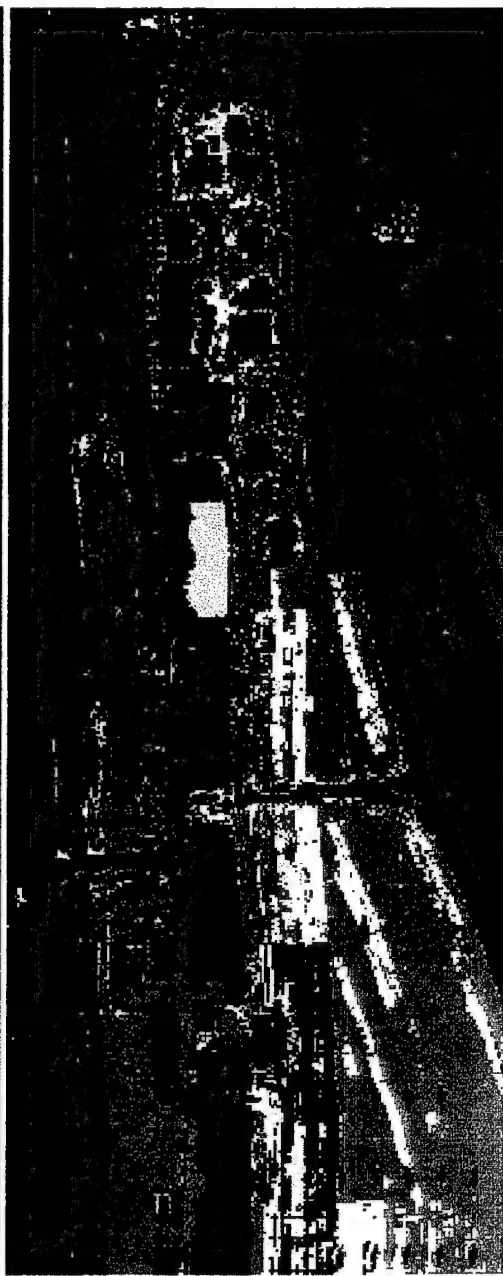
Run 45   Run 31 (X2).

Figure 5:   Parallelepiped results from PC bands 1-10 at 5 standard deviations from the mean.

**Run 45**　　　　**Run 31 (X2).**
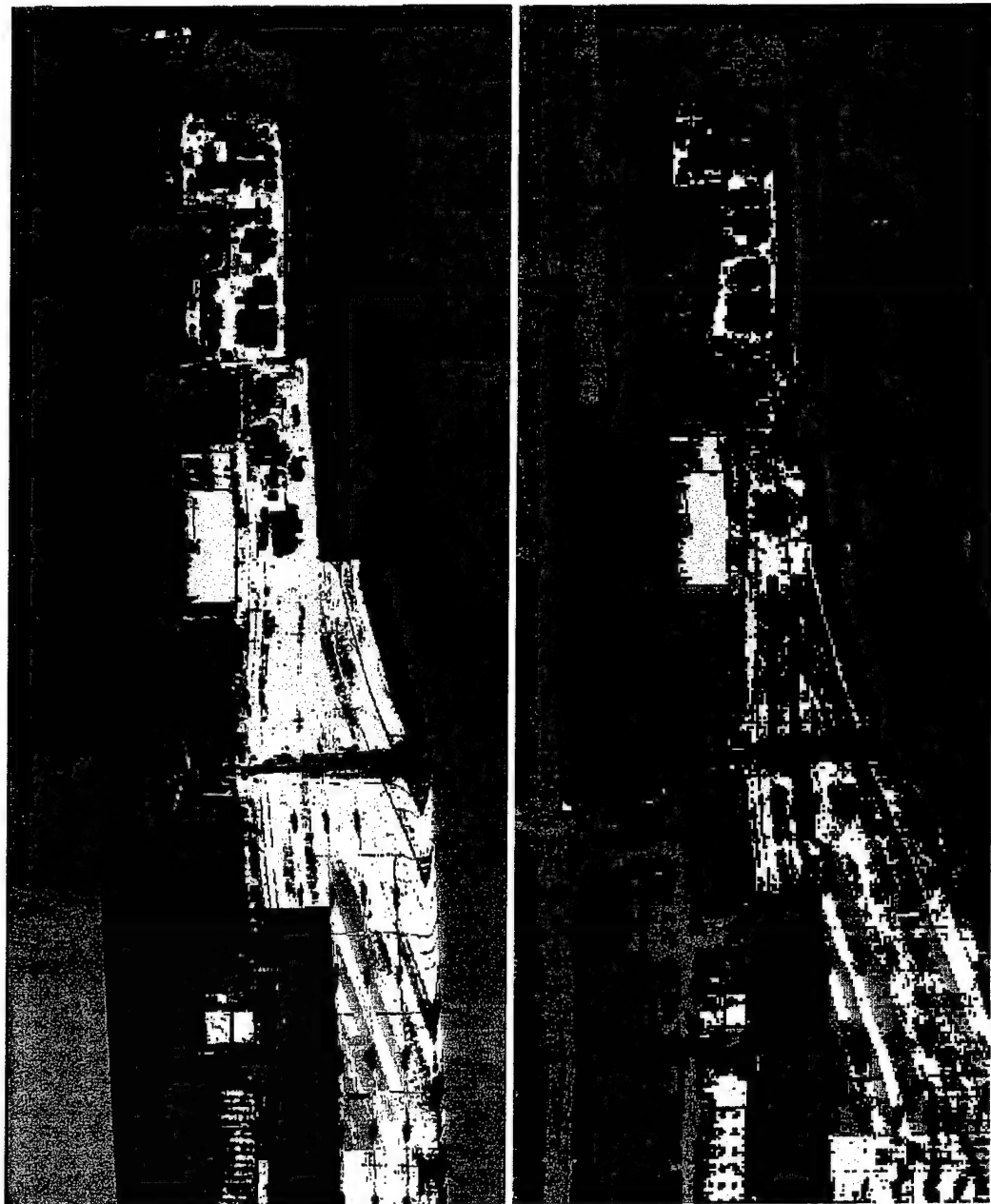
Figure 6: Spectral Angle Mapper results from PC bands 1-10.
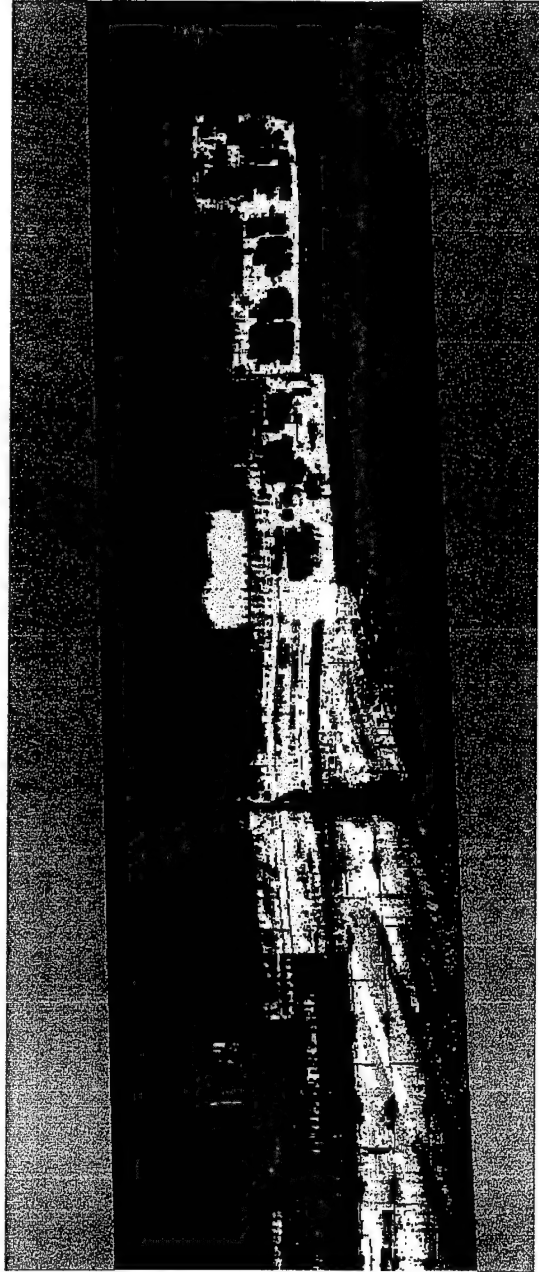
Run 45   Run 31 (X2).
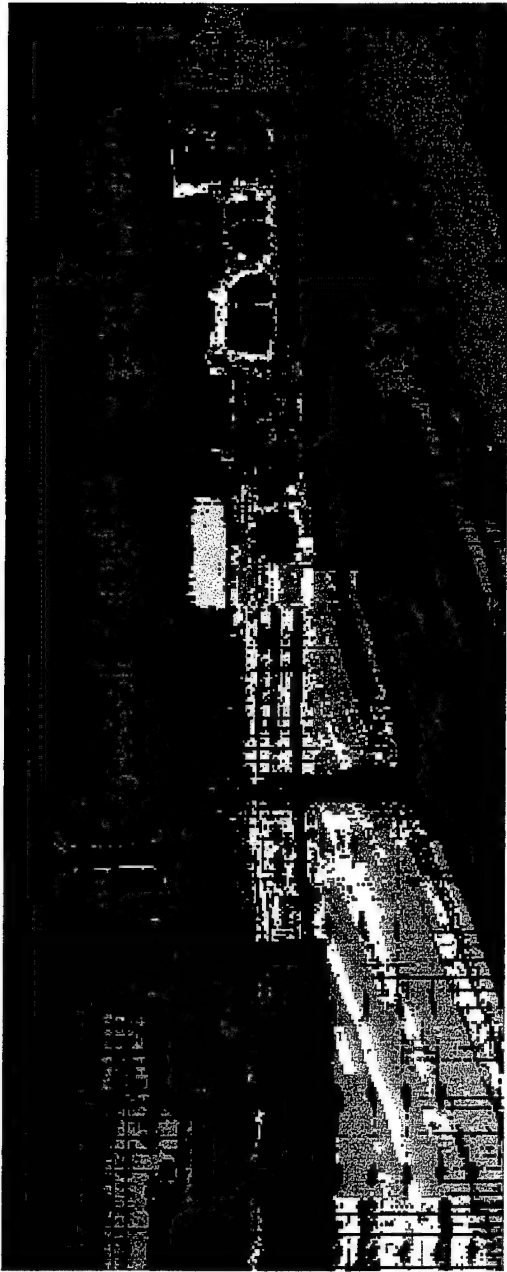
Figure 7: Parallelepiped results from PC bands 1-10, 3 standard deviations from the mean.

LIST OF REFERENCES

Aldrich, W. S., Basedow, R., Colwell, J. E., Kinder, W. D., *HYDICE System Performance – An Update*, Hughes Danbury Optical Systems, Inc., 1996.

Aldrich, W. S., Kappus, M., Mitchell, P., and Resmini, R. G., *The Flexible HYDICE Sensor's First Year of Operation*, Presented at the Eleventh Thematic Conference and Workshops on Applied Geologic Remote Sensing, Las Vegas, Nevada, 27 – 29 February 1996.

Aldrich, W. S., Kappus, M., Mitchell, P., and Resmini, R. G., *HYDICE Post-flight Data Processing*, 1996.

Anderson, M. E., Basedow, R. W., Carmer, D. C., *HYDICE System, Implementation and Performance*, Hughes Danbury Optical Systems, Inc.

Anderson, R., Malila, W., Maxwell, R., and Reed, L., *Military Utility of Multispectral and Hyperspectral Sensors*, IRIA State of the Art Reports, Infrared Information Analysis Center, November, 1994.

Avery, T. E. and Berlin, G. L., *Fundementals of Remote Sensing and Airphoto Interpretation*, 5th ed., Prentice-Hall, Inc., Upper Saddle River, New Jersey, 1992.

Basedow, R., Gulbransen, D., Murphy, D., Peterson, C., Rappoport, W., Rosebeck, J., Ruzicka, L., Silvergate, P., Wyles, R., and Zalewski, E., *HYDICE Focal Plane Design and Performance*, Hughes Danbury Optical Systems, Inc., March, 1994.

Basedow, R., Silvergate, P., Rappoport, W., Rockwell, R., Rosenberg, D., Shu, K., Whittlesey, R., and Zalewski, E., *The HYDICE Instrument Design*, Hughes Danbury Optical Systems, Inc., 1992.

Behrens, R. J., *Change Detection Analysis with Spectral Thermal Imagery*, Master's Thesis, Naval Postgraduate School, Monterey, CA, September, 1998.

Bergman, S. M., *The Utility of Hyperspectral Data to Detect and Discriminate Actual and Decoy Target Vehicles*, Master's Thesis, Naval Postgraduate School, Monterey, CA, December, 1996.

Collins, B. H., *Thermal Imagery and Spectral Analysis*, Master's Thesis, Naval Postgraduate School, Monterey, CA, September, 1996.

Dia, X., Khorram, S., *Quantification of the Impact of Misregistration on the Accuracy of Remotely Sensed Change Detection*, IEEE International Geoscience and Remote Sensing Symposium, vol. 4, pp. 1763-1765, August 1997.

ENVI, *User's Guide*, Version 3.0, Better Solutions Consulting Limited Liability Company, Lafayette, Colorado, December 1997 Edition.

Jahne, B., *Practical Handbook on Image Processing for Scientific Applications*, CRC Press LLC, Boca Raton, Florida, 1997.

Schowengerdt, R. A., *RemoteSensing: Methods for Image Processing*, 2nd ed., Academic Press, San Diego, CA, 1997.

Silvergate, P. R., *The HYDICE hyperspectral Imaging Experimental System and Future Technological Improvements*, Presented at the Eleventh Thematic Conference and Workshops on Applied Geologic Remote Sensing, Las Vegas, Nevada, 27 – 29 February 1996.

Stefanou, M. S., *A Signal Processing Perspective of Hyperspectral Imagery Analysis Techniques*, Master's Thesis, Naval Postgraduate School, Monterey, CA, June 1997.

INITIAL DISTRIBUTION LIST

1. Defense Technical Information Center 2
   8725 John J. Kingman Road., STE 0944
   Ft. Belvoir, Virginia 22060-6218

2. Dudley Knox Library 2
   Naval Postgraduate School
   411 Dyer Road
   Monterey, California 93943-5101

3. Richard C. Olsen, Code PH/OS 3
   Department of Physics
   Naval Postgraduate School
   Monterey, California 93943-5002

4. Chairman, Code PH 1
   Department of Physics
   Naval Postgraduate School
   Monterey, California 93943-5002

5. David Cleary, Code PH/CL 1
   Department of Physics
   Naval Postgraduate School
   Monterey, California 93943-5002

6. Chairman, Code SP 1
   Space Systems Academic Group
   Naval Postgraduate School
   Monterey, California 93943-5002

7. Dr. Greg Pavlin 1
   SITAC
   11781 Lee Jackson Memorial Highway
   Suite 500
   Fairfax, Virginia 22033-5309

8. Dr. Ron Resmini 1
   SITAC
   11781 Lee Jackson Memorial Highway
   Suite 500
   Fairfax, Virginia 22033-5309